Polarimetric SAR signals of river ice breakup

Sophie de Roda Husman

Technische Universiteit Delft

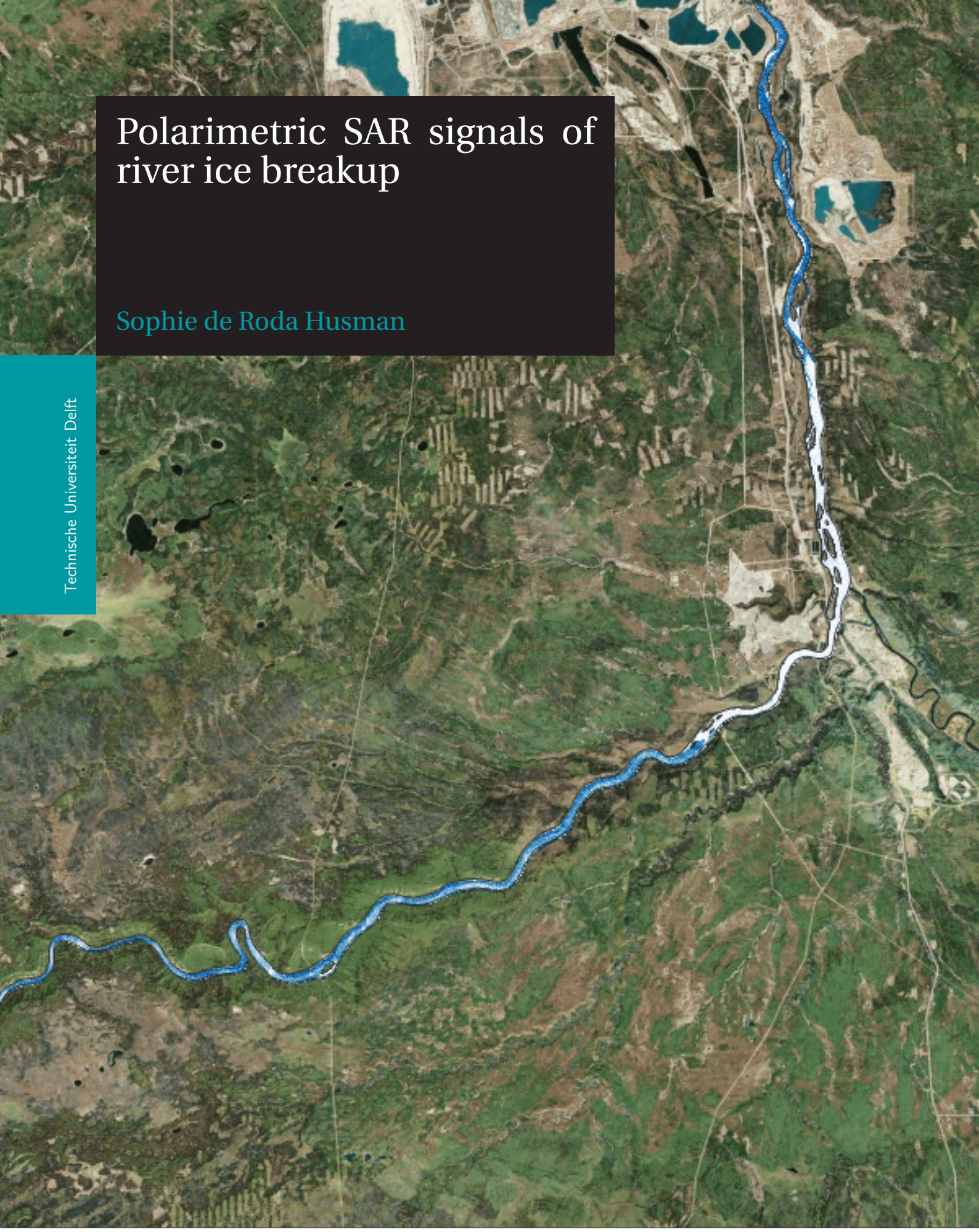

TU Delft Delft University of Technology

Challenge the future

On the cover

The cover shows an ice jam in a stretch of the Athabasca River flowing through the city of Fort McMurray. This ice jam, formed on 26 April 2020, resulted in disastrous flooding in Fort McMurray. The white pixels indicate the ice jam, water is indicated in blue. The river ice stages were derived from the backscatter in VV-polarization of the Copernicus Sentinel-1 image, acquired at 28 April 2020. The background image is courtesy of Bing.

Polarimetric SAR signals of river ice breakup

by

Sophie de Roda Husman

to obtain the degree of Master of Science

at the Delft University of Technology,

to be defended publicly on Tuesday November 3^{rd}, 2020 at 15:00 (GMT+1).

Student number:	4278437	
Project duration:	January, 2020 – November, 2020	
Thesis committee:	Dr. S.L.M. Lhermitte,	TU Delft, daily supervisor
	Dr. J.F. Lopez Dekker,	TU Delft, supervisor
	Dr. M.A. Eleveld,	Deltares & TU Delft, company daily supervisor
	Dr. J.J. van der Sanden,	Natural Resources Canada, external supervisor

TU Delft Delft University of Technology

Deltares Enabling Delta Life

ABSTRACT

Ice jams events can be devastating for the environment, human infrastructure, and local population. During breakup season, it is of great importance to be informed about the river ice cover condition in order to mitigate breakup flood risk. The Athabasca River near Fort McMurray, located in Alberta, is particularly prone to ice jam events and subsequent floodings. Satellite remote sensing techniques provide the necessary means to monitor the ice cover. Because of the wide availability most research and operational services for SAR river ice classification are based on single- or dual-polarized images. However, such imagery is limited in its ability to distinguish certain river ice types and open water states. The research presented examines how SAR polarimetry influences the detecting possibilities of specific ice types. Sentinel-1 (dual-polarization), RADARSAT-2 (quad-polarization) and RADARSAT Constellation Mission (compact-polarization) data were used to classify river ice during breakup. This study was about analysing a stretch of the Athabasca River which is prone to ice jam formation. First, SAR images from the 2018-2019 and 2019-2020 breakup were studied to find the temporal and spatial patterns of the radar backscatter. Next, sample areas with known ice stage (sheet ice, ice jam or open water) were selected. The sample areas of each ice stage were compared to assess the influence of SAR characteristics, as incidence angle and overpass time. In the last part of this study, a Random Forest classification was implemented in which intensity, texture and polarimetric features were used. Results show that classification accuracies increase with the inclusion of polarimetric decomposition features and GLCM mean texture features by enhancing between class separability and reducing the misclassification. Accuracies of 85.6% (Kappa = 0.78), 91.2% (Kappa = 0.87) and 91.0% (Kappa = 0.87) were obtained for Sentinel-1, RADARSAT-2 and RCM, respectively. The majority of the confusion between classes was due to similarities at backscatter signatures in very small incidence angles, mainly between open water and sheet ice under melting conditions. Also sheet ice early in the breakup season was confused with ice jams. To reduce the likelihood of misclassification, it is recommended to only use images with incidence angles higher than 30° and to include polarimetric and texture features in a classifier. Additional improvements can be achieved when using expert knowledge for tracking, since previous SAR images can provide added information when one understands the temporal patterns of river ice breakup. Further research should be directed at the development of an automatic classification approach that should be able to detect ice jams during the entire ice covered season. Having more knowledge about river ice breakup may help to eventually develop a river ice forecasting system, which may significantly reduce flood risk.

PREFACE

I want to say thanks to a lot of people.

I would like to take the opportunity to express some words of appreciation towards my supervisors. First of all, a big thanks to Stef, you always helped me when I lost track. Every time you gave me feedback, I was amazed at how you always managed to hit the nail on the head. Marieke, I am impressed by how much you know (about everything!). You are an example for me and I felt very honoured working together with you. Thanks for all the helpful advice, not only on the topic, but also on writing. Muchas gracias Paco, your sharp observations brought my thesis to the next level. Joost, I do not know how I can thank you enough. All the way from Canada, without having anything to do with the project, you said 'yes' when Dave asked you if you wanted to supervise me. It was incredibly helpful to work with a river ice plus SAR expert. I learned so much from you and I loved working with you. Thanks for everything you have taught me.

Next to my official supervisors, I was also blessed with many people at Deltares that made this project possible. It was amazing to have three 'mentors' at Deltares: Nena, Dave and Martijn. You were there since day one, picking me up for a tour along all the labs. It was so much fun working with you and the best part was our "ice meeting" (drinking ice cold beers over Skype). Dave, you did a great job organizing this project and are a truly amazing project manager. You have great communication and team-building skills and are always enthusiastic, which helped me a lot during the project. Nena, I owe you a very big thanks. You helped me with so many practical issues. It was great tackling some SNAP issues together. Thanks for checking on me, to see how I was doing when working from home. Martijn, you taught me so much about GPT's, bash scripts, Python in general. Thanks for all the great lessons. Thank you, Marieke, Dave, Nena and Martijn, for making me feel part of the team. Besides the 'river ice team', special thanks to the Operational Water Management team that hosted me at Deltares. Nadine Slootjes, thank you for involving me in your department, I had a great time and learned a lot. Also, I would like to express my gratitude to Enabling Technologies, one of the research lines within Deltares, that funded this project.

Also, I am very thankful to the staff from the River Forecasting Centre of Alberta Environment & Parks for all the help they gave. At the beginning of this project, Jennifer Nafziger and Stefan Emmer were so kind to share their knowledge and give me entire lectures on river ice breakup processes. During the thesis, they provided field updates as well as ice observation reports, maps, photos and videos of the observation flights. Thank you for bringing the data to life and making the research even more exciting!

Special thanks to Luis Veci and Brockmann Consult for providing an unofficial SNAP 8 pre-release to handle RCM data. NRCan, for providing the RADARSAT-2 data. And all other data providers that made this project possible.

Finally, there were so many that supported me. First of all, my lovely family. Thanks for the many times you told me how proud you were. My roommates in Rotterdam, thanks for all the laughs, hugs and great support. Pien and Geerten, unexpected, due to the outbreak of Covid-19, we partly lived together for a few months. Thanks for all the fancy dinners and yoga-sessions together. Many, many great friends, that were a welcome distraction (Soof, Neen, Iris, Merlijn, Maxim, Anna, Han, Merve, Goudvisjes, B122, and many more!). Last but not least, Mathijs. Thanks for all your help, in the good and the bad times. I love being with you.

A BIG thanks to everyone, I feel so blessed with so many amazing people around me. You rock my world!

Sophie de Roda Husman
Delft, Monday 26th October, 2020

NOMENCLATURE

LIST OF ACRONYMS

AEP	Alberta Environment & Parks
ATDD	Accumulated Thawing Degree Days
DN	Digital number
DTC	Decision Three Classifier
EO	Earth Observation
EW	Electromagnetic Wave
EODMS	Earth Observation Data Management System
ESA	European Space Agency
GeoTIFF	Geographical Earth Orbit Tagged Image File Format
GLCM	Grey Level Co-occurrence Matrix
GPT	Graph Processing Tool
GRD	Ground Range Detected
IW	Interferometric Wide Swath
LDA	Linear Discriminant Analysis
LR	Logistic Regression
NetCDF	Network Common Data Form
NB	Naive Bayes
NN	Nearest Neighbour
NRCan	Natural Resources Canada
OA	Overall Accuracy
QGIS	Quantum Geographic Information System
RADAR	Radio Detection and Ranging
RAR	Real Aperture Radar
RCM	RADARSAT Constellation Mission
RF	Random Forest
RFE	Recursive Feature Elimination
RFECV	Recursive Feature Elimination Cross-Validation
R2	RADARSAT-2
SAR	Synthetic Aperture Radar
SLAR	Side-Looking Airborne Radar
SLC	Single Look Complex
SNAP	Sentinel Application Platform
SVM	Support Vector Machines
SWE	Snow Water Equivalent
S1	Sentinel-1

LIST OF SYMBOLS

Variable	Description	Units
α	Decomposition parameter Alpha	$degree$
A	Decomposition parameter Anisotropy	–
β_0	Brightness coefficient	–
γ_0	Terrain-flattened coefficient	–
c	Speed of light	m/s
C	Covariance matrix	–
CH or S_{CH}	Circular transmit / horizontal receive backscatter	–
CV or S_{CV}	Circular transmit / vertical receive backscatter	–
δ_p	Penetration depth	m
$\Delta\hat{K}$	Test statistic	–
DC or ϵ_r	Relative dielectric constant	–
Φ	Polarimetric correlation coefficient	–
H	Decomposition parameter Entropy	–
HH or S_{HH}	Horizontal transmit / horizontal receive backscatter	–
HV or S_{HV}	Horizontal transmit / vertical receive backscatter	–
h_{rough}	Surface roughness	m
K_L	Lexicographic vector	–
K_P	Pauli vector	–
L	Length of antenna	m
λ	Wavelength	m
R	Slant range	m
ρ	Polarimetric phase difference	$degree$
ρ_{AZ}	Azimuth resolution	m
ρ_R	Ground range resolution	m
ρ_R	Range resolution	m
S	Size of footprint SAR image	m^2
σ_0	Scattering coefficient	–
T	Coherency matrix	–
θ_i	Incidence angle	$degree$
θ_l	Look angle	$degree$
τ_p	Pulse length	m
VH or S_{VH}	Vertical transmit / horizontal receive backscatter	–
VV or S_{VV}	Vertical transmit / vertical receive backscatter	–

List of Figures

LIST OF TABLES

CONTENTS

1

INTRODUCTION

1.1. RIVER ICE MONITORING

Many regions around the world experience weather below freezing points, leading to ice formation on lakes and rivers. More than half of the fresh surface waters in the Northern Hemisphere annually freezes over (e.g. Yang et al., 2020). For many regions in the Northern Hemisphere, river ice heavily impacts everyday life, both beneficially and detrimentally. On the one hand, winter ice roads and ice bridges are the primary means of transportation in many places. On the other hand, the development of an ice cover can lead to flooding triggered by ice jams, damage to property and infrastructure, interference with navigation, and reduction of power at hydroelectric generating plants (Hicks, 2016).

River ice governs the winter regime of many rivers located in cold regions. Typically, during colder periods rivers freeze up in upstream direction in a complex and dynamic manner (Puestow et al., 2004). During spring, the warmer weather brings increased flow discharges due to snowmelt and/or rainfall, which rises the water levels (Jasek, 2003). This often leads to breakup of the ice cover, reducing attachment to the river banks and causing the ice cover to move and break into relatively small ice blocks (Beltaos and Prowse, 2001). The small blocks move down the river and encounter stationary ice cover and they pile up behind it, initiating an ice jam. Ice jams can stay in place for many days, causing extremely high water levels (Beltaos and Prowse, 2001). On an annual basis, for countries like Canada, costs of damages related to ice breakup can exceed many millions of dollars (Morse and Hicks, 2005), mostly due to flooding caused by ice jams (Ettema et al., 1999).

Consequently, an understanding of river ice processes is absolutely necessary. Examples of relevant river ice properties include the extent of the ice, ice phenology, ice types, ice thickness, ice condition, and surface flow velocities (Duguay et al., 2015). The understanding of these river ice processes is of importance to various science, engineering and management activities. These can include forecasting on breakup and ice-jam flooding, hydraulic and hydrological modelling and the decision process regarding water intake and discharge (van der Sanden, 2015). The monitoring of river ice is conducted using a variety of approaches depending on the objectives and available resources. Conventional monitoring methods include ground-based surveys and aerial monitoring techniques (Vincent et al., 2004). Often however, collecting information on river ice is restricted by harsh weather conditions and the large extent and poor accessibility of the rivers of interest (van der Sanden, 2015).

Satellite remote sensing techniques provide the necessary means to increase the spatial and temporal frequency of conventional ice monitoring techniques. For the monitoring of river ice during breakup, Synthetic Aperture Radar (SAR) satellites offer multiple advantages over optical satellites. Radar sensors rely on their own sources of radiation to “illuminate” objects, which enables SAR satellites to create images regardless of weather and daylight conditions. Moreover, radar is sensitive to the presence of free water and is able to penetrate dry ice cover and snow (Flores-Anderson et al., 2019).

SAR images can be particularly useful in discriminating ice cover types. Especially during breakup season, it is of great importance to be informed about the river ice cover condition in order to mitigate breakup flood

risk. In the last two decades many important advances have been made in the field of river ice classification using radar data. Multiple case studies have shown that SAR images are very useful at identifying and classifying various ice types on medium (more than 100 m width) and large rivers (Tracy and Daly, 2003). Several classification methods were developed, for rivers such as the Canadian Athabasca River (Unterschultz et al., 2009) and Peace River (Gauthier et al., 2006, Weber et al., 2003).

Most research and operational services for river ice classification are based on the backscatter intensity of single- or dual-polarized SAR images. Nevertheless, such imagery is limited in its ability to discriminate certain river ice types and open water states (Mermoz et al., 2009). The additional information contained in polarimetric SAR imagery, also known as quad-polarization modes, may be used to improve classification potential (e.g. Lindenschmidt and Li, 2018, Mermoz et al., 2009), but current image swath widths (up to 50 km for RADARSAT-2 quad-polarization) are too small for large scale operational applications (Dabboor and Geldsetzer, 2014). The recently launched RADARSAT Constellation Mission (RCM) offers new opportunities. The Canadian RCM has the capacity to acquire Compact Polarimetry (CP) data, that offers a greater amount of information than standard dual-polarization modes, while covering much greater swath widths compared to quad-polarization modes (Dabboor and Geldsetzer, 2014). RCM transmits a right-circular polarization and receives orthogonal linear polarizations (Charbonneau et al., 2010). Simulated CP data have shown promising results in preliminary studies on ice classification and may have the classification potential of quad-polarization satellites (e.g. lake ice classification (van der Sanden and Geldsetzer, 2015) and sea ice classification (Dabboor and Geldsetzer, 2014)).

Besides the additional value of polarimetric variables, also texture information can be of added value in river ice classification. Traditional methods to classify river ice based on backscatter intensity, do not take the spatial distribution of the ice cover types into account. Pixel intensity alone can be insufficient for an accurate classification, since backscatter signatures for melting sheet ice and water can be similar (Sobiech and Dierking, 2013). Gauthier et al. (2006) showed that a combination of texture analysis and backscatter information of single-polarization RADARSAT-1 data, improved classification accuracies during freeze-up. Also in the field of lake ice classification, texture features have shown to be effective (e.g. Hoekstra et al., 2020).

Even though polarimetric and texture features could provide more information about river ice breakup than radar backscatter alone, limited research has been conducted on the added value of texture and polarimetric features for river ice classification. In order to improve classification, an in-depth understanding of the interaction of differently polarized radar signals with river ice is essential. Therefore, the main purpose of this study is to examine the possibility of using intensity, polarimetric and texture features to improve river ice classification, developed from a deeper understanding of radar - ice interaction. For this study classification methods for Sentinel-1 (dual-pol), RADARSAT-2 (quad-pol) and RCM (compact-pol) were developed.

1.2. CURRENT METHODS AND LIMITATIONS

Compared to other cryospheric research fields (i.e., glaciers, snow-cover, sea ice and permafrost), the study of river ice is relatively young (Jeffries et al., 2012). Figure 1.1 shows that few papers were published in the years 2000 to 2019 about river ice. The figure illustrates that the research on river ice falls behind on other cryospheric research fields.

Recent advances have been made on studying river ice using optical remote sensing. However, most studies faced issues due to persistent cloud layers over the rivers during breakup season. While no studies were found on identifying different types of ice, some studies use optical remote sensing to detect the presence of river ice. Like Chaouch et al. (2014), that used MODIS images to develop an automated technique to detect and map ice on the Susquehanna River, USA. The study distinguished between three classes: water, ice and clouds. Other studies aimed to estimate the river ice breakup date (Cooley and Pavelsky, 2016, Pavelsky and Smith, 2004). The latter study described an automated algorithm for breakup detection for the four largest rivers draining into the Arctic Ocean and estimated breakup dates with an accuracy of approximately ± 1.3 days (Cooley and Pavelsky, 2016). However, besides the significant disadvantage of the often cloud-obscured rivers, the relatively coarse spatial resolution made it difficult to distinguish small-scale breakup processes. Breakup detection using this approach was only practical for examination of rivers wider than 500 m (Cooley and Pavelsky, 2016). Kääb et al. (2019) used optical images of the PlanetScope constellation, which consists of more than a hundred small cubesats to index river flow velocities. However, also this study faced issues regarding cloud cover that impeded the interpretation of the optical images Kääb et al. (2019). Hence, as stated

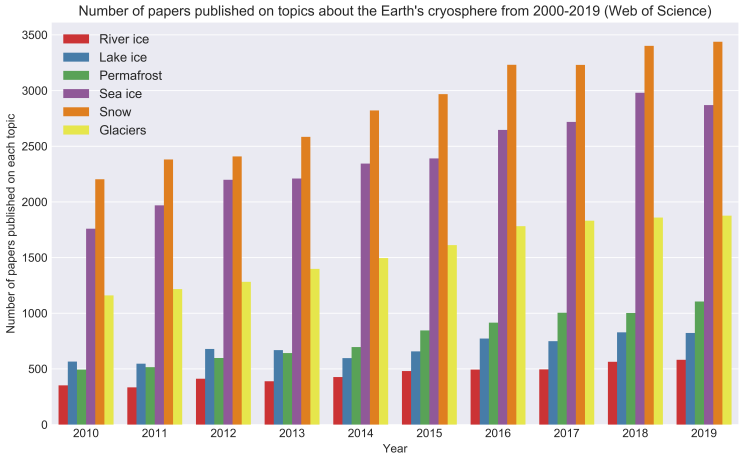

Figure 1.1: Number of papers published on topics about the Earth's cryosphere from 2000 to 2019. The data were obtained using the Web of Science. The lack of information on river ice makes it difficult to understand its behaviour during the breakup season.

before, optical remote sensing data provide limited usefulness during the breakup season in many regions, due to persistent cloud covers that create unusable images. To overcome this problem, active microwave data were used for this study.

Over the last decades, different approaches were used to classify the river ice cover during freeze-up, winter and breakup season. Both supervised (e.g. Łoś et al., 2019, Mermoz et al., 2009, 2013) and unsupervised (e.g. Chu et al., 2015, Chu and Lindenschmidt, 2016, Gauthier et al., 2010) classification methods have been applied. Supervised classification can be much more accurate than unsupervised classification, but depends heavily on the training sites. Most studies on the classification of river ice used unsupervised methods, based on backscattering values or texture parameters, nearly all using *k*-means algorithm (e.g. Lindenschmidt and Li, 2018, Mermoz et al., 2009).

The studies that used SAR data to study river ice are mostly based on single- or dual-pol images. At the start of this century, most research focused on RADARSAT-1 single-pol images to differentiate ice types (e.g. Gauthier et al., 2006, Unterschultz et al., 2009, Weber et al., 2003). Only one study was found that used dual-pol Sentinel-1 images (Łoś and Pawłowski, 2017), most other dual-pol studies used RADARSAT-2 (e.g. Chu et al., 2015, Jasek et al., 2013, Lindenschmidt et al., 2011). Mermoz et al. (2009) and Lindenschmidt and Li (2018) showed that quad-pol data is better able to classify river ice than single-pol data. A recent study showed good classification results for both dual-pol and quad-pol RADARSAT-2 images (Łoś et al., 2019).

The recent launch of the RADARSAT Constellation Mission gave a new push to the polarimetric SAR research, as the satellites of the RCM acquires compact polarimetry data. As stated by Charbonneau et al. (2010), the same classification results are expected as obtained with quad-pol RADARSAT-2, while wider swaths are imaged. Several studies simulated RCM compact-pol data from RADARSAT-2 quad-pol images, giving promising results for river ice (Charbonneau et al., 2010, van der Sanden et al., 2014) and lake ice (van der Sanden and Geldsetzer, 2015) mapping.

Few studies were found that examine how polarimetry influences the ice detecting possibilities of SAR. Moreover, no studies were found that compared the classification performance of dual-, quad-, compact-pol channels on river ice breakup. The launch of the RCM gives a new type of polarimetry data to detect river ice. The purpose of this study is to investigate the value of different polarimetric features for river ice classification. To reach this goal, SAR data of Sentinel-1 (dual-pol), RADARSAT-2 (quad-pol) and RADARSAT Constellation Mission (compact- pol) are analysed and compared.

1.3. RESEARCH QUESTIONS

The analysis of data in different polarization channels may reveal additional information about the characteristics of the ice cover. Interpretation of SAR images requires understanding of how the different polarization channels interact with the river ice. The aim of this study is to compare the potential of dual-, quad- and

compact- polarization to recognize different ice stages during breakup. The focus is on the breakup season, where a melting ice and/or snow layer will influence the scatter characteristics. Three classes are distinguished in this study: sheet ice, open water and ice jams. The latter class represents all rubble ice stages, also including ice runs.

To strive for a better understanding of the polarized radar signals with different ice cover conditions, the following research question was formulated:

> **What are the potentials and limitations of Sentinel-1, RADARSAT-2 and RADARSAT Constellation Mission on river ice type classification during breakup season?**

To solve this research question, three sub-questions are presented that need to be answered in order to make the main question more transparent.

1. *What is the effect of the characteristics of the different SAR acquisitions on river ice classification?*

   Each SAR acquisition has its own characteristics, which complicates comparison between Sentinel-1, RADARSAT-2 and RCM. First of all, the images are acquired with different satellites that carry non-identical sensors, leading to images with different resolutions, incidence angles and flight directions. Moreover, the images are acquired during different circumstances, such as the time of the day and weather conditions. The influence of these differences should be understood, in order to develop an accurate classification algorithm.

2. *Which features are most suited to base the river ice classification on during breakup season? Why do some features perform better than others?*

   Many different features from the SAR data can be extracted that can provide information about the target. The most straight forward features are the backscatter intensities, but also polarimetric features (e.g. phase difference between polarization channels and eigenvalue decomposition) and texture features (e.g. grey level co-occurrence matrix) may provide additional information. In this study one of the most used machine learning algorithms is used, a Random Forest model. Only the most important features should be used in this model, since it makes the model easier to interpret and reduces overfitting. Hence, it should be studied which features are best in distinguishing between the classes of interest.

3. *How does river ice classification improve when polarimetric and texture features are included in a Random Forest model compared to a basic backscatter intensity classification approach?*

   From literature it is known that river ice classifiers based on single-pol backscatter values have its shortcomings. When the previous sub-question has been answered, it can be studied if and how much the classification accuracies can be improved for each satellite mission by including polarimetric and texture features to a river ice breakup classifier. Due to the different mission characteristics, the added value of polarimetric and texture values can be different for Sentinel-1, RADARSAT-2 and RCM.

1.4. THESIS OUTLINE

Chapter 2 provides background information that is relevant for the understanding of the processes regarding river ice classification. The main topics in this chapter are the river ice processes, active microwave remote sensing and theory of polarimetry. Chapter 3 essentially consists of two parts; first, the study area is introduced and finally, a description of the data is provided. Details on the reference data is presented in Appendix A. In Chapter 4 the methodology which is used in this thesis is covered. This step-by-step approach starts with data preprocessing, feature extraction, SAR characteristic comparison, supervised classification and an error analysis. More details on the preprocessing steps are presented in Appendix B. The most important results regarding the polarimetric features and image classification are presented in Chapter 5. Results less relevant for the main line of research, but important for the evaluation of the quality of the main results can be found in Appendix C, D and E. Subsequently, the main topics of discussion that concern implications on the presented results and points for improvement will be discussed in Chapter 6. In conclusion, Chapter 7 will present brief answers to all of the research questions.

2

BACKGROUND

This chapter is split up into five different parts that are important for understanding the processes of river ice classification. As a result, this chapter is not so much a continuous storyline, but more like a patchwork of information.

The chapter starts with a theoretical background on the river ice processes that occur annually over most northern hemisphere rivers. The second part introduces the remote sensing technique that was used in this research to measure the river ice: active microwave remote sensing. Subsequently, the next section relates the previous chapters about river ice and SAR data and discusses the interaction between the ice and the microwave waves. The fourth section elaborates on the theory of polarization of electromagnetic waves. The last section discusses existing methods to classify SAR data using supervised algorithms.

2.1. RIVER ICE PROCESSES

In nearly every river located in the Northern Hemisphere, ice is present during winter months for a period that ranges from days to several months (Beltaos and Prowse, 2001). The river ice season can roughly be divided into three events: freeze-up, mid-winter and breakup. During freeze-up an ice cover is formed on the rivers. Then follows the mid-winter period, when the ice is in place and gets thicker. At the end of the ice season, breakup season arrives, where the deterioration and/or melting of ice takes place and eventually the clearing of an ice cover (Hicks, 2016).

The process by which an ice cover on a river can form, evolve, and deteriorate is substantially different from that on lakes. Unlike for lakes, flow velocities and fluid turbulence cannot be neglected for rivers (Hicks, 2009). Except for shallow parts of a river, the flow velocities and turbulence cause most flows to be relatively well-mixed throughout their depth. Consequently, flow hydraulics play an important role in the formation of a river ice cover. Combined with the meteorological conditions, they determine how a river ice cover will form and evolve (Hicks, 2016).

Figure 2.1 presents a summary of different river ice processes. The process starts off with open water during fall/winter, ending with open water again during spring. Between these open water stages, stages of freeze-up, mid-winter and breakup periods can be distinguished. These stages differ from year to year and from river to river. The processes are explained in more detail in the coming three paragraphs.

Phase 1: Freeze-up

The first phase of the freeze-up of a river is the cooling of water to freezing point (Hicks, 2016). Within vertically well-mixed rivers, the entire water column may *supercool*, which means the water cools to below 0°C without transforming to ice. This occurs when little to no surface ice is present on the river, the atmospheric temperature is below 0°C, and the water flow is turbulent enough to overcome the stratification. Water remains liquid and supercooled, until the latent heat is released, i.e. when the liquid water changes to solid ice (Brown et al., 2011).

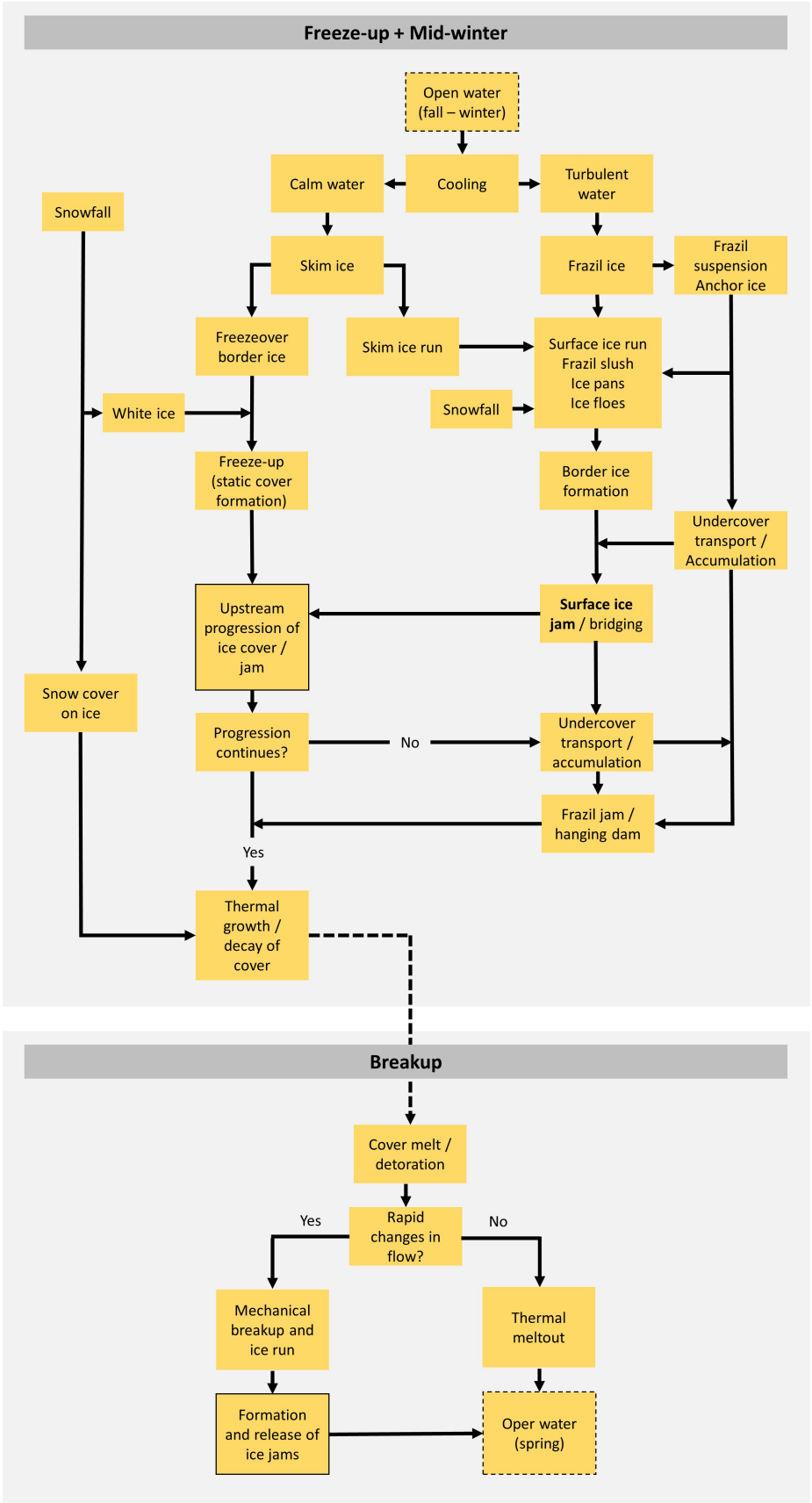

Figure 2.1: Overview of river ice processes during freeze-up, mid-winter and breakup. Both during freeze-up and breakup ice jams may form in a river. Adapted from Shen (2010).

In the slower moving parts of a river, along the river banks and edges of islands, turbulence is negligible, enabling *skim ice* to form. When the coverage of skim ice increases, it grows out from the banks and forms *border ice* (Hicks, 2016). The skim ice prevents further supercooling of the water beneath, resulting in thickening and lateral growth (Hicks, 2009).

In the faster moving parts of the river, ice crystals are formed, referred to as *frazil ice* (Brown et al., 2011). In supercooled water, the frazil ice crystals are called 'active', because they have the ability to stick. They tend to group into clusters and stick to underwater objects, such as bed sediments, plants and man-made structures (Ashton, 1986). The clusters of frazil ice accumulate further to *frazil slush* (also known as *frazil flocks*). When the frazil slush has increased in size, it will start floating on the water surface and form *frazil pans*. As the pans are carried downstream and tend to collide, the growing process continues with the formation of *frazil rafts*. Some of the pans may also stick to the border ice, increasing its lateral extent (Brown et al., 2011, Hicks, 2009).

Occasionally, frazil ice forms *anchor ice*, which happens when frazil ice attaches to the river bottom. As additional frazil ice accumulates to the anchor ice, the anchor ice grows and thickens (Brown et al., 2011). In small streams with fast currents, this can result in the formation of *ice dams* (Gerard, 1989). Anchor dams can temporally block the water discharge, which increases the water level (Brown et al., 2011).

As the freeze-up process continues, more and more frazil pans and rafts form and the border ice increases (Hicks, 2013). As the surface concentration of ice flows increase to the order of 80 to 90%, *bridging* becomes likely. The ice flows congest, leading to a cessation of their movement downstream (Hicks, 2009). Bridging typically occurs at locations where the river narrows, such as between bridge pillars, natural constrictions or constrictions due to border ice (Hicks, 2009).

Now the first part of a stationary ice cover has developed, it is just a matter of time for the ice cover to expand. Incoming ice flows accumulate upstream of the bridged ice cover, a process known as *frontal progression* (Hicks, 2009). An illustration of the ice cover development is given in Figure 2.2. An excellent metaphor was given by Hicks (2013), that compared the progression of river ice with a 'traffic jam', where the same process can be found as cars are backing up the blockage (Hicks, 2013). The accumulated ice cover is known as a *juxtaposed ice cover*. Besides the expansion of the ice cover, when flow velocities are sufficient, also a process of *hydraulic thickening* can occur, as the incoming ice flows are swept under the ice front and be deposit under it.

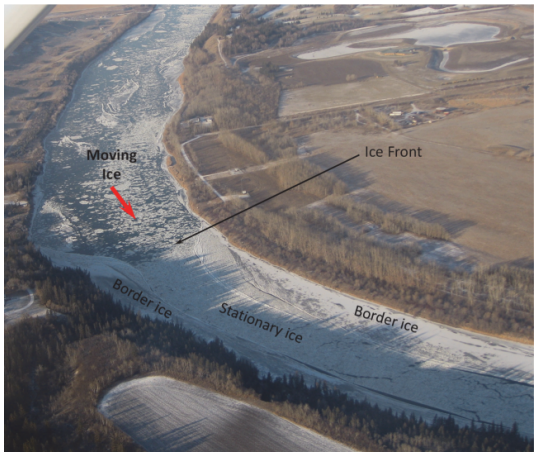

Figure 2.2: Natural constrictions and border ice, cause bridging of the ice cover. The incoming ice flows lead to the upstream progression of the ice front (frontal progression) and thickening of the stationary ice cover (hydraulic thickening). *Photo courtesy of T. Ghobrial and M. Loewen.* (Hicks, 2016)

The increased thickness of the ice cover results in an increased water level and corresponding decreased flow velocity. Once the flow velocity upstream is sufficiently low, ice flows are not swept under the ice front anymore and the frontal progression continues. As the stationary ice cover grows, the forces acting on the ice accumulation increase. The river ice breakup is controlled by the balance between the driving force (upstream discharge) and the resisting force (downstream ice cover) (Beltaos and Prowse, 2009). When the acting forces are sufficient to overcome the internal strength, the ice cover collapses, which then causes thickening of the

cover, termed a *hummocky ice cover*. This collapse, resulting in a thicker and rougher ice cover, increases the water level (Hicks, 2016).

Once the ice cover has stabilized, the interstitial water freezes, which adds strength to the ice cover. In extreme cases, the obstruction of the ice cover leads to overbank flooding, referred to as *freeze-up ice jams* (Hicks, 2009).

Phase 2: Midwinter
After initial ice formation and the establishment of an ice cover, the ice thickening process continues, which can occur from above or below. If there is no insulating snow cover, there is thermal heat loss from the ice cover, so the growth happens at the bottom. When a snow cover is present, ice may also form on top of the ice cover. This occurs due to water that seeps through cracks in the ice cover and saturates the lower part of the snow cover. Once this lowest layer freezes on top of the original ice surface, it is referred to as *snow ice* (Hicks, 2016).

Phase 3: Breakup
When spring arrives, the breakup process will start. The nature of the breakup may vary from a *thermal* to a *mechanical* breakup. During an ideal thermal breakup, an ice cover deteriorates through warming and melts in place, (almost) without movement of ice (Brown et al., 2011). At the other end is the mechanical breakup, which is more complex and less understood. In a mechanical breakup, the breakup of ice occurs suddenly, typically involving ice runs and ice jams (Hicks, 2016). Normally, breakups take place during warming periods when the strength of the ice cover decreases and the discharge increases due to snowmelt or precipitation. Therefore, most breakups fall between the extremes of thermal and mechanical breakup (Brown et al., 2011). The manner of breakup depends on the trade-off between ice deterioration due to increased temperatures (hydrodynamic influences) and ice cover fracture due to increased discharge (meteorological influences) (Hicks, 2009). In general, the closer a breakup is to a mechanical breakup, the more damage it will create due to the increased discharge and ice parts (Beltaos and Prowse, 2009).

The first stage in a thermal breakup is the melt of snow on top of the ice cover due to increased temperatures. Because of the decreased albedo, more and more solar energy will be absorbed, which increases the thermal breakup process (Hicks, 2016). Then open leads will develop at the thinner locations of the ice cover, lowering the albedo even more. The water absorbs the heat energy and will melt the ice cover from the underside, enlarging the open leads. Ultimately, all the ice disappears and the river is open again (Hicks, 2016).

The first stages of a mechanic breakup are the same as for a thermal breakup, the snow on the ice cover melt and open leads develop. However, in the case of a mechanical breakup, the water level typically rise fast, resulting in stresses on the ice cover. Usually, the ice cover is not able to resist the forces and the ice sheet will crack. Normally these cracks can be found along the banks, making the main ice sheet free to float up with the rising water levels. Also transverse cracks form, due to the increased flow stress on the underside of the ice cover. At that time the ice cover is broken in ice sheets that are still relatively large, and are generally not able to move due to geometric constraints of the river, like tight bends or islands in the channel (Hicks, 2016). Due to the flow drag, the ice sheet will break into smaller pieces and drift downstream with the flow. Ultimately this running might stop due to a new geometric constraint of the river or an intact ice sheet, which may initiate an *ice jam*. This jam obstructs the water flow and causes the water level to rise upstream. Due to the sudden blockage, a backwater wave propagates upstream, possibly leading to additional fractures in upstream ice sheets (Hicks, 2009).

The water levels upstream of the ice jam increase and the ice jam may lengthen due to incoming ice, increasing the forces on the ice cover. In general, these increased stresses result in a collapse of the accumulation, which thickens the ice cover. When the internal strength is no longer able to withstand the forces caused by the ice and water, the ice jam may release (Hicks, 2016). The moving ice is generally referred to as *ice runs*, the waves that appear due to the release of the ice jam are referred to as *javes* (Beltaos and Prowse, 2009). Downstream, when the ice runs and javes encounter new impediments, new ice jams may be formed. Eventually, extreme long ice jams may be formed, increasing the flood risk (Hicks, 2009).

Ice stage interpretation
The stage of the river ice influences the signal that is visible in a SAR image. In Figure 2.3 a basic explanation is presented that tells how different ice stages can be recognized in a SAR image. A more in-depth explanation is given in the next sections of this chapter.

When the river is free of ice, before the freeze-up has started or after breakup season, the reflected signal in all polarizations is low. The incoming EM waves are reflected away from the sensor, as the water will behave like a 'mirror'. When there is a dry ice sheet, during the winter and the beginning of the breakup season, there will be a relatively high signal visible in all polarizations. A part of the radar signals will be reflected back to the SAR sensor by the surface. Another fraction will penetrate the ice layer, reflect at discontinuities inside the layer and redirected back to the sensor. A part of this reflection occurs at the water-ice interface. For a melting ice sheet, during a thermal meltout, the reflection back to the sensor will be low. The same phenomenon as with open water can be found, hence the layer will behave like a mirror. During an ice jam, very interesting things happen with the radar signals. Due to the rough surface and the dynamic structure, the backscatter will be very high in the co-polarization channels (HH and VV). Another part of the EM waves will depolarize, giving a large backscatter in the cross-polarization channels (HV and VH) as well. More information about the difference between the polarization channels and depolarization can be found in Section 2.4.

	Co-pol *HH* or *VV*	Cross-pol *HV* or *VH*
Open water	Low backscatter	Low backscatter
Dry ice sheet	Medium / high backscatter	Medium / high backscatter
Melting ice sheet	Low / medium backscatter	Low backscatter
Rough ice jam	High backscatter	High backscatter

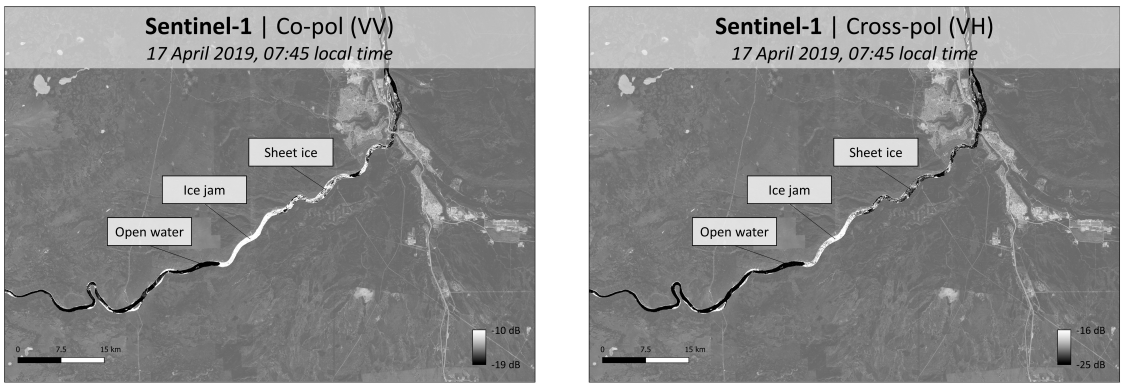

Figure 2.3: Qualitative comparison of radar backscatter during different stages of ice on a river, occurring during winter and spring. Open water can be found before freeze-up and after breakup season. In winter and during the beginning of spring, a large part of a frozen river consists of a dry ice layer. During a thermal breakup, a melting ice sheet is present. During a dynamic breakup, ice jams are formed and released. In the Sentinel-1 co-pol (VV) and cross-pol (VH) images the ice jam is clearly visible.

2.2. ACTIVE MICROWAVE SENSORS

River ice has a broad social and economic impact, can be used as an indicator for climate variability and climate change and, on top of that, influences the aquatic ecosystem (Duguay et al., 2015). However, a dramatic reduction in ground-based observations has taken place since the 1980s (e.g. Prowse et al., 2011). Satellite remote sensing provides the necessary means to increase the monitoring possibilities, due to its high spatial and temporal resolution.

Microwave sensing covers the range from approximately 1 cm to 1 m wavelength. Due to its long wavelengths compared to visible and near-infrared techniques, microwaves have special properties that can be very useful in monitoring river ice. Because of the longer wavelengths, microwaves are able to penetrate clouds and measure in all weather conditions (Ulaby et al., 1986).

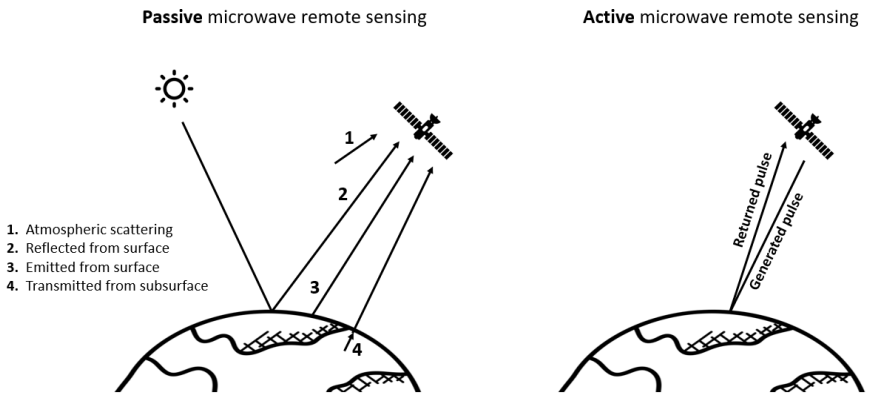

Figure 2.4: Active and passive microwave remote sensing. Passive remote sensing systems record EM radiation from the sun, atmosphere or surface or the Earth. Active remote sensing techniques are not dependent on the sun's EM radiation or thermal properties of the Earth, but create their own EM energy.

Microwave sensing includes active and passive forms of remote sensing, see Figure 2.4. In passive microwave remote sensing, a sensor detects the naturally emitted energy with a microwave wavelength of a target. Applications of passive microwave remote sensing include hydrology (soil moisture measurements), oceanography (mapping sea ice, currents, surface winds and the detection of pollutants, such as oil slicks) and meteorology (measurements of water and ozone contents) (Canada Centre for Remote Sensing, 2019). A major disadvantage of passive imaging sensors is that they do not emit their own radiation, but receive natural light and thermal radiation from the Sun and the Earth's surface. Reflected energy will only be measured by a passive imaging sensor when the sun is illuminating the Earth, i.e. during the day (Canada Centre for Remote Sensing, 2019). In contrast, in active microwave remote sensing, sensors provide their own source of microwave radiation to illuminate an object, which enables them to image a target, day and night and through cloud covers (Ulaby et al., 1986).

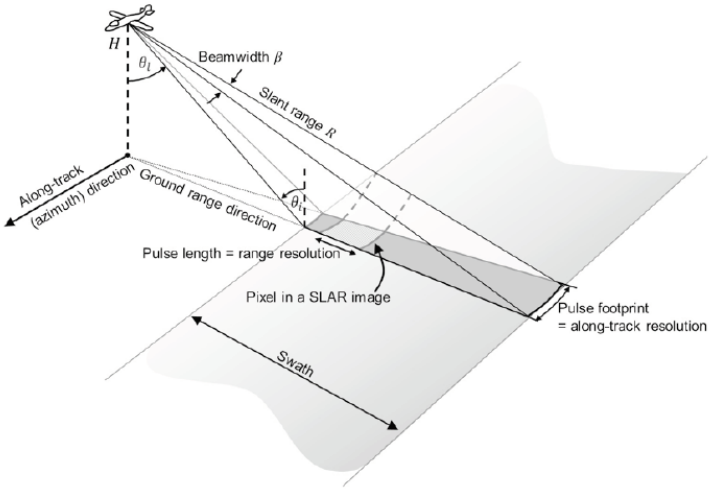

Figure 2.5: Observation geometry of a SLAR system. The radar is located at altitude H and observes the Earth with a looking angle θ_l. The size of the footprint S is defined by the beamwidth β and the distance between the satellite and the slant range R. The generation of a scene is facilitated by the forward motion of the SLAR system. Acquired from Flores-Anderson et al. (2019).

Active microwave remote sensing is generally divided into two classes: imaging and non-imaging. Non-imaging microwave sensors, like altimeters and scatterometers, measure in one linear dimension, e.g. distances. This research focuses on *imaging active microwave sensors*, that make a two-dimensional representation of an area by measuring the intensity of the backscattered energy (Canada Centre for Remote Sensing, 2019).

The most common form of imaging active microwave sensors is *RADAR*, which is an acronym for (imaging) **RA**dio **D**etection **A**nd **R**anging (Canada Centre for Remote Sensing, 2019). Although radar systems now use microwave wavelength energy almost exclusively instead of radio waves, the acronym was never changed (James, 1989). The first radio microwaves were generated and detected in an experiment conducted by Hertz in 1886. Hertz demonstrated that the waves were subject to reflection (Buderi, 1996). Shortly after the turn of the century military consideration really boosted the development of radar during the World War II: the imaging radars were used for detecting and positioning of aircraft and ships (Hanssen, 2001).

In the 1950s Side-looking (Airborne) Radar (SLAR) was developed (Canada Centre for Remote Sensing, 2019). Unlike most optical imaging systems, the antenna of a SLAR system 'looks' at targets with the *looking angle* θ_l (Skolnik et al., 1980). Sometimes the incidence angle θ_i is annotated, which equals 90°- θ_l. The antenna illuminates an area on the Earth's surface, the so-called *footprint*, see Figure 2.5. The size of this footprint S, in both range (across-track dimension perpendicular to the flight direction) and azimuth direction (along-track dimension parallel to the flight direction), is defined by

$$S \approx \frac{\lambda}{L} R \tag{2.1}$$

where λ is the wavelength of the sensor, L the length of the antenna and R the distance of the sensor from the ground (Raney, 1998).

The *spatial resolution* of a SAR system defines the minimum separation between two targets, which are indistinguishable in a SAR image. The higher the spatial resolution of the sensor, the more detail a SAR image contains. Spatial resolution is frequently confused with pixel size, event though the concepts are not interchangeable. Pixel size is the spacing of the pixels after processing the data (Flores-Anderson et al., 2019). SAR spatial resolution is determined in the two principal SAR image directions: ground range and azimuth. The *ground range resolution* (ρ_G) is derived from slant range (across-track) resolution (ρ_R). Targets can be distinguished if their slant range separation is greater than half the transmitted pulse length. Hence, the slant range resolution is defined by

$$\rho_R = \frac{c \cdot \tau_P}{2} \tag{2.2}$$

where c corresponds to the speed of light and τ_P the transmitted pulse length (Skolnik et al., 1980). The ground range resolution can be computed by projecting the slant range resolution onto the ground surface, which requires correction for the local slope and elevation of the terrain. Hence, the ground range resolution can be written as

$$\rho_G = \frac{\rho_R}{\sin\theta_i} \tag{2.3}$$

where ρ_R is the slant range resolution and θ_i the incidence angle. The *azimuth resolution* (ρ_{AZ}) is defined by the width of the beam in azimuth direction, which is determined by the antenna length. Following Equation 2.1, the azimuth resolution is defined by

$$\rho_{AZ} = S_{AZ} \approx \frac{\lambda}{L_{AZ}} R \tag{2.4}$$

with S_{AZ} indicating the antenna footprint in azimuth direction, λ the wavelength of the sensor, L_{AZ} the side length of the antenna in azimuth direction and R corresponding to the distance to the ground (Skolnik et al., 1980).

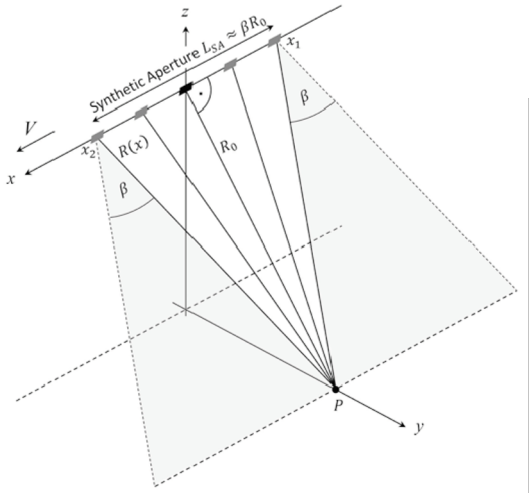

Figure 2.6: Observation geometry of a SAR system. The SAR principle synthesizes a much longer effective antenna from a sequence of observations made with a shorter antenna as the system moves in forward direction. The length L_{SA} of a synthetic aperture can be estimated by multiplying the beamwidth β with the nominal slant range R_0. Acquired from Flores-Anderson et al. (2019).

To achieve acceptable azimuth resolutions, lengths of antennas are required that are not feasible with current-day technology. In 1952 a more practical solution for the azimuth resolution problem was developed, the *Synthetic Aperture Radar* (SAR) (Hanssen, 2001). SAR is able to acquire a finer azimuth resolution by making use of the forward motion of a platform and special method of recording and processing the backscattered signal (Canada Centre for Remote Sensing, 2019), see Figure 2.6. A SAR image has a much higher resolution than SLAR images and is the basis for all modern radar systems (Moreira et al., 2013).

2.3. INTERACTION OF RADAR SIGNALS WITH RIVER ICE

Now that the seasonal cycle of river ice and the basic principles of a polarimetric SAR system are known, the interaction of radar signals with the ice target is discussed in this section. SAR systems transmit EM signals and measure the backscattered portion of this signal in the direction of the sensor. The radar backscattering coefficient σ_0 provides information about the imaged target and is a function of both surface and sensor characteristics (Unterschultz et al., 2009). Although the radar backscattering coefficient contains very interesting information about the river ice, the signal is difficult to interpret. Under predominantly freezing conditions, the microwave signal is able to penetrate through the surface and thus contains information about the surface and the internal structure of the river ice (Hall and Martinec, 1985).

Many different components influence a received radar signal, including river and sensor characteristics. These parameters are discussed in Section 2.3.2. To understand how these variables influence the backscatter, first the basic principle of a backscattered radar signal is discussed in Section 2.3.1.

2.3.1. SCATTERING MECHANISMS

The backscatttered signal that is measured by the SAR sensor consists of a combination of echos from the target. There are two main types of scattering mechanisms: *surface scattering* and *volume scattering*. The contribution of surface and volume scattering to the backscattered signal is influenced by the characteristics of the (partly) frozen ice. In order to understand this interplay, it is convenient to split the river into four components: water, ice, snow and air (Chu et al., 2015), see Figure 2.7.

Surface scattering reflects the incoming EM wave at the interface of target components with different dielectric properties. During winter, the main part of the surface scattering occurs at the water-ice interface. The EM wave can penetrate through the dry ice layer and reflects at the water-ice layer. The signal scatters at this interface, because there is a larger difference in dielectric constant between the ice (DC $\approx$ 3) and water layer (DC $\approx$ 80). However, this changes when the breakup season arrives. Due to the warmer temperatures, the snow and ice start melting which limits the penetration of the radar signal. Resulting in a surface-air interface that starts to dominate the backscatter (Unterschultz et al., 2009).

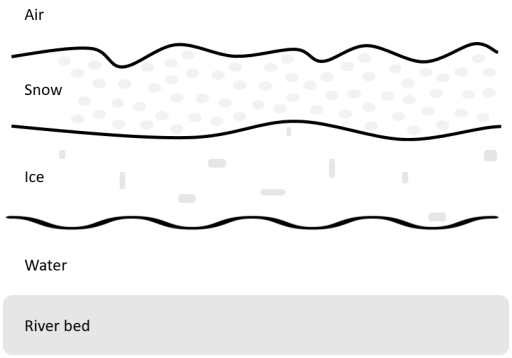

Figure 2.7: Geometry of the scattering problem. During the ice season, the river can be simplified as a combination of layers: water, ice, snow and air. These four components play an important role in the amount and type of backscatter that a SAR sensor receives.

Volume scattering occurs in inhomogeneous layers. In the case of river ice, this will be mainly in the snow and ice layer, in which there are dielectric discontinuities like cracks, air inclusions and impurities. When the signal penetrates a layer, it can be reflected at these dielectric discontinuities and be redirected back to the sensor (Unterschultz et al., 2009). Besides the dependence of volume scattering on the heterogeneous nature of the ice layer, it also depends on sensor properties, such as wavelength and incidence angle (Weber et al., 2003). If the size of the dielectric discontinuities in the river ice is small relative to the wavelength, the volume backscattering component is low. More about this is Section 2.3.2.

To conclude, highly heterogeneous ice covers can be expected to have a higher backscattered signal from both surface and volume scattering (Chu et al., 2015). The effect of the radar side-looking geometry, the sensor and river ice characteristics on the type and amount of backscatter, are discussed in the following sections.

2.3.2. INFLUENCING PARAMETERS

The interaction of microwave signals with a target is a function of the observed target and the characteristics of the sensor. Also, the relative orientation of the sensor to the observed target influences the backscatter received by the SAR system. Three of the most important influencing parameters on the received backscatter are explained in the next paragraphs.

EFFECT OF RIVER ICE CHARACTERISTICS

The first source that influences the backscattered radar signal are the characteristics of the river ice itself. The two most important parameters that influence the backscatter are the surface roughness and the dielectric properties.

Surface roughness

The surface roughness, abbreviated as h_{rough}, specifies how rough a surface is. As was presented in Figure 2.7, an ice cover knows multiple layers, and thus multiple surfaces that can vary in amount of roughness. Whether a surface appears rough is a relative concept. Relative roughness depends upon the wavelength and incidence angle of the SAR sensor (Unterschultz et al., 2009).

There are two famous criteria on when a surface is defined as rough, namely the *Rayleigh Criterion* and *Fraunhofer Criterion*. In literature, the Rayleigh Criterion is used as a first-order classification of when a surface can be defined as rough or smooth. However, for natural surfaces the stricter Fraunhofer criterion for smoothness is more appropriate (Woodhouse, 2017). Both criteria indicate a surface as rough when the height deviation from the mean height of the surface exceeds the value of h_{rough}, which is determined by Equations 2.5 and 2.6 (Ulaby et al., 1986):

$$h_{\text{rough}} > \lambda/(8\cdot\cos\theta_i) \qquad \text{Rayleigh Criterion} \tag{2.5}$$

$$h_{\text{rough}} > \lambda/(32\cdot\cos\theta_i) \qquad \text{Fraunhofer Criterion} \tag{2.6}$$

where h_{rough} is the standard deviation of the surface height, λ the signal wavelength and θ_i the incidence angle. Note that according to Equations 2.5 and 2.6 a layer might be indicated as rough in X-band, but not in

L-band. The concept of effective roughness is explained by Figure 2.8, which shows that a rougher surface can lead to different scattering behaviour. This figure is in accordance with the Fraunhofer Criterion (Equation 2.6).

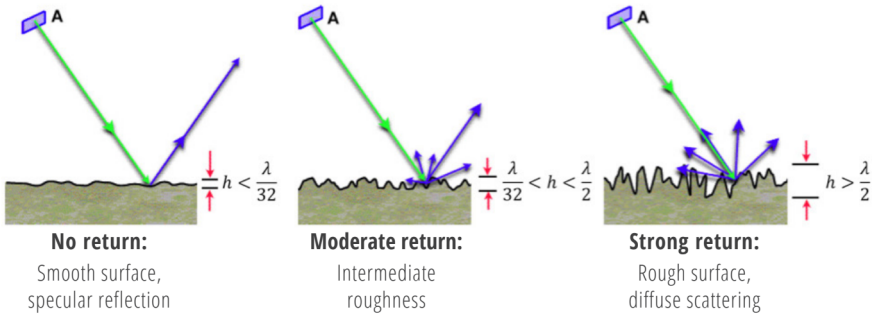

Figure 2.8: Sketch of the dependence of surface roughness on the sensor wavelength (in accordance with the Fraunhofer Criterion). The amount of backscatter increases as the wavelength-dependent surface roughness increases, hence the same pixel may look darker on a L-band (λ = 24 cm) than on a X-band (λ = 3.1 cm) SAR image. Acquired from Flores-Anderson et al. (2019).

For a smooth surface, most of the energy is directed away from the surface in a single direction, hence no significant portion of the energy will be backscattered to the sensor. This 'mirror-like' reflection is referred to as *specular reflection*. Such coherent surface scatters arise in for example calm water or a smooth ice surface and will show dark in a radar image. For most natural surfaces we find *diffuse* or *non-coherent* scattering. A rough surface will create a diffuse scattering resulting in a stronger backscatter, hence a brighter pixel in a SAR image (Skolnik et al., 1980).

Dielectric constant

The second parameter that influences the reflection of the radar signal, is the relative dielectric constant (DC) ϵ_r, which describes how deep the signal penetrates the surface. The relative DC of river ice and snow is almost completely dependent on their free-water content (Unterschultz et al., 2009). When the ice cover is dry, microwave signals with frequencies between 1 to 10 GHz can potentially penetrate to depths ranging from 100 m to 10 m respectively (Hallikainen and Winebrenner, 1992). However, when the breakup season arrives and the ice starts to melt, the penetration depth decreases.

The penetration depth (δ_p) represents the largest depth within a medium that can contribute to the backscatter. This depth is defined as the depth at which the power of a propagating wave is equal to e^{-1} of the power at the surface of that medium. If scattering losses are ignored, the penetration depth in the direction of the incidence angle can be calculated by

$$\delta_p = \frac{\lambda}{4\pi} \frac{1}{\sqrt{[1 + (\frac{\epsilon''}{\epsilon'})^{\frac{1}{2}} * \frac{\epsilon'}{2}}} \tag{2.7}$$

where λ is the wavelength of the sensor in free space, ϵ' and ϵ'' the real and imaginary part of the dielectric permittivity (Ulaby et al., 1986). In reality, the penetration depth of a wave will be smaller than the calculated δ_p in Equation 2.7, due to scattering losses (Hallikainen and Ulaby, 1986).

Ice in its liquid state (i.e. water) has an extremely high DC (around 80). Consequently, the reflection of microwaves at the ice surface increases and nearly no penetration is allowed. When the water crystallises into clear ice, the molecules bound and are no longer able to interact with the radar signal. This results in an extreme drop of the DC (around 3.2) (Cumming, 1952), making the layer almost transparent to the incoming microwaves. Surfaces with a high DC (i.e. water) have an increased radar reflectivity. For large incidence angels, most of the scattering will reflect away from the sensor, resulting in a low measured backscatter. The dielectric properties of different water stages are presented in Table 2.1.

Table 2.1: The most important dielectric constants for river ice analysis. Adapted from Weber et al. (2003).

	Dielectric constant	Source
Air	1	Evans (1965)
Freshwater ice - clear ice with air bubbles > 0.6 cm	2.99	Cooper et al. (1976)
Freshwater ice - milky ice	3.08	Cooper et al. (1976)
Freshwater ice - clear ice	3.17	Evans (1965)
Dry snow	1.2-2.0	Hallikainen and Ulaby (1986)
Wet snow	>35	Hall and Martinec (1985)
Fresh water	81	Raney (1998)

EFFECT OF SENSOR CHARACTERISTICS

There are several SAR sensor characteristics that influence the radar return signal, namely wavelength (or frequency), incidence angle and polarization of the emitted EM waves (Unterschultz et al., 2009). The following discussion focuses on the effect of each of these sensor characteristics.

Wavelength

The *wavelength* is of primary importance in the interaction of EM waves with river ice. The wavelength affects the penetration capacity and the spatial distribution of the scattered power. In a comparable situation, a microwave sensor with a longer wave penetrates river ice to a greater depth than a sensor with a shorter wavelength. The distribution of the scattered power is related to the scattering mechanisms (surface, volume, double-bounce scattering). The effective scale of the river ice roughness is relative to the incident wavelength, hence the wavelength determines the scattering patterns of a backscattered signal from a target (van der Sanden, 1997).

In this study, there is no difference in wavelength between the acquisitions, because only one frequency was used (5.3 GHz). All selected SAR sensors measure at C-band, which is equivalent to a wavelength of 5.6 cm.

Incidence angle

The *incidence angle* influences the roughness sensitivity of a sensor, and therefore the amount of the backscattered signal. The incidence angle describes the angle between the sensor and the normal to the intercepting surface. When slopes are tilted toward the sensor, a stronger backscatter is expected than for slopes tilted away from the sensor (Farr, 1993). The effect of the incidence angle on the radar backscatter is less pronounced for rougher surfaces, because the returned signal is dominated by diffuse scattering rather than specular reflection. Likewise, for targets where volume scattering is dominant, the effect of the incidence angle reduces (Unterschultz et al., 2009).

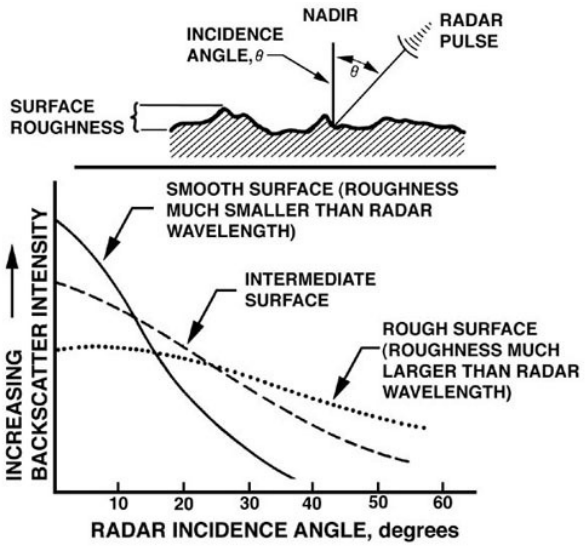

Figure 2.9: The relationship between the incidence angle and the radar backscattered intensity. The backscatter generally decreases for larger incidence angle. The influence of the incidence angle increases with decreasing surface roughness. Acquired from Imhoff (1995).

Figure 2.9 shows the effect of the incidence angle on the radar backscatter for smooth, intermediate and rough surfaces. Smooth surfaces (see Eq. 2.5 and 2.6) act like a mirror, when the incidence angle is small. However, with an incidence angle larger than 20°, the amount of backscatter decreases, because the specular reflection is directed away from the antenna. The opposite phenomenon occurs for rough surfaces. For steep incidence angles, most of the emitted signal is scattered in random directions, resulting in a lower total backscatter than from a smooth surface at the same incidence angle. For larger incidence angles, rough surfaces still produce a lot of random scattering, which results in a higher backscatter than for smooth surface at the same incidence angle (Imhoff, 1995).

The effect of different incidence angles on the backscattered signal was studied in this research. There was a large variety of incidence angles in the used data products, ranging from ±20° to ±50°.

Polarization

The *polarization* of SARs affects the interaction with river ice, because it defines the plane in which the microwave and river ice interact (van der Sanden, 1997). SAR is an active sensor that uses its own source of illumination, which enables SARs to control the polarization of a transmitted or received signal. The scattering mechanisms do not contribute to all polarimetric channels equally (Mermoz et al., 2009).

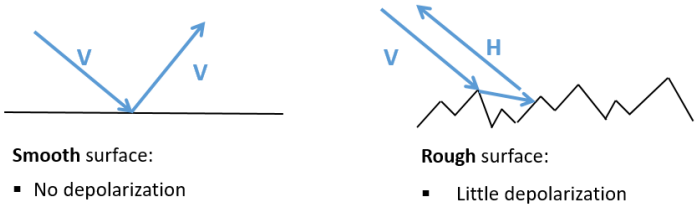

Figure 2.10: Depolarization caused by surface scattering. In case of a smooth surface (a), generally speaking the outgoing signal will be scattered back with the same polarization as the incoming signal. In this figure the incoming signal is vertically polarized, resulting in an outgoing signal that is also vertically polarized. The amount of backscatter received by the sensor is dependent on the angle of the surface relative to the incoming signal. For a rougher surface (b), there can be some depolarization. When the incoming signal is vertically polarized, the signal can be depolarized, resulting in a horizontally polarized backscatter.

In general, when the backscattered signal is mostly created by surface scattering, the amount of depolarization is low. This means that if the outgoing signal is vertically polarized, the direction of the backscattered signal will remain unchanged and be vertical as well. The same holds for incoming horizontally polarized waves, which will also create outgoing horizontal waves. This results in a high S_{VV} and S_{HH}, and relatively low S_{HV} and S_{VH} when the backscatter is mainly generated by surface scattering. However, when the surface of a target is very rough relative to the incoming wavelength, theory tells that there might be little depolarization (Freeman and Durden, 1998), see Figure 2.10.

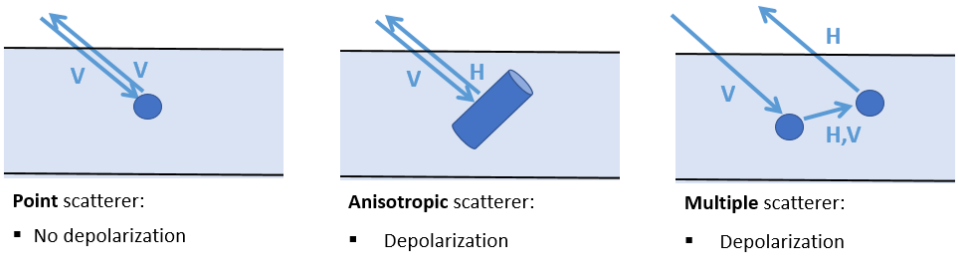

Figure 2.11: Depolarization caused by volume scattering. When a radar signal penetrates a target, the signal can hit an isotropic point scatterer (a). In general, this backscattered signal will have the same polarization as the incoming signal. For anisotropic scatterers (b) this is not the case. The anisotropic nature causes the incoming signal to change of polarization, so if the incoming signal is vertically polarized, the outgoing signal will be horizontally polarized. When a signal hits multiple scatterers (c), the signal can depolarize as well.

The main source of depolarization of an incoming SAR signal is volume scattering. A horizontally polarized wave might hit several impurities, bounce back and forth among them, and be backscattered to the satellite

in a vertically polarized state. However, in general the overall radar backscatter received from a depolarized signal is much lower than from a non-depolarized signal (Freeman and Durden, 1998). Whether a signal depolarizes, is dependent on the nature of the scatterer, see Figure 2.11. When an incoming radar signal hits a single isotropic point scatterer and is scattered back to the sensor immediately, usually the signal will not depolarize. When the scatterer is non-isotropic, and thus has a different value when measured in different directions, the signal may depolarize. The same holds for a signal that hits multiple scatterers. These scatterers can be located in one or multiple layers (Groenenboom and Snieder, 1995). See Figure 2.11.

EFFECT OF RADAR SIDE-LOOKING GEOMETRY

The *viewing geometry* describes the relative orientation of the SAR sensor to the observed object. Depending on the orientation of objects relative to the sensor, effects as foreshortening, layover and shadowing may be induced. These characteristics result from the side-looking configuration of the SAR system (van der Sanden, 1997).

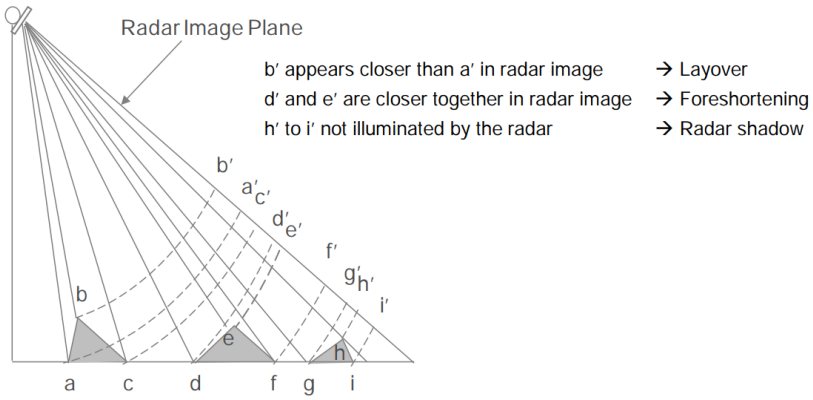

Figure 2.12: Visual representation of viewing geometry distortions: foreshortening, layover and radar shadow. Radar images are projections of a scene onto an image plane, leading to characteristic distortions. Acquired from van Zyl (2011).

Foreshortening occurs along slopes that face the sensor and results in high radar returns. *Layover* also results in a high backscatter, but occurs when the radar return signal from the peak of the target is received earlier than the returned signal at the base of the target. *Radar shadowing* appears when a slope faces away from the sensor, with an angle that is steeper than the sensor depression angle (angle between the radar beam and the horizontal at the radar platform) (Unterschultz et al., 2009). A visual representation of foreshortening, layover and radar shadowing is presented if Figure 2.12.

2.4. POLARIZATION OF ELECTROMAGNETIC WAVES

Different polarization modes are affected differently in their interaction with river ice. The polarization state of an EM wave can change when the wave scatters from a target, also referred to as depolarization. Depolarization is a measure of the change in the degree of polarization of a polarized incident wave as a consequence of scattering (Emery and Camps, 2017). Consequently, the measurement of depolarization leads to a better understanding of the local scattering mechanisms of the scene.

2.4.1. LINEAR AND CIRCULAR POLARIZATION

For man-made sources, such as SARs, the transmitted and received radar waves have a well-defined polarization (van Zyl, 2011). There are three categories of polarized waves: linear, circular and elliptical (Nave, 2011). *Linear polarization* is an EM wave that is an in-plane wave, this concept is explained in Figure 2.13. In this research, the data products of Sentinel-1 and RADARSAT-2 were used, which transmit and receive linear polarized waves.

Besides linear polarization, recently also *circular polarization* modes are becoming more popular for SAR systems. For circular polarization, both H and V waves are transmitted with a 90 degrees phase difference. The concept is explained in Figure 2.14. In this study circular polarized waves from the RADARSAT Constellation Mission are used.

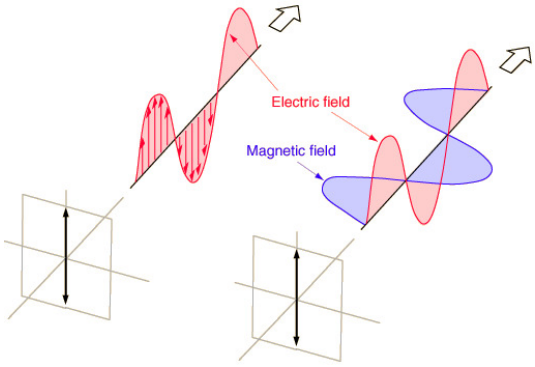

Figure 2.13: A plane EM wave is said to be linearly polarized. The electric field wave (red) is accompanied by a magnetic field wave (blue) as illustrated. In this figure, a vertical transmitted wave is presented. However, also horizontal EM waves can be transmitted. Acquired from Nave (2011).

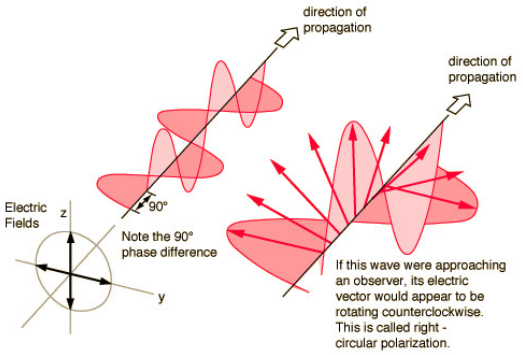

Figure 2.14: Circular polarization consists of two orthogonal EM plane waves, an H-wave and a V-wave. The waves are equal in amplitude, but differ in phase by 90 degrees. Circular polarizations could be right- or left-circularly polarized. When looking at the incoming wave, the electric vector of the EM wave coming towards you rotates counterclockwise. However, we refer to this wave as *right-circular* wave, as the direction of propagation is clockwise. Acquired from Nave (2011).

In this study a *compact mode* of circular polarimetry was used. In compact polarimetric configurations, only one transmit/receive cycle is required instead of two that are required for a quad-pol system. Hence, this reduces the pulse repetition frequency and data rates by a factor of two for a given swath width (Boularbah et al., 2012). The circular compact mode transmits circular waves and receives linear H and V waves. This configuration is known as Circular-Transmit-Linear-Receive, abbreviated as CTLR (Raney, 2007).

The last category of polarization is known as *elliptical polarization*. This concept is very similar to circular polarization, but for elliptical polarization the phase difference is not equal to 90 degrees (Nave, 2011). This type of polarization is not used for transmitted radar signals in SAR systems, so will not be further discussed.

A SAR system can be designed to operate as a linear single polarization system (from now on referred to as *single-pol*), where there is a single polarization transmitted and received. A linear dual polarized system (referred to as *dual-pol*) transmits horizontally or vertically polarized waves, and receives both polarizations. Quadrature polarized radars (referred to as *quad-pol* or *full-pol*) use the four polarization modes, the system alternates between transmitting and receiving both horizontally and vertically polarized waves. CTLR compact-pols transmit a circularly polarized signal, which can be right-circular or left-circular, and receive circular signals or horizontally or vertically linear polarized signals (Canada Centre for Remote Sensing, 2019). The single-, dual-, quad- and compact-pol options give different possible combinations of transmitted and received polarization channels. The possible options are summarized below, where the first character indicates the transmitting signal and the character the receiving:

- Linear single polarization (*single-pol*)
  - HH - horizontal transmit / horizontal receive

  - VV - vertical transmit / vertical receive
- Linear dual polarization (*dual-pol*)
  - HH and HV - horizontal transmit / horizontal and vertical receive
  - VV and VH - vertical transmit / vertical and horizontal receive
- Linear quadrature polarization (*quad-pol*)
  - HH, HV, VH and VV - horizontal and vertical transmit / horizontal and vertical receive
- CTLR polarization (*compact-pol*)
  - Right Circular Transmit, Linear Receive (CTLR): CH and CV - right-circular or left-circular transmit, horizontal and vertical receive

In this study, SAR data from different satellites were used: Sentinel-1, RADARSAT-2 and RCM. Table 2.2 shows the polarization configuration of each satellite. Depending on the settings and beam mode, single-, dual-, quad-, and/or compact-pol data are acquired by these satellites.

Table 2.2: Polarization options of Sentinel-1, RADARSAT-2 and RADARSAT Constellation Mission. Over land, Sentinel-1 acquires data in dual-pol modus. Depending on the used beam mode, RADARSAT-2 and RCM data acquire data with different polarizations. In this study, Sentinel-1 dual-pol data, RADARSAT-2 quad-pol data and RCM compact-pol data were used.

Sentinel-1	**RADARSAT-2**	**RCM**
Single-pol: VV	Single-pol: HH	Single-pol: HH Single-pol: VV
Dual-pol: VV and VH	Dual-pol: HH and HV	Dual-pol: HH and HV Dual-pol: VV and VH
	Quad-pol: HH, HV, VH and VV	Quad-pol: HH, HV, VH and VV
		Compact-pol: CH and CV

2.4.2. POLARIMETRIC THEORY

In the previous section, different polarization modes were introduced: single-pol, dual-pol, quad-pol and compact-pol. From the last two polarization modes, quad-pol and compact-pol, polarimetric information can be subtracted. For dual-pol data, semi-polarimetric data can be computed. This polarimetric information is encoded in a *scattering matrix* ***S***. For every pixel imaged by a quad-pol SAR, the scattering matrix is defined as

$$\mathbf{S} = \begin{bmatrix} S_{HH} & S_{HV} \\ S_{VH} & S_{VV} \end{bmatrix} \tag{2.8}$$

where the elements of the matrix represent the response of all scatterers for all combinations of input-output polarization. S_{ij} is a complex expression of the received electric field for transmit polarization i and receive polarization j (Henderson and Lewis, 1998). Hence, the first and second subscripts represent the transmitted and received signals respectively.

The scattering matrix of a single-pol or dual-pol SAR can be easily constructed based on Equation 2.8. For a single-pol SAR system that transmits and receives vertically polarized waves (VV), elements S_{HH}, S_{HV} and S_{VH} equal zero. For RCM compact-pol the first index i of the scattering elements should be replaced by the transmitted right-circular wave R.

In this study monostatic system configurations were used, i.e. transmitter and receiver are located at the same platform. For these systems, $S_{HV} = S_{VH}$ holds according to the reciprocity theorem (Lee and Pottier, 2009). The reciprocity constraints that the matrix is symmetrical for the cross-polarization channels, so $S_{HV} = S_{VH}$.

The scattering matrix cannot characterize distributed targets. For this purpose, polarimetric data sets can be translated into different matrix representations which contain a re-organized form of the scattering matrix S

(Henderson and Lewis, 1998). Hence, for many polarimetric interpretation methods not the scattering matrix S, but the *coviarance matrix* C and *coherency matrix* T are used. The covariance and the coherency matrices contain the same information, but this information comes in different forms (Qi et al., 2012).

The second order covariance and coherency matrices are formulated using the vectorised forms of the scattering matrix. For the covariance matrix the Lexicographic basis vector K_L is used (see Equation 2.9), for the construction of the coherency matrix the Pauli vector K_P (see Equation 2.10) (Cloude and Pottier, 1996). The target vectors are computed by

$$\mathbf{K}_L = \begin{bmatrix} S_{HH} & \sqrt{2}S_{HV} & S_{VV} \end{bmatrix}^T \tag{2.9}$$

$$\mathbf{K}_P = \sqrt{2}\begin{bmatrix} S_{HH}+S_{VV} & S_{HH}-S_{VV} & 2S_{HV} \end{bmatrix}^T \tag{2.10}$$

so that the covariance matrix C and coherency matrix T can be generated from the outer product of the basis vectors and its conjugate transpose (Lee and Pottier, 2009), with

$$\mathbf{C} = \mathbf{K_L} \cdot \mathbf{K_L}^{*T} \tag{2.11}$$

$$\mathbf{T} = \mathbf{K_P} \cdot \mathbf{K_P}^{*T} \tag{2.12}$$

For fully polarized SAR images, the covariance matrix has a dimension of 3x3 and is represented by

$$\mathbf{C}_3 = \begin{bmatrix} C11 & C12 & C13 \\ C21 & C22 & C23 \\ C31 & C32 & C33 \end{bmatrix} = \begin{bmatrix} |S_{HH}|^2 & \sqrt{2}S_{HH}S_{HV}^* & S_{HH}S_{VV}^* \\ \sqrt{2}S_{HV}S_{HH}^* & |S_{HV}|^2 & \sqrt{2}S_{HV}S_{VV}^* \\ S_{VV}S_{HH}^* & \sqrt{2}S_{VV}S_{HV}^* & |S_{VV}|^2 \end{bmatrix} \tag{2.13}$$

where matrix 2.13 contains the complete information of SAR data. Nevertheless, the covariance matrix C does not allow a physical interpretation. This is why the coherency matrix T is often preferred, because its elements are closely associated with physical and geometrical properties of the scattering process (Singh et al., 2019).

Like the covariance matrix, the coherency matrix contains nine elements and is constructed for every pixel in an image. The matrix has the following parameterisations (Cloude and Pottier, 1996)

$$\mathbf{T} = \frac{1}{2}\begin{bmatrix} |S_{HH}+S_{VV}|^2 & (S_{HH}+S_{VV})(S_{HH}-S_{VV})^* & 2(S_{HH}+S_{VV})S_{HV}^* \\ (S_{HH}-S_{VV})(S_{HH}+S_{VV})^* & |S_{HH}-S_{VV}|^2 & 2(S_{HH}-S_{VV})S_{HV}^* \\ 2(S_{HV}(S_{HH}+S_{VV})^*) & 2(S_{HV}(S_{HH}-S_{VV})^*) & 4|S_{HV}|^2 \end{bmatrix} \tag{2.14}$$

2.5. SUPERVISED CLASSIFICATION

Nowadays earth observation data are abundant. Machine learning derives knowledge from this data in order to make data-driven decisions and can be used to create a classifier. Within classification techniques, a distinction is made between *supervised* and *unsupervised* learning (Raschka and Mirjalili, 2017). Supervised classification involves the classification of pixels of unknown identity by means of a classification algorithm using characteristics of pixels of known classes (referred to as training data) (Campbell and Wynne, 2011). On the other hand, unsupervised classification involves the separation of image pixels into groupings based upon similar spectral characteristics by means of a classification algorithm. Consequently, the groupings are assigned to informational classes by the analyst (Enderle and Weih, 2005).

In this study, supervised classification is used, since it was considered important to select classes that represent features on the ground. Moreover, reference data from the observation flights of Alberta Environment and Parks were available, which included labels of the different ice stages.

2.5.1. MACHINE LEARNING TECHNIQUES

There are many supervised approaches in the field of machine learning and each technique has its advantages and disadvantages. *Skikit-Learn* is a Python library that contains a range of useful techniques for classification purposes and other machine learning tasks. Among these classifiers are:

- K-Nearest Neighbours
- Support Vector Machines
- Naive Bayes
- Linear Discriminant Analysis
- Logistic Regression
- Random Forest

Several supervised classifiers were compared in this study. This will not be further discussed in the main part of this thesis, however a comparison on the performance of different supervisors was made in Appendix C. The Random Forest model was evaluated as the best classifier over various types of data sets. Moreover, Random Forest classification has proven successful in other ice type and ice-water classification studies (e.g. Dabboor et al., 2018, Hoekstra et al., 2020, Shen et al., 2017).

For this study, besides the highest accuracies that were achieved in some tests, there are three other advantages of using a Random Forest classifier over other machine learning approaches. First of all, a Random Forest classifier is less affected by outliers and noise in a data set than other machine learning techniques, which is of great importance for SAR classification due to the presence of speckle noise in SAR images. Secondly, Random Forest classifiers can deal with many input features, which is necessary for this work since the importance of different intensity, polarimetric and texture features were studied. Finally, a Random Forest model is able to determine the importance of each feature (Hoekstra et al., 2020). This is of great importance for this study, since the added value of polarimetric and texture features is examined.

2.5.2. RANDOM FOREST CLASSIFIER

Random Forest (RF) classifiers are considered one of the most simple, yet most used machine learning classifiers.

RF classifiers use an ensemble learning method for classification problems. A RF-model consists of many building blocks, which are also known as decision trees. A decision tree is a very basic decision scheme based on split rules that categorize the data until certain criteria are met, see Figure 2.15.

A Random Forest model consists of a large number of individual decision trees that operate as a group. Rather than simply averaging the prediction of those trees, the model uses two random concepts: (1) random sampling of training data points when building trees and (2) random subsets of features considered when splitting nodes. The first key concept is also known as *bootstrapping*. During the training process, each tree in the Random Forest learns from a random sample of the data set. The samples are drawn with replacement, hence some samples will be used multiple times. The procedure of training each individual tree on different subsets on the data and then averaging the predictions is also known as *bagging* (bootstrap aggregating). The second concept that causes randomness, is that only a subset of all the features is considered for splitting a node (Liaw et al., 2002). These random elements create an ensemble model that combines the predictions from multiple algorithms together to make more accurate predictions than any individual model.

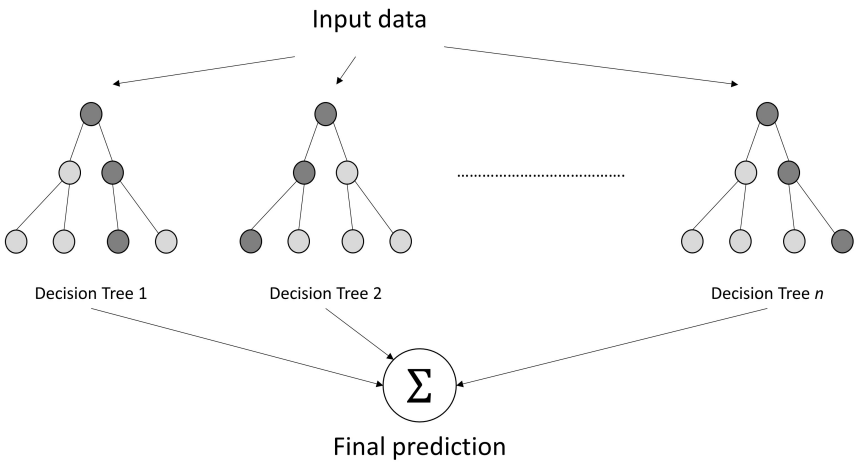

Figure 2.15: A conceptual illustration of a Random Forest model. After "planting" multiple independent decision trees, a RF takes a majority vote to predict a class.

2.5.3. OVERVIEW OF FEATURES

In machine learning, a feature is an individual measurable property of a phenomenon being observed. Choosing informative and discriminating features is a crucial step for effective algorithms in classification (Bishop, 2006).

Often river ice classifications are solely based on intensity features (e.g. Floyd et al., 2014, Gauthier et al., 2010, Sobiech and Dierking, 2013). This study aimed to get more out of the SAR data than co-pol backscatter alone and studied the added value of polarimetric and texture features.

In this section, an overview of the studied features is provided, including the calculations and their physical meaning. For each river ice stage (i.e. sheet ice, ice jam and open water) the feature value is estimated. In a later phase of this study, the hypothesized values and actual measurements are compared. In the subsections below, reasoning for the hypothesized values is provided. The matrix with hypothesized values can be found in Figure 2.16.

INTENSITY FEATURES

Backscatter intensity

The most commonly used feature in radar research is the backscatter intensity, which can be extracted from each SAR image. The pixel intensity values are often converted to a physical quantity called the *backscattering coefficient*. In remote sensing, the backscatter is commonly expressed in terms of sigma nought (σ^0), beta nought (β^0) or gamma nought (γ^0). In this study, the gamma nought backscattering coefficient was used to analyse and compare the intensities from the SAR images.

Sigma nought is the most basic backscattering coefficient and calibrates the backscatter returned to the SAR antenna from a unit area on the ground, and is thus related to ground range. This backscatter coefficient has a significant variation with incidence angle.

To correct for the effect of the incidence angle, the β^0 and γ^0 backscattering coefficients are used. *Beta nought*, also known as the radar brightness coefficient, is obtained when the ratio between the power transmitted and received by the antenna is computed. Beta nought is related to slant range. The last backscatter coefficient *gamma nought*, also known as terrain-flattened gamma nought, is computed when the reference area is defined to be in the plane perpendicular to the line of sight from a sensor to an ellipsoidal model of the ground surface. In theory this means that near range and far range cells are equally bright (Small, 2011).

Depending on the polarization channels used during a SAR acquisition, a different number of intensities can be extracted. For Sentinel-1 that operates in dual-pol, the VV and VH intensity are obtained. RADARSAT-2 quad-pol acquires the HH, HV, VH and VV channels. When RCM operates in compact-pol, two intensities are obtained, namely CH and CV.

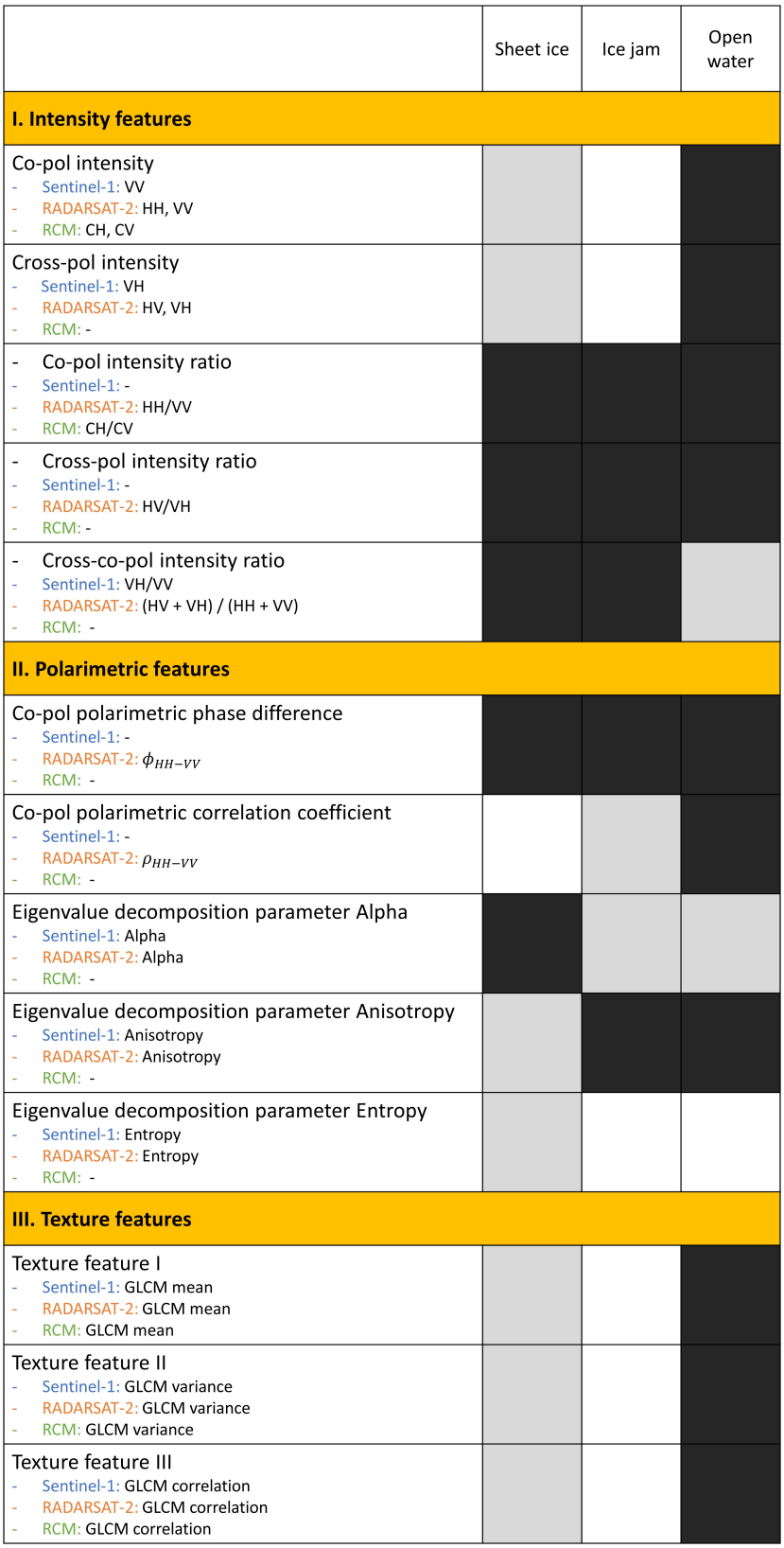

Figure 2.16: Hypothesized feature values for the three feature classes, i.e. intensity, polarimetric and texture features. An expected value for each feature is indicated, ranging from low (black) to high (white).

The used backscattering coefficient in this research, gamma nought, is obtained by normalising sigma nought with respect to the incidence angle. In this way some of the range-dependency of the sigma nought backscatter is removed. The standard formula to calculate sigma nought from the backscatter amplitude is (Rosenqvist and Killough, 2018):

$$\sigma^0 = DN^2 + K \tag{2.15}$$

where DN is the image pixel digital number measured in a SAR amplitude image. The unit of sigma nought is $[m^2/m^2]$, and can be expressed in decibel. K is a calibration factor that varies depending on the SAR sensor and processor system used.

From sigma nought, the terrain-flattened gamma nought backscatter coefficient can be computed by

$$\gamma^0 = \sigma^0 / \cos\theta_i \tag{2.16}$$

where the cosine of $theta_i$ is used to find the backscatter coefficient per unit projected area.

In this study, for simplicity reasons the intensities were divided into two groups: co-pol (HH, VV, CH, CV) and cross-pol (HV, VH). In order to accurately interpret the backscatter intensities, some understanding of the interaction of the radar signals with the river ice is required.

A strong *co-pol* backscatter intensity can be expected when (a combination of) specific scattering mechanisms occur. First of all, high gamma nought values are induced from *surface scattering*, for example when there is a direct scatttering from a surface that is facing the radar. Another surface scattering mechanism that results in a high co-pol backscattering intensity is diffuse scattering from a rough surface. Similar to direct scattering, a rough surface will have areas pointing to the sensor that causes part of the signal to be reflected back to the sensor. Also double-bounce scattering can cause a high co-pol backscatter. However, double-bounce scattering does not often occur during the breakup of river ice (Unterschultz et al., 2009). Secondly, also *volume scattering* can cause a high co-pol backscatter. When the radar signal gets reflected by an isotropic scatterer, this will result in an enhanced co-pol backscatter. The highest co-pol values are expected for ice jams, due to the rough surface and heterogeneous structure. Lowest values should be found for open water, since the wet surface impedes penetration and causes the incoming radar signal to scatter in a specular manner.

High *cross-pol* backscattering coefficients can be observed if the transmitted signal gets depolarized. *Depolarization* occurs when a radar signal gets reflected from very rough surfaces or from anisotropic or multi-bounce volume scattering. Therefore, the highest cross-pol values are expected for ice jams.

Intensity ratio
Ratios between two individual intensities could give additional information about the target. Based on the pixel intensity values, the ratios between co- and cross-polarization can be computed. In the case of a quad-pol acquisition, the co-polarization ratio is HH/VV and the cross-polarization ratio is HV/VH. According to the reciprocity theorem HV and VH are equal (Lee and Pottier, 2009). However, the ratio between HV and VH is sometimes computed as well, to see if there is a difference that might provide extra information about the target. Finally, the cross-co-pol ratio can be computed, which describes the amount of cross-pol (HV or VH) compared to co-pol (HH or VV) intensity.

The ratio between two polarization channels in arbitrary *xy* polarization can be expressed as

$$R_{xx-yy} = \frac{S_{xx}S^*_{xx}}{S_{yy}S^*_{yy}} \tag{2.17}$$

When one has interest in the ratio between the co-pol elements, the *xx* can be replaced by *HH*, the *yy* can be replaced by *VV*. Similarly, the cross-pol ratio can be determined by replacing *xx* by *HV* and *yy* by *VH*. The

depolarization is determined as the ratio of cross-pol to both co-pol channels, where the numerator equals 2^*S_{HV}, and the denominator $S_{HH}S^*_{HH}+S_{VV}S^*_{VV}$. For dual-pol sensors, the depolarization ratio holds xy/xx.

The co-pol, cross-pol and cross-co-pol ratio may provide different information. In this study, it is expected that the *co-pol* and *cross-pol* ratios will not provide additional information about the target, because it is hypothesized that both HH and VV as HV and VH will behave the same for the different ice stages.

On the other hand, cross-co-pol intensity ratios may provide additional information about an observed target. Complex surfaces or anisotropic or multiple-scattering surface layers cause a signal to depolarize. However, very rough surfaces like ice jams have a very high co-pol (i.e. HH or VV) intensity as well. Therefore, even though the cross-pol intensity of ice jams is high, it is expected that they will have a low cross-co-pol ratio.

POLARIMETRIC FEATURES

Polarimetric phase difference

The phase of a returned EM wave is recorded by polarimetric sensors and contains information about the timing of one wave relative to another wave. When two EM waves are in phase, the phase difference equals zero. When one polarization channel is delayed upon return as a result of interaction with the river ice, the phase difference does not equal zero. The relative differences in phase between received polarimetric channels are interesting. For each scattering event, the relative phase of waves is transformed. Therefore, the polarimetric phase difference may provide additional information about an observed target.

Quad- and compact acquisitions measure the phase difference between the received backscatter signals of the different polarization channels. The relative phase difference between HH and VV of a quad-pol acquisition, can be unequal to zero, which possibly provides additional information about the observed target.

The relative phase difference between HH and VV, also expressed as Φ_{HH-VV}, can be computed based on the covariance matrix:

$$\Phi_{HH-VV} = atan(imag[(S_{xx}S^*_{xx}) * conj(S_{yy}S^*_{yy})], real[(S_{xx}S^*_{xx}) * conj(S_{yy}S^*_{yy})]) \tag{2.18}$$

were *conj* in the complex conjugate and $S_{xx}S^*_{xx}$ and $S_{yy}S^*_{yy}$ are the complex values of the requested polarizations. The results are returned in degrees or radians.

Different phase features can be analyzed, namely the co-pol phase difference (i.e. HH and VV) and the cross-pol phase difference (i.e. HH and HV or VV and VH). The phase difference between HV and VH is assumed to be zero (reciprocity theory). The cross-pol phase difference is usually random, as there is little correlation between the scattering phase centres of the co-pol and cross-pol channels.

On the other hand, the co-pol phase difference may provide information about the observed target, as is characterizes the number of bounces that an EM wave experiences during reflection. Difference in phase between the co-pol channels can be caused by many scattering mechanisms, including (1) single or odd bounce surface scattering, (2) volume scattering or (3) double-bounce surface scattering (Ulaby et al., 1986). When a backscattered signal only consists of surface scattering, the co-pol phase difference generally equals zero. Conversely, double bounce scatterers of vertical cylinders increase phase difference to a maximum of 180° (Ulaby et al., 1986).

The relative phase difference can vary between -180° and 180°. An ideal single bounce scatterer will have a co-pol difference of 0°, while an ideal double bounce scatterer will have a phase difference of 180°. In practical situations, the co-pol phase difference has a value somewhere between 0° and 180°. An ice sheet is relatively flat, which means few multi-bounce scattering will occur. For flat surfaces, a co-pol phase difference near 0° is expected.

Polarimetric correlation coefficient

Already in 1991 Drinkwater et al. (1991) concluded that additional phase information, embedded in the correlations between the different polarization channels, is important information for ice classification. Later it was found that the correlation between the co-polarization channels HH and VV provides most information (Eriksson et al., 1998).

The polarimetric correlation coefficient is defined as the complex correlation between two polarization channels. A correlation coefficient is a complex number. It is computed as the average of the product between the complex amplitude of arbitrary channel *xx* and the conjugate of the complex amplitude of arbitrary channel *yy*. The coefficient is normalized by the square root of the products of the powers in *xx* and *yy* (Quegan, 1994). The correlation coefficient in arbitrary *xy* polarization basis can be expressed as

$$\rho_{xxyy} = \frac{S_{xx}S_{yy}^*}{\sqrt{S_{xx}S_{xx}^*} * \sqrt{S_{yy}S_{yy}^*}} \tag{2.19}$$

where ρ_{xxyy} is a complex number (Ainsworth et al., 2008). The magnitude of the correlation coefficient can be determined by

$$\mid \rho_{xxyy} \mid = \sqrt{\rho^2_{xxyy_{real}} + \rho^2_{xxyy_{imag}}} \tag{2.20}$$

where the square root of the product of the real and imaginary part of the complex ρ_{xxyy} is taken. Then the correlation coefficient between two co-polarized channels in the linear polarization basis can be obtained by replacing *xx xx* by *HH* and *yy* by *VV*. The same can be done when the correlation coefficient between the co-polarized and cross-polarized channels is desired, for example by replacing *xx* by *HH* and *yy* by *HV*.

If the magnitude of the correlation coefficient equals one, the received signal from the two channels is linearly correlated. This can be expected when a backscatter is received from a corner reflector. If the magnitude is less than one, this means that the channels *xx* and *yy* are not directly related. For the co-polarized correlation coefficient, this can be the case when there is a different amount of depolarization for the transmitted H and V waves.

The correlation coefficient of the co-polarized channels ρ_{HHVV} is related to the scattering mechanism. When a surface is very rough, which is the case for ice jams, it is expected that the correlation coefficient is lower, as the dominant scattering mechanism is odd-order scattering (Mermoz et al., 2009).

Eigenvalue decomposition parameters

Decomposition is a broad class of strategies that have proven to be useful for the classification of radar backscatter (Cloude and Pottier, 1996). There are many different polarimetric decomposition methods that allow the separation of scattering contributions and can be used to extract information about the scattering processes (Lee et al., 1999). Decomposition methods reduce all the information that is contained in the covariance or coherency matrix into a small set of descriptors of the scattering mechanisms on the ground.

For fully polarized data, such as quad-pol RADARSAT-2 data product, a 3x3 matrix is used. For Sentinel-1 dual-pol data, pseudo decomposition parameters can be extracted based on a 2x2 matrix. Recently, also decomposition methods for compact-pol data were developed. However, compact-pol data have a 2x2 matrix, instead of a 3x3 matrix. To deal with this differently sized matrix, two options were developed in order to apply decomposition on compact-pol data. The first method is to expand the 2x2 matrix to a pseudo 3x3 matrix. Such an operation depends on certain symmetry assumptions that cannot be met in all cases. An alternative decomposition methodology for compact-pol radar data is based on the four-element Stokes vector (Charbonneau et al., 2010). Unfortunately, no decomposition parameters of compact-pol RCM data were computed, since only Ground Range Detected Georeferenced (GRD) data were available for this project, in which phase information is lost.

Cloude and Pottier (1997) developed the *H*-*A*-α decomposition method that is widely used for polarimetric SAR data (Mermoz et al., 2009). The H-A-α decomposition method is based on the eigenvalue and eigenvector analysis of the coherency matrix. The method divides the polarimetric data into scattering entropy (*H*), anisotropy (*A*) and alpha (α) (Zhang et al., 2018). Cloude and Pottier (1997) divided the feature spaces of *H* and α into eight effective areas, each of which corresponded to a specific scattering mechanism. Based on the feature spaces, the scattering mechanism (surface, volume, and double-bounce scattering) can be extracted (Cloude and Pottier, 1997).

The parameters of the *H-A-α* decomposition are based on the eigenvalues λ_1, λ_2 and λ_3 of the coherency matrix, where $\lambda_1 > \lambda_2 > \lambda_3 > 0$. The eigenvectors u_1, u_2 and u_3 can be expressed as follows

$$u_i = \begin{bmatrix} cos(\alpha_i), & sin(\alpha_i)cos(\beta_i)e^{j\delta} & sin(\alpha_i)cos(\beta_i)e^{j\gamma} \end{bmatrix}^T \tag{2.21}$$

where parameter α_i is directly related to the incidence angle and the DC, with i ranging from 1 to 3. Parameters δ_i and γ_i are phase angles characteristic of the target material.

The first part of the decomposition deals with *entropy* (H) and can be expressed as follows

$$H = \sum_{k=1}^{3} p_i log_3(p_i) \tag{2.22}$$

with $P_i = \lambda_i \,/\, \sum_{k=1}^{3} \lambda_k$. The eigenvalues are used to calculate entropy and are a function of the noise that is caused by the depolarization. If the entropy is close to zero, the signal is likely to be dominated by a single scattering mechanism. On the other extreme, if the entropy value is close to one, all scattering mechanisms are equally likely to be found in the received signal (Cloude and Pottier, 1997).

The second part of the decomposition refers to *anisotropy* (A), which also ranges from 0 to 1 and can be taken to complement H. Polarimetric anisotropy is defined as

$$A = \frac{\lambda_2 - \lambda_3}{\lambda_2 + \lambda_3} \tag{2.23}$$

Anisotropy provides information on the relative importance of secondary scattering mechanisms (surface / volume / double-bounce scattering). When A is higher, only the second scattering process is in play. When A is lower, the first scattering mechanism is dominant and the second and third mechanisms are equally important (Xie et al., 2018).

The last part of the decomposition method deals with α, which is an angle that ranges from 0 to 90 degrees. Angle α is given by

$$\alpha = \sum_{k=1}^{3} p_i \alpha_i \tag{2.24}$$

Angle α represents the dominant scattering mechanism in a pixel. When α gets close to zero, surface scattering is the dominating scattering mechanism. When a value approaches 45 degrees, the signal is controlled by volume scattering. For α values close to 90 degrees, the double bounce scattering is most dominant (Cloude and Pottier, 1997).

TEXTURE FEATURES

Everyday texture generally refers to a topographical surface with high and low points. Image texture works in the same way, except that the high and low values relate to the brightness values instead of elevation changes. These brightness values are called digital numbers (DN) or image tones (Hall-Beyer, 2000).

Texture information can be extremely useful for the classification of SAR images. In SAR image, texture can be used to show the intensity variation in an image. It includes information from neighbouring pixels, which is important to characterize the different ice stages that have specific spatial patterns.

In 1976, Haralick and Bryant (1976) proposed the Gray Level Co-occurence Matrix (GLCM) to compute texture features. Currently, this is one of the most widely used methods to compute texture features. Since they were

first used by Holmes et al. (1984), textural features have proven to be useful in ice classification (e.g. Barber and LeDrew, 1991, Gauthier et al., 2006, Soh and Tsatsoulis, 1999).

Several texture features can be computed from the GLCM, which can be divided into a statistic, contrast and orderliness group:

1. Statistic group: mean, variance, correlation
2. Contrast group: contrast, dissimilarity, homogeneity
3. Orderliness group: applied second moment, entropy, inverse moment

For this study, only features from the *statistic* texture group were considered. *GLCM mean* is the probability that two pixels are neighbours. *GLCM variance* is associated with values that highly differ from the mean. *GLCM correlation* is a measure of linear dependence between neighbouring pixels. The GLCM statistics features differ from common descriptive statistics, such as mean and variance, because they are second order instead of first order statistics. The GLCM features are calculated using the GLCM and not the original pixel values. The GLCM expression is computed by

$$p(i,j,d,\theta) = \{[(x,y),(x+D_x,y+d_y)|f(x,y)] = i; f(x+D_x,y+d_y) = j; x(y) = 0,1,2,...N_{x(y)}]\} \tag{2.25}$$

where i,j={0,1,...,N_g-1} are the set of quantized gray levels. The pixel coordinate is given by *(x,y)*. Then N_x and N_y are the columns and the rows and D_x and D_y are the horizontal and vertical offsets. d is the interval distance between reference pixels and neighbouring pixels. Since this equation is relatively difficult to understand, an example is provided in Figure 2.17 to illustrate the production of the GLCM.

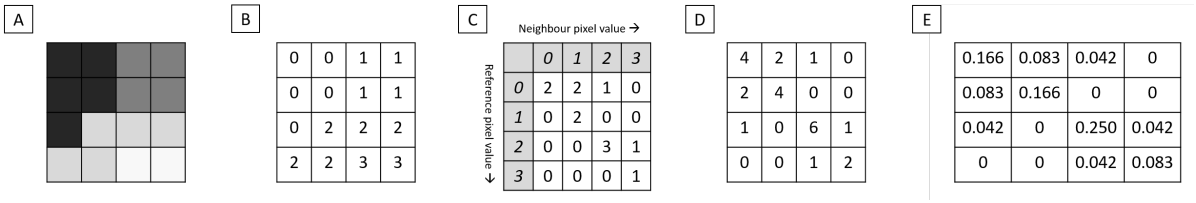

B			
0	0	1	1
0	0	1	1
0	2	2	2
2	2	3	3

C	0	1	2	3
0	2	2	1	0
1	0	2	0	0
2	0	0	3	1
3	0	0	0	1

D			
4	2	1	0
2	4	0	0
1	0	6	1
0	0	1	2

E			
0.166	0.083	0.042	0
0.083	0.166	0	0
0.042	0	0.250	0.042
0	0	0.042	0.083

Figure 2.17: Explanation of the computation of the Gray Level Co-occurence Matrix (GLCM) in east direction with an offset of one pixel. The first image [A] represents the intensity values of a SAR image. In step [B], the gray-scale SAR image is represented by discrete values. The third figure [C] shows that the number of co-occurences of pixel pairs for a given search window is counted and a GLCM is produced with an east spatial relationship. In image [D] the GLCM is made symmetrical by adding it to its transpose. In the final image [E] the matrix is normalized.

GLCM texture considers the relation between two pixels at a time, which are called the *reference* and the *neighbour* pixel (Hall-Beyer, 2000). In the example presented in Figure 2.17 the neighbour pixel is chosen to be the one right from the reference pixel. In the example, an offset of one ($d = 1$) was selected. In reality, the computation can be more complicated, since the distance between the reference and neighbour pixel can also be larger than one and more directions can be chosen.

The GLCM is constructed by counting the number of pixel pairs that show a combination of all possible value pairs (Hall-Beyer, 2000). In the first cell, i.e. [0,0], the amount of occurrences is counted and tabulated for which a reference pixel with the value 0 has a neighbouring pixel that was 0 as well. In the example presented in Figure 2.17 [C] this combination occurred two times.

Texture calculations perform better when the GLCM is symmetrical. To make the matrix symmetrical, a transposed copy of the GLCM should be created and added the GLCM itself, see 2.17 [D]. The final step is to normalize the GLCM, which can be achieved by dividing each element by the sum of all elements as was done in Figure 2.17 [E]. The elements in this final GLCM may now be considered probabilities of finding all reference-neighbour pixel relationships (Hall-Beyer, 2000).

3

STUDY AREA AND DATA DESCRIPTION

In the previous chapter background information on river ice and remote sensing was provided. In this chapter, the study area is introduced. The area of interest for this research is the Athabasca River, a dynamic river known for its many stages of ice types during the winter season. Besides this study area, descriptions of the used SAR and reference data are provided.

3.1. ATHABASCA RIVER, ALBERTA

The Athabasca River is the longest river of Alberta, the fourth-largest province of Canada. It originates along the border of British Colombia and Alberta, in a large icefield of the Rocky Mountains, and then travels 1538 km through the province of Alberta to eventually mouth in Lake Athabasca. As the river flows northeast through Alberta, it passes several towns, like Jasper, Hinton, Whitecourt, Athabasca and Fort McMurray (Alberta Environment, 2010).

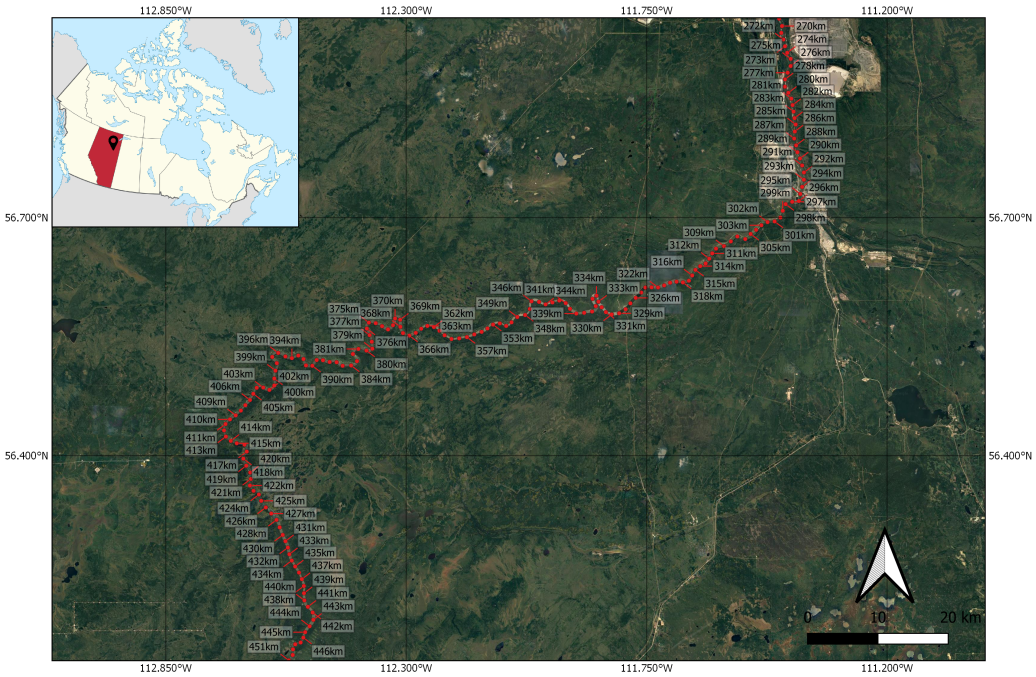

Figure 3.1: The study reach of the Athabasca River. The river flows from south-west to north-east. This stretch of the Athabasca River is very prone to ice jams, due to its dynamic morphology in this reach. Ice jams occur almost every year, which destroyed parts of the upstream located city Fort McMurray many times throughout history.

For this research, the study site is a river stretch of approximately 160 km, extending from the House River (km 445) to approximately 10 km downstream of the Clearwater River (km 285), see Figure 3.1. The width of the river from upstream Grand Rapids (445 km) to upstream of the city of Fort McMurray (285 km) varies from approximately 400 to 900 m, and the channel slope varies from 0.001 m/m up to 0.0003 m/m (Lindenschmidt et al., 2011).

The reach upstream of Fort McMurray is particularly steep, narrow and sinuous, alternating with several rapids, which makes this stretch conducive to a thick ice cover during winter and to sequences of ice jamming and release during breakup. Downstream of Fort McMurray the river bed is flatter and the river is wider. In this part, several islands can be found, which may arrest the ice flow and provide locations for ice jams. The inflow from the Clearwater River provides an additional source of ice and water (Lindenschmidt and Li, 2019).

As a result of the dramatic change in the character of the Athabasca River upstream of Fort McMurrray, severe ice jams form at Fort McMurray during breakup. Documentation of ice jam events on the Athabasca River near Fort McMurray dates back to the 19th century. In 1875 the most dramatic ice jam event occurred, during which the water level was reported to have risen 12 meters in less than half an hour (Hutchison and Hicks, 2007). Other significant ice jam events that have produced water levels in the order of 10 meters above the normal open water stage, were reported in 1977, 1978, 1979 (Andres and Doyle, 1984) and this year (2020).

Because of the ongoing risk of ice jam flooding in Fort McMurray, Alberta Environment and Parks (AEP) has an annual river ice monitoring and observation program for the Athabasca River upstream of Fort McMurray (Sun et al., 2015). The data obtained based on on-site measurements by permanents cameras and observation flights operated and conducted by AEP facilitated the implementation of this study. Based on their observations, the two breakup seasons that were studied in this research are discussed in the next sections.

3.1.1. BREAKUP SEASON 2018-2019

Thermal deterioration of the ice cover began in the last two weeks of March 2019. On the observation flight of April 8 the ice cover was mostly intact, but there were some open leads located at the rapids. By April 9, the deterioration had continued. The ice cover upstream of Crooked Rapids (km 335) had broken up, resulting in ice runs in downstream direction. An intact ice cover persisted between Crooked Rapids (km 335) and Fort McMurray (km 285), which obstructed flowing ice and resulted in the formation of a 16 km long ice jam. Upstream of the ice jam, the Athabasca River was almost free of ice, whereas downstream of the ice jam an intact ice cover remained. The observation flights of the coming days showed a thermal breakup of the ice cover downstream of the ice jam. On April 12, the ice jam that had formed between km 307 and km 322, started to shrink. The length of the ice jam melted from 15 km on April 14 to 13 km on April 15. The ice jam was melted completely on April 20. Two days later, on April 22, the entire river stretch of interest was open again.

3.1.2. BREAKUP SEASON 2019-2020

In 2020, the Athabasca River breakup started in mid-April, when the ice cover upstream of Crooked Rapids (km 335) showed signs of thermal deterioration by April 21. This gradual decay continued and no major changes were noted until an ice run was observed by AEP stationed just downstream of km 380, on April 24. On the next day, AEP noted a 20 km long ice jam that had formed just upstream of the city of Fort McMurray. The following day, the ice jam was still in place and water levels downstream and in the Clearwater River started to increase. On April 26, the ice jam had lengthened and was slightly moved, now being located between 285 km and 305 km, running right through the city of Fort McMurray. The ice jam caused water levels to rise by 4.5 to 6 meters across low-lying areas. Between April 26 and May 2, approximately 13000 people had to be evacuated. Over a thousand structures were damaged in the flood, leading to over 522 million in insured damages, as was reported by the Insurance Bureau of Canada (Insurance Bureau Canada, 2020). From May 2 on, the river was free of ice.

3.2. DESCRIPTION OF SAR DATA

For this study, SAR data from Sentinel-1, RADARSAT-2 and the RADARSAT Constellation Mission were used. All three satellite missions carry a single C-band synthetic aperture radar instrument operating at a centre frequency of 5.405 GHz. Other properties like revisit time, spatial resolution and polarization modes differ per mission and are introduced in the sections below.

3.2.1. SENTINEL-1

The Sentinel-1 mission is a constellation of two polar-orbiting satellites launched in April 2014 - Sentinel-1A - and in April 2015 - Sentinel-1B. The Sentinel-1 satellite constellation acquires data in single and dual polarization with a revisit time of 6 days at the equator (Torres et al., 2012). In case of Fort McMurray revisit time ranges from 3 to 4 days.

The system potentially operates in four acquisition modes: Interferometric Wide swath (IW), Stripmap (SM), Extra-Wide swath (EW) and Wave (WV). The Sentinel-1 images used for this study were acquired in IW imaging mode, which is the primary conflict-free mode over land. The IW data products have a 250 km swath at 5 m by 20 m resolution and dual polarization capabilities (VV and VH) (Torres et al., 2012).

The Sentinel-1 mission provides different types of products, which are available in "raw" Level-0 data, and "SAR processed" Level 1/2 data. For this study the Level-1 data were used, the most unprocessed product that is available to the public. Sentinel-1 Level 1 data are distributed by the Copernicus Open Access Hub under two product types: Single Look Complex (SLC) and Ground Range Detected Georeferenced (GRD).

The GRD products consist of data that have already been detected, multi-looked and projected to ground range using an Earth ellipsoid model. GRD images only contain amplitude data, the phase information is discarded. The SLC data product on the other hand preserves the phase information (Potin, 2013). Also, the user has control over all the desired preprocessing steps. The additional phase information and control over the entire preprocessing scheme made the SLC images the desired product for this study.

Table 3.1 presents a description of the data products that were used for this study. Seventeen Sentinel-1 images were studied, eight from breakup season 2018-2019 and nine from 2019-2020. Half of the images were acquired by S1A and the other half by S1B. The sensor characteristics are comparable, but the orbit and overpass time differ per product.

3.2.2. RADARSAT-2

RADARSAT-2 was launched in December 2007 as a follow-on to RADARSAT-1 which mission terminated in April 2013. Like Sentinel-1, RADARSAT-2 also operates in C-band. The satellite offers full flexibility in the selection of polarization options. The sensor can obtain images with different models, obtaining images from 1 m to 100 m resolution and covering an area ranging from 20 km x 20 km to 500 km x 500 km (Girard et al., 2002).

RADARSAT-2 data is not freely available. For this study, the data were requested to the Canadian Space Agency and offered for single use. Same as for the Sentinel-1 data, the SLC products were used, which gives freedom for the preprocessing. Table 3.2 shows the used data products, the SAR characteristics like beam mode, resolution, orbit and overpass time differ per acquisition.

3.2.3. RADARSAT CONSTELLATION MISSION

The recently launched RADARSAT Constellation Mission is a follow-up on the RADARSAT program (RADARSAT-1 and RADARSAT-2), launched in June 2019. The constellation consists of three satellites, evenly spaced on the same orbital plane. The exact repeat cycle per satellite is twelve days, hence the repeat time of the constellation mission equals four days. Like Sentinel-1 and RADARSAT-2, the RCM carries a C-band SAR at the same frequency (5.405 GHz) (Thompson, 2015).

The main product of RCM system is the circular-linear compact polarimetric mode, in this study abbreviated as compact-pol. The compact-pol data used in this study consists of a right hand circular transmit and linear/circular receive radar signal. Besides the compact-pol mode, RCM can also transmit and receive radar signals of the conventional linear polarization channels (Geldsetzer et al., 2015).

Unlike RADARSAT-2 data, certain RCM data products are completely open for public, both for Canadian and non-Canadian citizens. GRD data products from a resolution lower than 16 meters could be achieved. Because RCM was launched mid-2019, only the 2019-2020 breakup of the Athabasca River was analysed. An overview of the used RCM data is presented in Table 3.3.

Table 3.1: Sentinel-1 data products that were used for this study.

ID	Local date	Local time	Beam mode	Orbit	Polarization	Inc. Angle	Resolution	Swath width
S1-AR19-1	12-Mar-2019	07:45:22	IW	Asc	Dual-pol	29°- 46°	5 x 20 m	250 km
S1-AR19-2	16-Mar-2019	19:15:09	IW	Des	Dual-pol	29°- 46°	5 x 20 m	250 km
S1-AR19-3	24-Mar-2019	07:45:22	IW	Asc	Dual-pol	29°- 46°	5 x 20 m	250 km
S1-AR19-4	28-Mar-2019	19:15:10	IW	Des	Dual-pol	29°- 46°	5 x 20 m	250 km
S1-AR19-5	5-Apr-2019	07:45:22	IW	Asc	Dual-pol	29°- 46°	5 x 20 m	250 km
S1-AR19-6	9-Apr-2019	19:15:10	IW	Des	Dual-pol	29°- 46°	5 x 20 m	250 km
S1-AR19-7	17-Apr-2019	07:45:22	IW	Asc	Dual-pol	29°- 46°	5 x 20 m	250 km
S1-AR19-8	21-Apr-2019	19:15:11	IW	Des	Dual-pol	29°- 46°	5 x 20 m	250 km
S1-AR20-1	18-Mar-2020	07:45:54	IW	Asc	Dual-pol	29°- 46°	5 x 20 m	250 km
S1-AR20-2	22-Mar-2020	19:15:43	IW	Des	Dual-pol	29°- 46°	5 x 20 m	250 km
S1-AR20-3	30-Mar-2020	07:45:54	IW	Asc	Dual-pol	29°- 46°	5 x 20 m	250 km
S1-AR20-4	3-Apr-2020	19:15:42	IW	Des	Dual-pol	29°- 46°	5 x 20 m	250 km
S1-AR20-5	11-Apr-2020	07:45:55	IW	Asc	Dual-pol	29°- 46°	5 x 20 m	250 km
S1-AR20-6	15-Apr-2020	19:15:43	IW	Des	Dual-pol	29°- 46°	5 x 20 m	250 km
S1-AR20-7	23-Apr-2020	07:45:55	IW	Asc	Dual-pol	29°- 46°	5 x 20 m	250 km
S1-AR20-8	27-Apr-2020	19:15:43	IW	Des	Dual-pol	29°- 46°	5 x 20 m	250 km
S1-AR20-9	5-May-2020	07:45:56	IW	Asc	Dual-pol	29°- 46°	5 x 20 m	250 km

Table 3.2: RADARSAT-2 data products that were used for this study.

ID	Local date	Local time	Beam mode	Orbit	Polarization	Inc. Angle	Resolution	Swath width
R2-AR19-1	12-Mar-2019	18:50:37	SQ2W	Asc	Quad-pol	19.0°- 22.7°	27.2 x 23.4 m	50 km
R2-AR19-2	15-Mar-2019	19:03:06	SQ12W	Asc	Quad-pol	30.6°- 33.7°	26.5 x 24.3 m	50 km
R2-AR19-3	22-Mar-2019	7:32:22	SQ27	Des	Quad-pol	45.2°- 46.5°	19.0 x 18.6 m	18 - 25 km
R2-AR19-4	28-Mar-2019	7:57:25	SQ5W	Des	Quad-pol	22.5°- 26.0°	23.6 x 20.6 m	50 km
R2-AR19-5	29-Mar-2019	7:28:12	SQ31	Des	Quad-pol	48.3°- 49.4°	18.1 x 17.7 m	18 - 25 km
R2-AR19-6	5-Apr-2019	18:50:34	SQ2W	Asc	Quad-pol	19.0°- 22.7°	27.2 x 23.4 m	50 km
R2-AR19-7	8-Apr-2019	19:03:06	SQ12W	Asc	Quad-pol	30.6°- 33.7°	26.5 x 24.3 m	50 km
R2-AR19-8	14-Apr-2019	8:01:34	SQ2W	Des	Quad-pol	19.0°- 22.7°	27.2 x 23.4 m	50 km
R2-AR19-9	15-Apr-2019	7:32:22	SQ27	Des	Quad-pol	45.2°- 46.5°	19.0 x 18.6 m	18 - 25 km
R2-AR19-10	21-Apr-2019	7:57:24	SQ5W	Des	Quad-pol	22.5°- 26.0°	23.6 x 20.6 m	50 km
R2-AR19-11	22-Apr-2019	7:28:12	SQ31	Des	Quad-pol	48.3°- 49.4°	18.1 x 17.7 m	18 - 25 km

Table 3.3: RADARSAT Constellation Mission data products that were used for this study.

ID	Local date	Local time	Beam mode	Orbit	Polarization	Inc. Angle	Resolution	Swath width
RCM-AR20-1	8-Apr-2020	7:49:44	Stripmap	Des	Compact-pol	35.2°– 37.4°	16 m	30 km
RCM-AR20-2	8-Apr-2020	19:19:21	Stripmap	Asc	Compact-pol	45.6°- 47.2°	16 m	30 km
RCM-AR20-3	9-Apr-2020	18:55:49	Stripmap	Asc	Compact-pol	24.2°- 26.8°	16 m	30 km
RCM-AR20-4	12-Apr-2020	7:49:56	Stripmap	Des	Compact-pol	35.2°– 37.3°	16 m	30 km
RCM-AR20-5	12-Apr-2020	19:19:33	Stripmap	Asc	Compact-pol	22.5°- 26.0°	16 m	30 km
RCM-AR20-6	13-Apr-2020	7:57:56	Stripmap	Des	Compact-pol	24.2°- 26.7°	16 m	30 km
RCM-AR20-7	13-Apr-2020	18:55:53	Stripmap	Asc	Compact-pol	24.2°- 26.7°	16 m	30 km
RCM-AR20-8	16-Apr-2020	7:49:33	Stripmap	Des	Compact-pol	35.2°- 37.3°	16 m	30 km
RCM-AR20-9	16-Apr-2020	19:19:44	Stripmap	Asc	Compact-pol	45.6°- 47.2°	16 m	30 km
RCM-AR20-10	17-Apr-2020	18:55:18	Stripmap	Asc	Compact-pol	24.2°- 26.7°	16 m	30 km
RCM-AR20-11	20-Apr-2020	7:49:45	Stripmap	Des	Compact-pol	35.2°– 37.3°	16 m	30 km
RCM-AR20-12	21-Apr-2020	18:55:42	Stripmap	Asc	Compact-pol	24.2°- 26.7°	16 m	30 km
RCM-AR20-13	22-Apr-2020	8:03:03	ScanSAR	Des	Compact-pol	17.3°– 28.5°	30 m	125 km
RCM-AR20-14	24-Apr-2020	7:49:56	Stripmap	Des	Compact-pol	35.2°– 37.3°	16 m	30 km
RCM-AR20-15	24-Apr-2020	19:19:33	Stripmap	Asc	Compact-pol	45.6°- 47.2°	16 m	30 km
RCM-AR20-16	25-Apr-2020	7:57:56	Stripmap	Des	Compact-pol	24.2°- 26.7°	16 m	30 km
RCM-AR20-17	25-Apr-2020	18:55:53	Stripmap	Asc	Compact-pol	24.2°- 26.7°	16 m	30 km
RCM-AR20-18	27-Apr-2020	7:41:27	ScanSAR	Des	Compact-pol	40.7°- 48.0°	30 m	125 km

3.3. DESCRIPTION OF REFERENCE DATA

It is important to have areas with well-known ice stages in order to create a reliable data set for training and validation of the river ice classification. In this study sample areas were classified as sheet ice, ice jam or open water. The labels of the training and validation data sets were based on ground observation (trail cameras), aerial surveys (helicopter or fixed-wing airplane) and space-born remote sensing (optical imagery). A brief description of these data products is provided below.

3.3.1. OBSERVATION FLIGHTS AEP

Ice cover breakup monitoring is carried out every spring by scientists and engineers from Alberta Environment and Park's (AEP) River Forecasting Centre. One of their main sources of information are observation flights, which they execute almost daily during breakup season. Most of their flights are carried out between km 285 and km 445, which explains the choice for the selected study area in this research.

The ice progression maps and ice observation reports from the AEP observation flights that were used in this study, are archived and can be accessed at *https://rivers.alberta.ca/*. Immediately after an observation flight, their monitoring reports are released on their website. An overview of the ice progression during the breakup seasons 2018-2019 and 2019-2020 is provided in Appendix A.1. The photos that were taken during the observation flights, were sent by personal communication.

The time difference between SAR images and observation flights ranged from 3 hours to 1.5 days. The AEP ice progression maps and observation reports were mainly used as reference data when the time differences between the SAR acquisition and flight were small. However, through personal communication with ice experts of AEP, it could be confirmed that for some dates certain ice stages were stationary for a longer period of time. This enabled the use of AEP monitoring data, also when time differences were larger, for example one day.

3.3.2. WEBCAM IMAGERY

The second source of reference data used in this study are webcam photos. Along the researched study stretch, different webcam cameras are located. AEP facilitates one camera which is installed at km 334.6, just upstream of Crooked Rapids. This camera was programmed to take pictures every hour. Photos acquired during breakup season 2018-2019 and 2019-2020 were sent by personal communication.

Only for a small stretch of the river webcam imagery could be used as reference data, as the camera images an area of several tens of meters. However, there was a high confidence in the correct river ice stage labels close to Crooked Rapids, since the time difference between webcam photography and a SAR acquisition was maximum one hour.

3.3.3. OPTICAL IMAGERY SENTINEL-2

The last source of reference data used in this study is Sentinel-2 optical images. The Sentinel-2 satellite series, consisting of two satellites, may further enhance river ice monitoring. The first of the satellites, Sentinel-2A, was launched in June 2015. Sentinel-2B was launched two years later in 2017.

The orbit repeat rate of the satellites combined is five days. Both Sentinel-2 satellites operate the MultiSpectral Instrument, which has a 10 meter spatial resolution. Compared to other optical satellites (e.g. Landsat-8 that has a 30 meter resolution), this enhances monitoring on a fine scale.

Even though in theory the Sentinel-2 satellites provide great opportunities for river ice monitoring, cloudiness is the main limitation of space-borne optical imagery. Especially during breakup season, most images cannot be used. An overview of the images that were acquired in the studied breakup seasons, is provided in Appendix A.2. The Sentinel Hub Playground tool (*https://apps.sentinel-hub.com/sentinel-playground/*) was used for quick visualization of Sentinel-2 imagery.

4

METHODOLOGY

In the previous chapter, the study area was introduced and a description of the data products was provided. Consequently, in this chapter the method is derived that was followed to answer the research question: what are the classification potentials and limitations of Sentinel-1, RADARSAT-2 and RCM for river ice during breakup.

4.1. GENERAL APPROACH

This research follows a step-by-step approach that starts with the preparation of the SAR data, which includes downloading and preprocessing. This is explained in Section 4.2. Background information about the preprocessing steps of the SAR images and the specific settings used in SNAP are discussed in Appendix B. After the data preparation phase, intensity, polarimetric and texture features are computed from the preprocessed products. The details on the extraction of features are explained in Section 4.3. In Section 4.4 the procedure is given on how the influence of sensor characteristics can be studied. Next, in Section 4.5 the classification approach is explained. Finally, the methodology for the evaluation of the classifiers is discussed in Section 4.6.

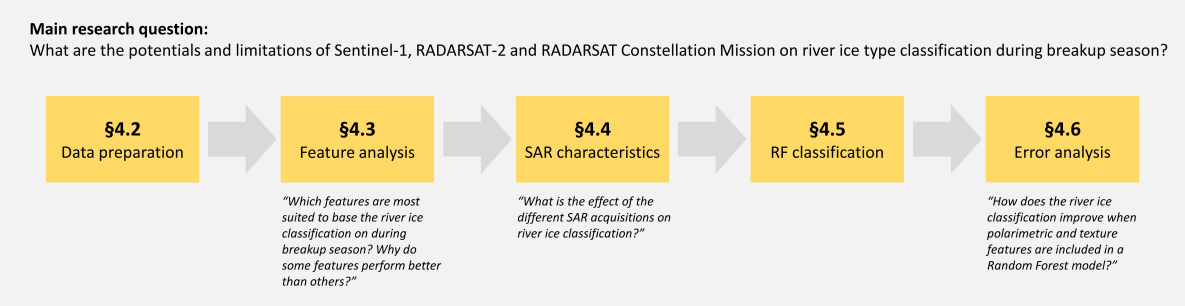

Figure 4.1: Schematic overview of the methodology of this thesis. The sub-questions are answered during different stages of the study. The main research question can be answered at the end of the research, when all phases are completed.

4.2. DATA PREPARATION

Figure 4.2 presents the flowchart of data preparation for this work. It consists of two main parts - data downloading and data preprocessing. The preprocessing chains are executed for all satellite missions.

4.2.1. DOWNLOADING

The *Sentinel-1* data set is accessible to any user via the Copernicus Open Access Hub, also known as the Sentinels Scientific Data Hub. An automatic data downloading script was developed, with three input parameters: the data product of interest (in this case: Sentinel-1 Level-1 SLC), a region of interest and a given time period of data collection. In this study, the Python tool *Sentinelsat* was used to batch download the data.

The *RADARSAT-2* data were sent to me personally, since the data is not publicly available. The *RADARSAT Constellation Mission* data were downloaded via the Earth Observation Data Management System (EODMS) website, which is a geospatial platform provided by NRCan to access Canadian remote sensing data. The general public can only download images with a spatial resolution up to 16 meter in GRD format.

SAR images from the three satellite missions have been downloaded for a time period between mid-March and end-May for breakup season 2018-2019 and 2019-2020. The Sentinel-1 IW images cover the entire region of interest. Most images of RADARSAT-2 and RCM have smaller swath widths and cover part of the studied river stretch. More information on the product details of the SAR images was provided in Tables 3.1, 3.2 and 3.3.

4.2.2. PREPROCESSING

For the data processing the ESA toolbox Sentinel Application Platform (SNAP) was used, which is a commonly used software for all Sentinel satellite toolboxes. Since version 5 (end-2016), SNAP also allows processing SAR images from RADARSAT-2. Preprocessing of RADARSAT Constellation Mission images is possible since version 8 (not released at the moment of writing). In this study, the beta release of SNAP 8 was used to preprocess the RCM images.

SNAP provides a powerful kit, named the graph processing tool (GPT), which is able to handle large data processing. Based on the GPT, automatic data preprocessing chains were developed for Sentinel-1, RADARSAT-2 and RCM. As the goal was to compare the preprocessed images, the processing chains are very similar. However, some small modifications were needed for each satellite mission to deal with the different product types. Sentinel-1 and RADARSAT-2 are preprocessed in SLC-format, from RCM only the GRD products could be used. Moreover, the differences in polarimetry ask for a slightly different preprocessing approach.

In the 'preprocessing'-box of Figure 4.2 three different preprocessing schemes are presented. The intensity scheme [A] was used for the extraction of intensity values. The output parameters of this preprocessing scheme are the intensity values for Sentinel-1 (VV and VH), RADARSAT-2 (HH, VV, HV and VH) and RCM (CH and CV). The polarimetric scheme [B] provides polarimetric output products, namely decomposition parameters and the covariance matrix. The texture scheme [C] provides information about the texture of the images. As was mentioned previously, the three preprocessing chains needed to be adjusted to each satellite mission, since the input data of the missions differed slightly. Some of the steps were only included for Sentinel-1 data. These steps are indicated with an asterisk symbol in Figure 4.2.

Figure 4.2: Data preparation plan for SAR data for the three different satellite missions. The data is downloaded from the Sentinel Scientific Data Hub (Sentinel-1) and EODMS (RADARSAT-2 and RCM). Three different processing schemes were executed for all satellite missions to obtain [A] intensity values, [B] decomposition parameters and the covariance matrix and [C] texture parameters. Preprocessing steps with an asterisk symbol are not executed for all SAR missions.

The different preprocessing schemes presented in Figure 4.2 show different steps. All the steps that were used are available in SNAP. The purpose of each step is explained below. The used methodology of the different steps can be found in Section 4.3.

- **Read data product:** The first step in SNAP is to read the specified file as product. SNAP is able to read data from multiple SAR sensors. Since version 8, also RCM data is recognized as readable SAR product and can be opened and processed. SNAP can read a .zip file that includes the SAR data (including metadata) or a manifest.safe file.
- **Apply orbit file:** The orbit state vectors provided in the metadata of a SAR product are generally not very accurate. The precise orbit files of satellites are determined after several days and can replace the inaccurate orbit state vectors. The operation of applying a precise orbit in SNAP provides an accurate satellite position and velocity information (Filipponi, 2019). In the latest SNAP version at the moment of this research (SNAP version 7 and beta version 8), the application of orbit files in SNAP is limited to Sentinel-1, ERS and ENVISAT, resulting in a less precise location of pixels for RADARSAT-2 and RCM images as this step could not be applied to these data products.
- **Calibration:** Calibration aims to convert the digital pixel values to radiometrically calibrated SAR backscatter, which is directly related to the radar backscatter of the scene. Two different output products were generated: the complex valued image and the gamma nought (γ^0) calibrated product. To construct the covariance and coherency matrices, the output product of calibration was chosen as a complex valued image. The gamma nought product was used to inspect individual polarizations, as it takes the looking angle of the sensor into account. Gamma nought gives a calibrated product, in which the reference area is positioned in the plane perpendicular to the local look direction, representing the local area that the radar system actually sees (Howell et al., 2019).
- **TOPSAR Deburst:** For each polarization channel, the Sentinel-1 IW product consists of three swaths. Each sub-swath image consists of a series of bursts, where each burst was processed as a separate SLC image. TOPSAR Deburst merges all these bursts and swaths into a single SLC image (Hu et al., 2018).
- **Multilooking:** To reduce the inherent speckled appearance of an original SAR image, several images are incoherently combined as if they corresponded to different looks of the same scene. As a result, the multilooked image improves the image interpretability. Additionally, multilooking is used to produce a product with nominal image pixel size.
- **Conventional Speckle filtering:** Speckles in SAR images degrade the quality of the image and make interpretation of features more difficult. Speckle noise reduction was applied by the spatial Gamma Map filter, with a window size of 3x3. More in-depth information about the selected speckle filter can be found in Appendix B.1.
- **Polarimetric Speckle filtering:** For full polarimetric SAR data (i.e. RADARSAT-2 quad-pol), SNAP offers polarimetric speckle filters that take advantage of all bands and preserve the complex information. Speckle reduction was conducted by using the SNAP-integrated refined Lee filter, with a window size of 7x7 (Plank et al., 2017). The Polarimetric Speckle filter has a second-order matrix as output (covariance or coherency matrix).
- **Decomposition:** The objective of polarimetric decompositions is to express the measured scattering matrix by the radar as a combination of the scattering responses of simpler objects. For example a small set of parameters to classify scattering mechanisms. SNAP offers multiple polarimetric decompositions for dual-pol, quad-pol and compact-pol data. In this study, only Sentinel-1 dual-pol and RADARSAT-2 quad-pol are decomposed, since only the GRD RCM data were available. However, it should be noted that the dual-pol decomposition methods are difficult to interpret physically. The input of the dual-pol decomposition is the speckle filtered coherency matrix T_2, for quad-pol the T_3 matrix was used. More information about the used SNAP configuration for decomposition parameter retrieval is discussed in Appendix B.2.
- **Normalize:** GLCM provides relative information. In order to compare the spatial information of SAR images, each image should first be normalized. This step is executed with the Data Conversion tool, in which the data can be linearly scaled. For each mission, the lowest and highest backscatter values were detected over the entire breakup season. These minimum and maximum values were used to specify the interval for normalization.

- **Texture analysis:** SNAP offers the widely used Grey Level Co-occurence Matrix (GLCM) tool to analyze the texture of the image. The GLCM is a measure of the probability of occurrence of two grey levels separated by a given distance in a given direction. The texture features can be categorized into three groups, namely contrast, orderliness and statistic group features (Haralick and Bryant, 1976). For this study, the statistic group features (GLCM mean, GLCM variance, GLCM correlation) were selected. The GLCM was computed based on the co-pol channels VV, HH and CH for Sentinel-1, RADARSAT-2 and RCM respectively. Appendix B.3 discusses the details on the used settings in SNAP to obtain texture features.
- **Range Doppler Terrain Correction:** Due to topographical variations of a scene and the tilt of the satellite sensor, distances can be distorted in SAR images. Terrain corrections were performed to compensate for these distortions so that the geometric representation of the image will be as close as possible to the real world. To accomplish this correction, the SRTM was used as the DEM to provide height information. The data were resampled to a 10 meter ground sampling distance by the nearest-neighbour interpolation (Hu et al., 2018).
- **Mask area of interest:** For further image analysis, it is useful to mask the area that is not of interest. SNAP allows to import a vector geometry. In this study a shapefile of the Athabasca River between 285 km and 445 km was imported. The mask operator turns any pixel that is outside the uploaded vector file into a no data value.
- **Data conversion:** SNAP is able to convert the linear dimensionless values to decibel (dB), which is more commonly used in remote sensing. For every pixel the log of the linear value is taken and this is multiplied by a factor of 10.
- **Write preprocessed data product:** The last step of every preprocessing scheme that was used for this research is to store the preprocessed data product to a specified file location. SNAP is able to write the preprocessed products in multiple formats. For this study NetCDF-4-CF was chosen.

In this last preprocessing step, different NetCDF raster files are created. For Sentinel-1 and RADARSAT-2 all three preprocessing chains presented in Figure 4.2 were performed to obtain intensity, polarimetric and texture parameters. For the RCM SAR images, only the intensity and texture chains were used. The following NetCDF files were written after preprocessing:

1. Gamma nought intensity features (output of preprocessing scheme *A*) - *Sentinel-1, RADARSAT-2, RCM*
2. Covariance matrices (output of preprocessing scheme *B*) - *Sentinel-1, RADARSAT-2*
3. Polarimetric decomposition parameters (output of preprocessing scheme *B*) - *Sentinel-1, RADARSAT-2*
4. Texture features (output of preprocessing scheme *C*) - *Sentinel-1, RADARSAT-2, RCM*

These raster products can be combined into one product using the *collocate* operator in SNAP. This tool allows to collocate spatially overlapping products. After preprocessing, the raster products already had the same spatial resolution. The collocation tool in SNAP requires a master product, slave products and an optional resampling method. For each SAR image, one of the co-pol intensity features (VV for Sentinel-1, HH for RADARSAT-2, CH for RCM) was selected as a master product. The other intensity features, the covariance matrix, the decomposition parameters and the texture parameters were set as slave products.

4.3. FEATURE ANALYSIS

After the data preparation phase, the intensity, polarimetric and texture features can be computed and analyzed in Python. Some of the preprocessed products are already features (e.g. intensity and texture features). Other features have to be computed first (e.g. intensity ratios and polarimetric features). The required equations were provided in Section 2.5.3.

In Section 4.3.1 an overview of the studied features per satellite mission is provided. Next, in Section 4.3.2, the method to temporally and spatially analyze the features is discussed.

4.3.1. EXTRACTION OF FEATURES

After the first phase of data preparation, the preprocessed data products were used to extract features that were used for the Random Forest classification. The features used in this research can be categorized into three classes, i.e. intensity, polarimetric and texture features. The first class is relatively simple to compute, since the prepocessed backscatter intensities are the output products of the first preprocessing schemes. The same holds for the texture features, which are the final products of the third preprocessing scheme. The polarimetric features are more complex, since they are computed based on the covariance matrix. The computation and physical interpretation of each feature was explained in Section 2.5.

Table 4.1: Overview of the extracted features per satellite mission. Intensity and texture features were computed for each satellite mission. Polarimetric features were computed for RADARSAT-2. For Sentinel-1 some pseudo-polarimetric features could be computed. No polarimetric features were computed for RCM, because only GRD data were available.

Features	**Sentinel-1**	**RADARSAT-2**	**RCM**
Co-pol intensity	VV	HH, VV	CH, CV
Cross-pol intensity	VH	HV, VH	-
Intensity ratio co-pol	-	$\frac{HH}{VV}$	$\frac{CH}{CV}$
Intensity ratio cross-pol	-	$\frac{HV}{VH}$	-
Intensity ratio cross-co-pol	$\frac{VH}{VV}$	$\frac{HV+VH}{HH+VV}$	-
Polarimetric phase difference co-pol	-	Φ_{HH-VV}	-
Polarimetric correlation coefficient co-pol	-	ρ_{HH-VV}	-
Polarimetric decomposition parameter I	Pseudo-Alpha	Alpha	-
Polarimetric decomposition parameter II	Pseudo-Anisotropy	Anisotropy	-
Polarimetric decomposition parameter III	Pseudo-Entropy	Entropy	-
T**exture parameter I**	GLCM mean	GLCM mean	GLCM mean
Texture parameter II	GLCM variance	GLCM variance	GLCM variance
Texture parameter III	GLCM correlation	GLCM correlation	GLCM correlation

4.3.2. TEMPORAL AND SPATIAL ANALYSIS

Temporal and spatial analysis aim to better understand the behaviour of river ice breakup. The method to create the temporal and spatial plots is explained in this section.

Temporal analysis enables to examine and model the behaviour of a parameter in a data set over time. In this study, the temporal courses of the intensity, texture and polarimetric features were studied. The mean and standard deviation of the features were plotted over time in the temporal analysis figures. In remote sensing, dimensionless features like intensity are normally expressed in decibel (dB), which is computed by

$$z = 10 * \log_{10}(y) \tag{4.1}$$

in which y is the dimensionless backscatter and z the backscatter in log-scale. To represent the error bars correctly, a differential analysis can be used, with

$$\delta z \approx dz = d[10 * \log_{10}(y)] = \frac{10}{\ln(10)} * \frac{dy}{y} \approx 4.343 \frac{\delta y}{y} \tag{4.2}$$

in which δz is known as the relative error, 4.2 δy is the standard deviation of the backscatter in a certain segment and y represents the average value of the backscatter in linear-scale. To plot the range of the standard deviation of the backscatter intensity, $\pm 4.343\ \delta y/y$ has to be added or subtracted from the average segment intensity.

The results, presented in Chapter 5, show two types of *spatial* plots, namely 1D and 2D figures. In the 1D images, the behaviour of a feature over the stretch of the river was studied. In the 2D images, the spatial patterns over the river width can also be analyzed.

In the 1D plots, the distance along the Athabasca River is plotted on the x-axis and a certain parameter is presented on the y-axis. In these figures for every kilometer along the Athabasca River the median value of the studied parameters for each kilometer section was plotted, see Figure 4.3. The first step in obtaining this median value is to create a centerline of the river. This centerline can be created in QGIS with the *HCMGIS* plugin, which creates centerlines for roads, rivers and similar linear structures. However, in this study, a centerline of the Athabasca River with a vector point at each kilometer was provided by Alberta Environment & Parks.

To find the mean or median value of each km-section, the *nearest neighbour* operator was used in SNAP, which finds the closest km-point for each pixel. In this study, a stretch of 160 kilometers was studied, ranging from km 285 to km 445.

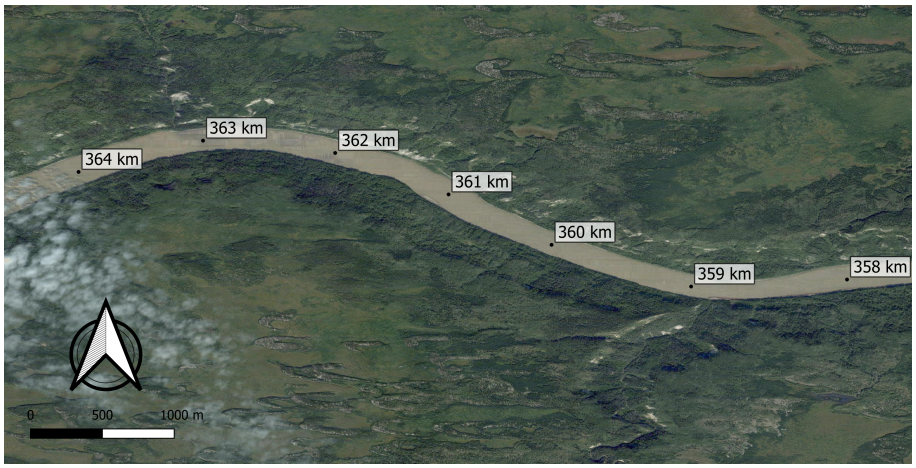

Figure 4.3: Vector points for each kilometer along the Athabasca River. For the spatial analysis of SAR features, median values were computed from km 285 to km 445. The centerline and km-points were provided by Alberta Environment & Parks.

4.4. SAR CHARACTERISTICS

SAR characteristics influence the returned radar signal. To answer the second sub-question of this research, the influence of four SAR properties was analyzed, namely polarization channels, incidence angle, acquisition time and noise floor.

When a SAR image is imported in SNAP, the metadata can be explored. The metadata provides basic product information such as acquisition date, product type and acquisition mode. After importing the sample areas in SNAP using the *ESRI shapefile* import option, the metadata of that specific area can be downloaded. This can be done by selecting the *Export mask pixels* operator. In Python the mean values of the incidence angle and acquisition time were computed and plotted against the average co-pol backscatter of the sample areas to analyze the influence of SAR characteristics.

4.5. RANDOM FOREST CLASSIFICATION

After the extraction of intensity, polarimetric and texture features, several Random Forest classifications were performed. The Random Forest algorithm is based on decision tree classification (Breiman, 2001), and has been applied successfully in ice classification (e.g. Boulze et al., 2020, Hoekstra et al., 2020). Before the actual classification can be executed, several preparation steps have to be conducted. First of all, sample areas should be selected (see Section 4.5.1) and divided into a training and validation data set (see Section 4.5.2). Next, in Section 4.5.3 the method to optimize specific RF parameters is discussed. Finally, in Section 4.5.4 a data-based approach is explained which identifies the most relevant features.

4.5.1. SELECTION OF SAMPLE AREAS

Sample areas were selected from which the ice stage was known based on reference data. An ice stage was assumed to be known when the acquisition time of reference data almost matched the SAR acquisition time or if the ice stage could be confirmed by AEP.

Sample areas were selected for each satellite mission. Ten Sentinel-1 SAR images, eight RADARSAT-2 images and fifteen RCM images were used for this selection. The sample areas were selected over the entire study region in such a way that there was no overlap between the samples, see Figure 4.4.

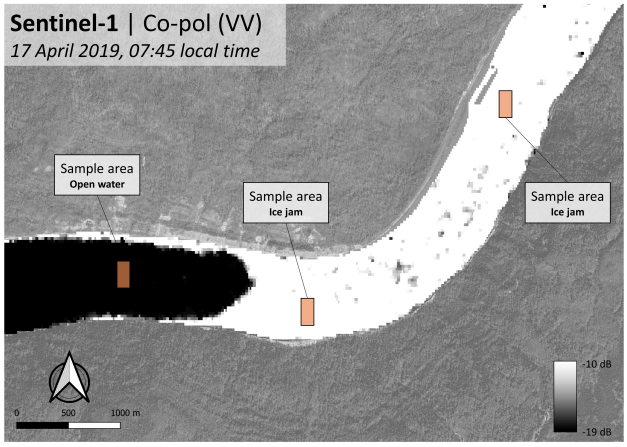

Figure 4.4: Methodology to select sample areas in QGIS. Based on reference data, sample areas were selected manually. Polygons of 100 pixels were drawn over areas with a homogeneous backscatter. The presented river stretch shows a part of an ice jam imaged by Sentinel-1 at 17 April 2019.

In QGIS the features were drawn by using the *QAD Plugin*. This plugin gives the possibility to manually draw areas with a specific amount of pixels. For each satellite mission seventy sample areas were created for each ice stage, all of which consisted of a hundred pixels. It should be noted that there were fewer images available with open water and ice jams, so these sample areas could only be selected from a limited amount of SAR images for each mission.

4.5.2. TRAINING AND VALIDATION SETS

To train and validate the Random Forest classifier, 70% of the sample areas were used for training and 30% for validation, see Figure 4.5. The training data is used to fit the RF-model. To check how well the model is able to predict on unseen data, the model is run against the test data. The predicted and expected results are used to study the model performances.

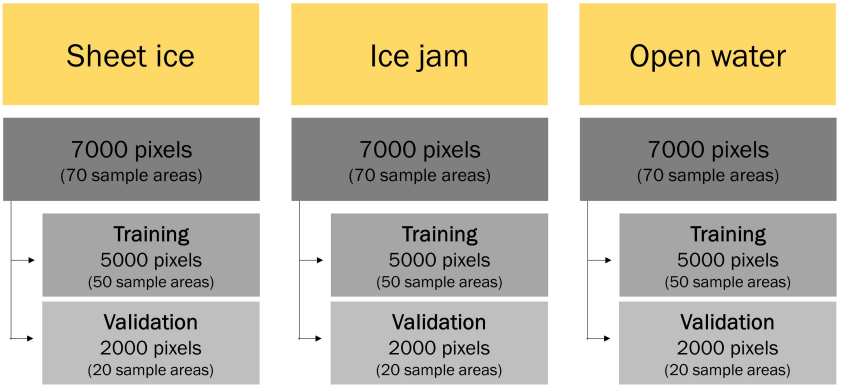

Figure 4.5: Splitting the sample area data set in training and validation data. The splits were made on sample area level, so pixels in one area were kept together. This train-test split approach was used for each satellite mission.

An overview of all the acquisition dates of the sample areas and the division between training and validation data is shown in Figure 4.6. Sheet ice sample pixels were acquired over the entire breakup season. There were fewer SAR scenes with ice jams and open water, so these sample areas were selected from a limited number of SAR images.

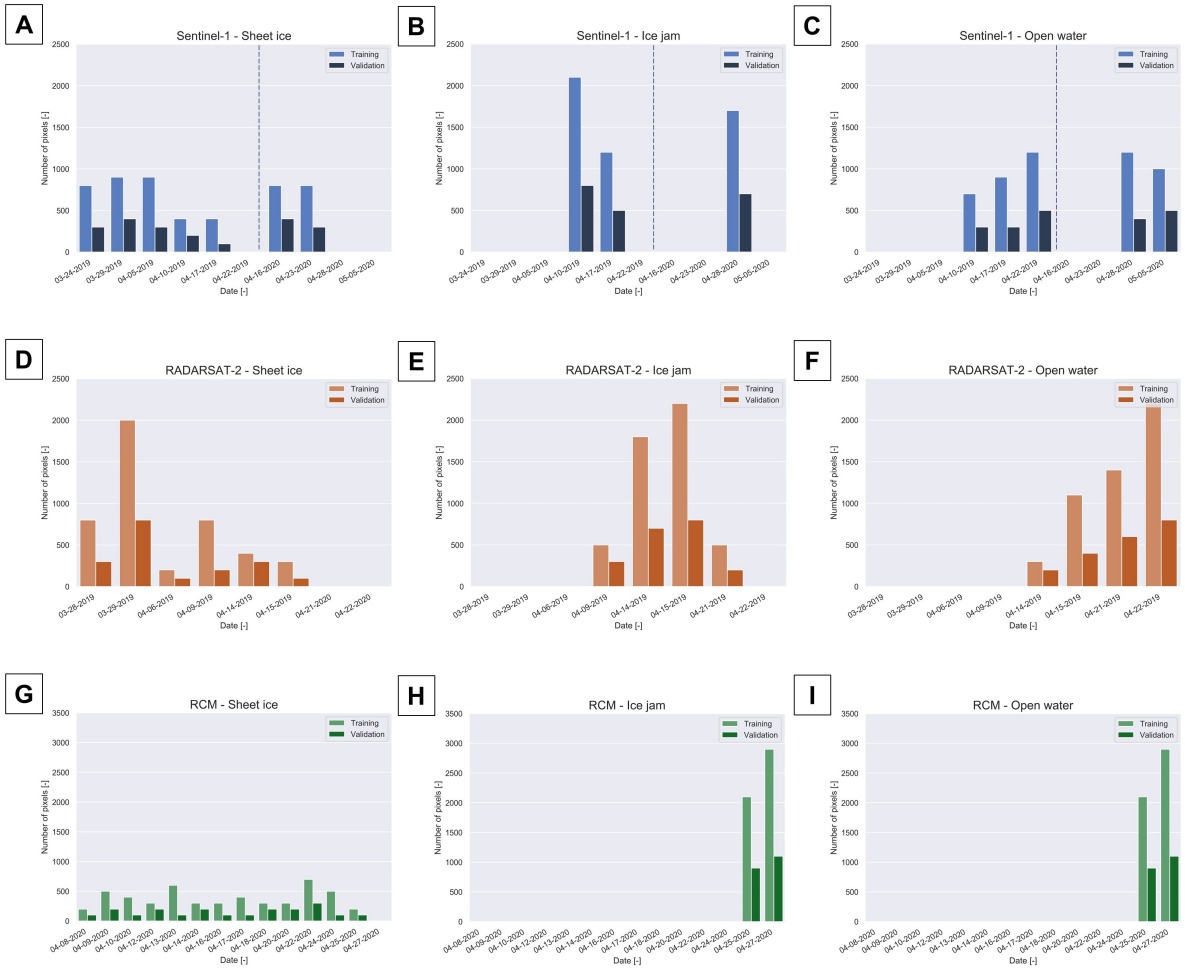

Figure 4.6: Overview of sample areas used in this study. Sample areas were divided into two groups: 70% training data, 30% validation data. [A], [B] and [C] show the sample areas for Sentinel-1 (2019 and 2020), [D], [E] and [F] for RADARSAT-2 (2019), [G], [H] and [I] for RCM (2020).

4.5.3. OPTIMIZATION OF HYPERPARAMETERS

Optimizing hyperparameters is a key step in making accurate predictions with Random Forest models. Hyperparameters are parameters of the model that are set before the start of the learning process. By adjusting these parameters, the performance of the Random Forest model can be optimized. Four parameters were analyzed in this research: *n_estimators*, *max_depth*, *min_samples_split* and *min_samples_leaf*.

The first parameter *n_estimators* specifies the number of trees in the Random Forest model. The default number is ten, which means that ten different decision trees will be constructed. The second parameter *max_depth* defines the maximum number of levels in each decision tree. The default value is None, which indicates that each tree will expand until each leaf only has data from the same class. The *min_samples_split* describes the number of samples required to split an internal leaf node. The default value is two, meaning that an internal node must have at least two samples in order to split. The final hyperparameter that can be tuned is the *min_samples_leaf*. This parameter specifies the minimum number of data points allowed in a leaf node. The default value is one, which means that every leaf must have at least one sample that it classifies. However, default values of hyperparameters do not always result in the optimal classifier.

The adjustment of the hyperparameters is performed on the training data. Once the parameters are opti-

mized, the Random Forest model is tested on the validation data set. A good approach to find the optimized hyperparameters is to plot validation curves. A validation curve can be plotted on a graph to analyse the influence of a single hyperparameter on the training score and the validation score. In this way, one can find out whether the RF-model is overfitting or underfitting for some hyperparameter values. The validation curves and appropriate hyperparameter values for this study are presented in Appendix D.

The *sklearn* package in Python includes the *validation_curve* function. This function was used to generate parameters that are required to plot such a validation curve. The training set including features and labels and the name and range of one of the four hyperparameters are required as input for the *validation_curve* function. The output of the *validation_curve* function contains the training and test scores for varying hyperparameter values.

4.5.4. SELECTION OF FEATURES

As the number of features increases in a Random Forest model, the model becomes more complex. In practice, not every feature in a data set carries information useful for discriminating ice stages. Some features are either redundant or irrelevant and hence can be removed. By only selecting the important features, several benefits are gained. First of all, the model becomes more simple to interpret. Secondly, feature selection is a powerful defence against overfitting, because less redundant data means a lower chance to make decisions based on noise. Finally, the computational costs and time required to train the model are reduced. The process of identifying only the most relevant features is called "feature selection".

A popular approach for feature selection is the Recursive Feature Elimination (RFE) technique (Guyon et al., 2002). RFE is basically a backward selection of features. The first step of this technique is building a RF model on the entire set of features and computing the importance of each feature. The least important features are removed. Then the Random Forest model is re-built and importance scores are computed again (Kuhn and Johnson, 2019).

The main issue of RFE is that it can be expensive to run. In order to reduce the computational cost, correlated features can be removed beforehand. It is better to do this anyway, because highly correlated features provide the same information. The correlation between each feature can be found by computing the correlation matrix. Pandas *dataframe.corr()* can be used to find the pairwise correlation of all features. To visualize the computed correlation coefficients, a heatmap can be created. For this study, from parameter pairs with a correlation higher than 0.85 or lower than -0.85, the least representative feature was removed.

The next step is to run the Recursive Feature Elimination. The *scikit*-learn Python machine learning library provides an implementation of RFE. RFE requires a specified number of features to keep, however it is often not known in advance how many features are valid. Cross-validation can be used to find the optimal number of features. The idea of cross-validation is to use the initial training data to generate multiple training-test splits. Standard k-fold cross-validation can be used, in which the data is partitioned into k subsets, also known as folds. By using this approach, the validation data is a truly unseen data set for testing the final model (Cawley and Talbot, 2010).

When running the RFE algorithm in Python, several variables need to be set. First of all, *X*, that represents all the training features, and *target*, that represents the target variable, are used as input for the RFE algorithm. Secondly, the *machine algorithm* has to be selected, in this study, Random Forest was selected. *Step* is the number of features to remove at each iteration, which was set to one. Also, the *cross-validation* approach should be chosen, this was set to StratifiedKFold with k equals 10. Finally, a *scoring metric* can be selected. In this study 'accuracy' was used.

When using RFE, it is interesting to know which features were selected and which were removed. By using the RFE attribute *feature_importance* the added value of each feature becomes clear. This RFE attribute reports the relative ranking of features in the same order.

4.6. ERROR ANALYSIS

This study examined three commonly used evaluation indices, namely the *confusion matrix, overall accuracy* and *Cohen's Kappa* coefficient. Other popular metrics such as *F1-score* and *precision-recall ratio* are not used, since these are more relevant for unbalanced data sets.

A *confusion matrix* is a way to express how many of the RF predictions were correct, and when incorrect,

where the classifier got confused. The diagonal values of the matrix are true positive counts, while off-diagonal values are false positive and false negative counts, for each class against the other. The *overall accuracy* characterizes the overall efficiency of the RF classifiers and is determined by dividing the total number of correctly identified pixels by the total number of validation pixels. The *Cohen's Kappa* statistic is a metric that compares an observed accuracy with an expected accuracy or random chance. Hence, this value indicates how much better the performance of a classifier is, compared to guessing with the target distribution (Yang et al., 2018).

Scikit-Learn's *confusion_matrix* takes the true validation labels and the actual predictions and returns the confusion matrix as an array. *Seaborn heatmap* was used to add labels and a color scale, which visualizes data better than a table of numbers. The overall accuracy and Cohen's Kappa metrics were computed with the following two functions: *sklearn.metrics.overall_accuracy* and *sklearn.metrics.cohen_kappa_score*. The validation features and labels are used as input for these functions.

To examine whether the 'IntPolTex' classifier makes *significantly* better predictions than the 'Int' classifier, *hypothesis testing* is used. Cohen's kappa statistics were computed based on the confusion matrices of each classifier, by using the Python function *statsmodels.stats.inter_rater*. The output of this function, the kappa statistic $\hat{K}$ and kappa variance σ^2 were used to construct a hypothesis test for significant difference between 'Int' and 'IntPolTex' classifiers. The test statistic $\Delta\hat{K}$ is given by

$$\Delta\hat{K} = \frac{|\,\hat{K}_{Int} - \hat{K}_{IntPolTex}\,|}{\sqrt{\sigma^2_{Int} + \sigma^2_{IntPolTex}}} \tag{4.3}$$

where $\hat{K}$ is the kappa statistic and σ^2 its corresponding variance (Bishop et al., 2007, Congalton et al., 1983) of the 'Int' and 'IntPolTex' classifiers. Two classifiers may be considered significantly different when $\Delta\hat{K} > 1.96$, when a confidence level of 95% is used (Benson and DeGloria, 1985).

In this study, hypothesis testing was not performed to examine significant differences between Sentinel-1, RADARSAT-2 and RCM. Different sample areas were used for each mission, which complicates the comparison between the three satellite missions.

5

RESULTS

In this chapter, the main results are shown which are relevant to the research questions. First of all, a study on the temporal and spatial variations of the studied breakup seasons is presented. This gives a more in-depth understanding of the river ice development over the breakup season and its influence on the radar backscatter. Second, to analyze the effect of different polarizations on river ice classification, the impact of variables differing per SAR acquisition is quantified. Next, the classification potential of different features is discussed per satellite mission. Finally, the results of the Random Forest classifications are presented and the quality of each classification is discussed. Besides the accuracy results, classification maps are presented that give a better understanding of the potentials and limitations of each classifier.

5.1. TEMPORAL AND SPATIAL ANALYSIS OF RIVER ICE BREAKUP

After following the preprocessing steps as were described in Section 4.2, spatial plots of the SAR images were created to analyze the breakup patterns of the 2018-2019 and 2019-2020 breakup seasons. In this research, Sentinel-1 and RADARSAT-2 SAR images were used to study the 2018-2019 breakup. For the 2019-2020 breakup, preprocessed Sentinel-1 and RCM images were used.

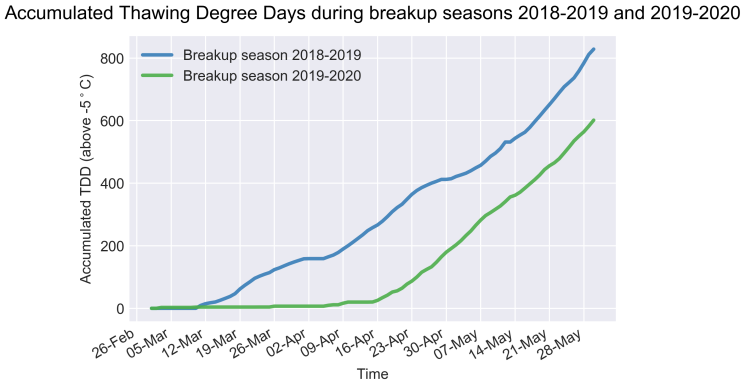

Figure 5.1: Accumulated Thawing Degree Days obtained from weather station 3062696, located 10km southeast of Fort McMurray. Mean daily temperatures above -5°were observed one month later in breakup season 2019-2020 (mid-April) compared to 2018-2019 (mid-March).

In general, the breakup of an ice cover is triggered by a sudden increase of runoff caused by a combination of precipitation and increasing temperatures. Figure 5.1 shows the Accumulated Thawing Degree Days (ATDD) of the breakup seasons 2018-2019 and 2019-2020, which helps to understand the breakup patterns of the two different years. The ATDD can be interpreted as a time-temperature integral that represents the cumulative warming over the spring season (Bilello, 1980).

The ATDD were calculated based on the mean daily temperature that was measured by weather station

3062696, which is located at the airport of Fort McMurray, 10 km southeast of the city. A base of -5°C was used, since the majority of river ice covers already exhibit 10% or more thinning before the temperature exceeds 0°C (Lotsari et al., 2019). The mean temperatures were summed over a period of three months, from 1 March to 1 May.

The observed ATDD of the breakup seasons 2018-2019 and 2019-2020 show similar patterns. However, there is a time difference of one month between the two breakup seasons. In the 2018-2019 breakup season, a significant rise in temperate is visible from mid-March on. A year later, during the breakup season of 2019-2020, this increase in temperature started around mid-April. From the SAR images and reference data, this temporal difference is also visible. A decrease in SAR backscatter in parts of the Athabasca River can be observed in mid-March in 2019 and mid-April in 2020.

Besides temperature data, a second source that might help to interpret the SAR backscatter are Snow Water Equivalent (SWE) records. Since 2008 a climate station, located around 50 km southeast of Fort McMurray, measures the depth of water contained within the snowpack of the Gordon Lake. The records provide information on SWE accumulation and ablation. Figure 5.2 shows the daily amount of water that was melted in the snow for the breakup period of 2018-2019 and 2019-2020. Even though there is no SWE measurement device on the Athabasca River, the snowpack on the Gordon Lake station is expected to behave almost similar, since meteorological circumstances are comparable.

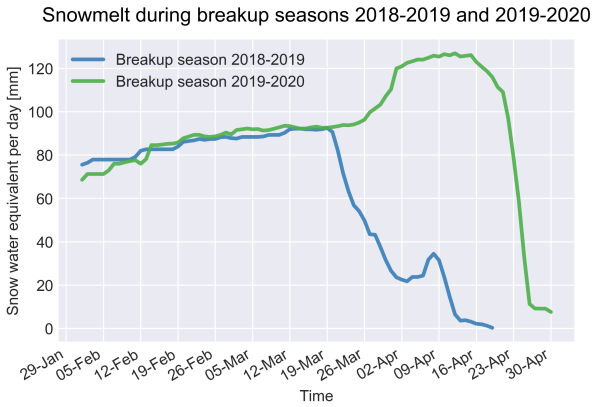

Figure 5.2: Measured accumulation and ablation of snow water equivalent at Gordon Lake snow pillow.

Figure 5.2 shows the measured accumulation and ablation of SWE at Gordon Lake snow pillow for the breakup season 2018-2019 and 2019-2020. For the first year that was studied, the largest decrease of the snow layer took place from mid- till end-March, comparable to the time period when the mean daily rapidly increased. Around 8 April a small peak shows up, this can be linked to a snowfall event that took place on 4 April. For breakup season 2019-2020 the largest part of the snow layer melted between mid-April and end-April, which also coincides with the temperature increase presented by Figure 5.1.

A dry snow layer increases the SAR backscatter, due to both surface and volume scatter of the radar signal. On the other hand, when the SWE decreases, the ice layer is covered by a wet layer. This will lead to lower backscatter values, due to specular surface reflection and hampered volume scattering. Therefore, a high SAR signal is expected before mid-March for the 2018-2019 season and before mid-April for the 2019-2020 breakup. Also, a sudden increase is expected to be visible in SAR images after the snowfall event of 4 April 2019.

5.1.1. BREAKUP SEASON 2018-2019

Figures 5.3 and 5.4 show the VV (Sentinel-1) and HH (RADARSAT-2) backscatter patterns over the Athabasca River between 12 March 2019 and 22 April 2019. After the preprocessing of the SAR images, the median backscatter per kilometer of the Athabasca River was plotted.

The images acquired at 12 March 2019 in Figures 5.3 and 5.4 show a high backscatter, which is in accordance with the expectations based on the ATDD plotted in Figure 5.1 and the SWE plotted in Figure 5.2, where it can be seen that thawing had not started before mid-March. Hence, the river ice is still in winter conditions,

where the dry ice cover enhances the radar signal to penetrate the ice layer, resulting in a high backscatter due to volume scattering. Also, the rough surface might lead to some diffuse scattering.

In the spatial plots obtained between mid-March and end-March 2019 in Figures 5.3 and 5.4, the backscatter starts to decrease. The first stretch of the river where ice and snow start to melt is in the downstream stretch, between 285 km - 330 km. This is in accordance with the reference data, as were described in Section 3.1.1. At the end of March, a low backscatter is measured for the entire river stretch. Sentinel-2 images from this period (26 and 31 March 2019) show that there is melt water on top op of the ice cover at several locations. The Sentinel-2 image of 31 March also shows some small cracks.

Sentinel-1 and RADARSAT-2 images from 5 April 2019 show an increase in backscatter. An explanation is the snowfall event of the previous day, which was also visible in Figure 5.2. A week later around 13 April, all snow has melted. Already large parts of the river are free of snow and ice from 9 April on, which was also reported in Section 3.1.1. The part upstream of Crooked Rapids (km 335) is open water from this date on. The river stretch downstream of Fort McMurray (km 290) is open after April 14.

According to the observation flights of AEP, an ice jam was located between km 307 and km 322 at 14 April 2019. This ice jam remained at the same location, but slowly melted off at the head of the ice jam. At 19 April 2019 the ice jam was observed between km 307 and km 311 and was released later that day. This 15 km long ice jam can be observed in the Sentinel-1 image of 17 April and the RADARSAT-2 images of 14 and 15 April. At 21 April 2019, another small ice jam was observed at the city of Fort McMurray, between km 293 km and km 296. However, this ice jam is difficult to see in the SAR images.

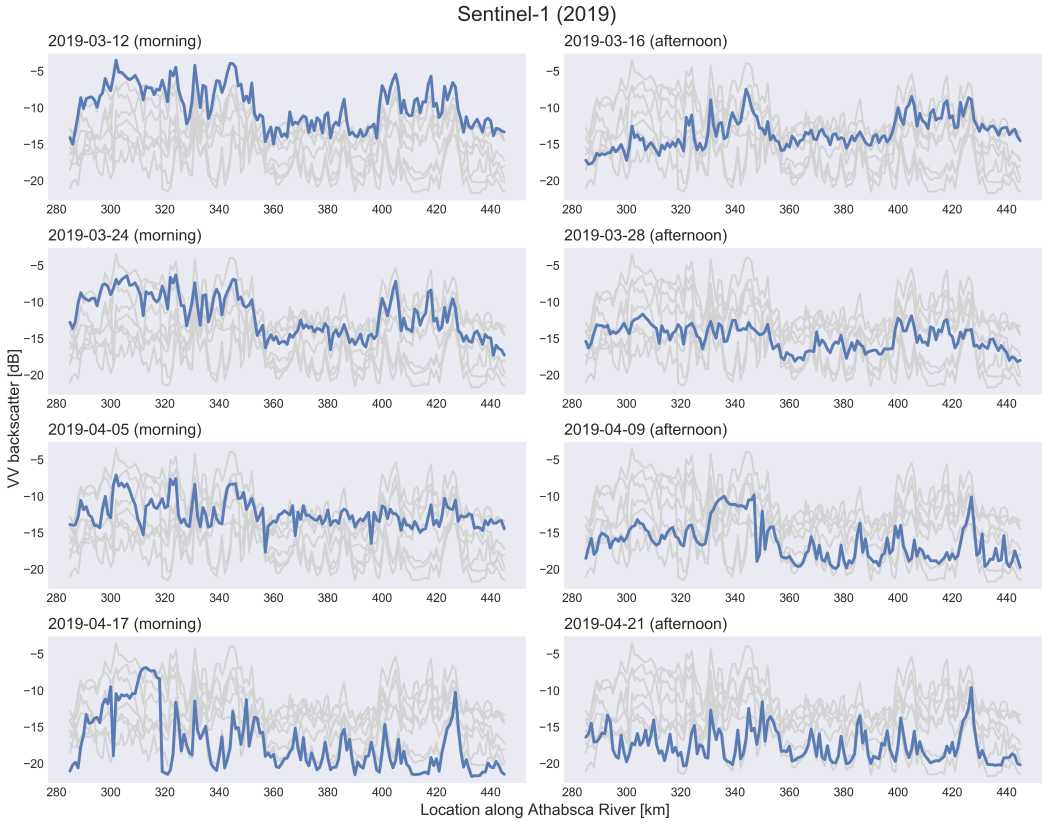

Figure 5.3: VV backscatter acquired by Sentinel-1 over the Athabasca River during breakup season 2018-2019. From mid-March on, ice degradation starts at the downstream part of the stretch. The ice jam from 17 April is clearly visible in the SAR image, represented by a high VV backscatter. To ease the comparison, each figure shows the backscatter values of all days (in grey), with a specific day highlighted (in blue).

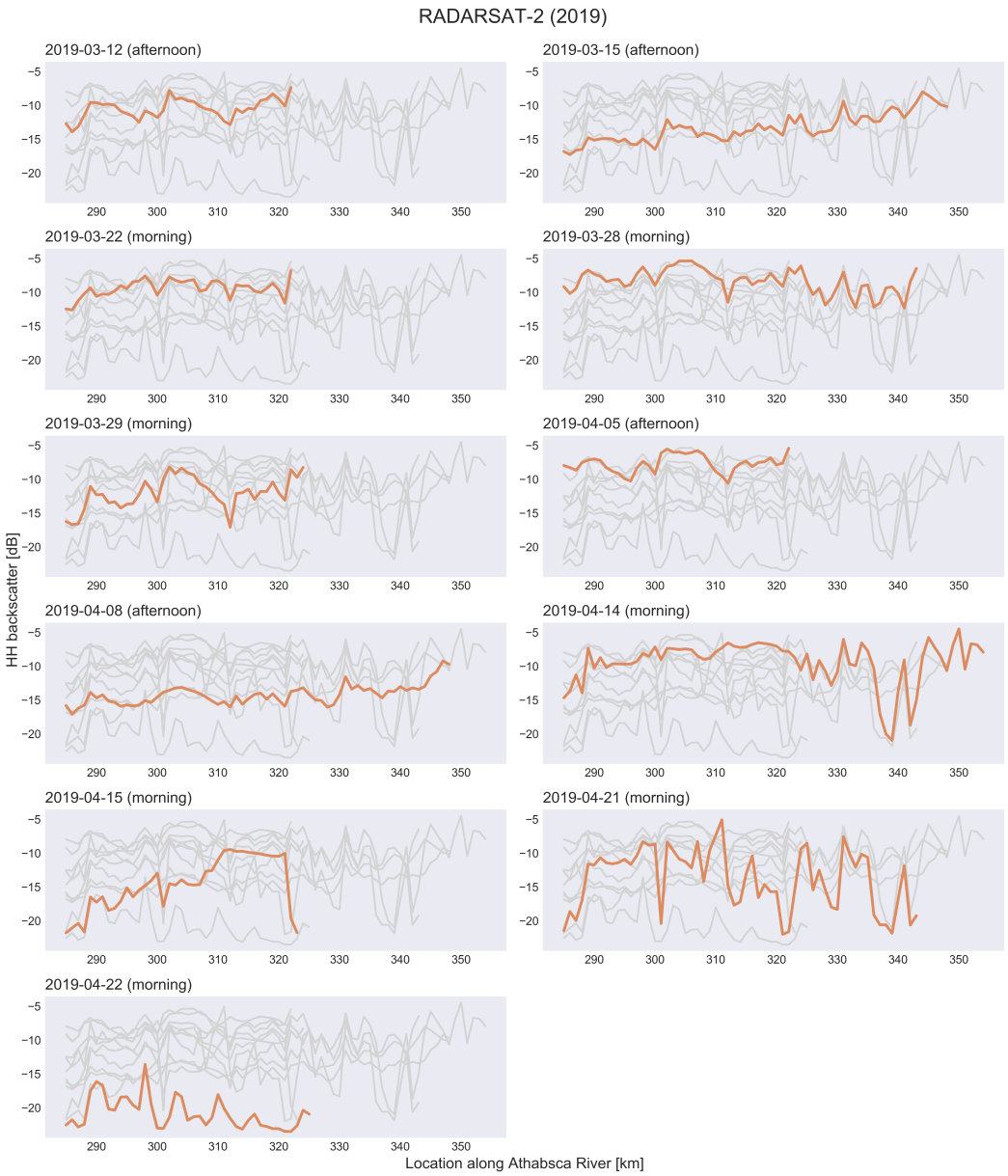

Figure 5.4: HH backscatter acquired by RADARSAT-2 over the Athabasca River during breakup season 2018-2019. Only the downstream part of the stretch is observed by RADARSAT-2. An ice jam was present on multiple SAR images, namely at 14, 15 and 21 April. The largest part of the river was free of ice in the last SAR image obtained at 22 April. To ease the comparison, each figure shows the backscatter values of all days (in grey), with a specific day highlighted (in blue).

5.1.2. BREAKUP SEASON 2019-2020

Figures 5.5, 5.6 and 5.7 show the VV (Sentinel-1) and CH (RCM) backscatter over the Athabasca River between 18 March 2020 and 5 May 2020. Figure 5.1 indicates that the breakup season of 2019-2020 started one month later than in the breakup season of the previous year, which was also indicated by the Accumulated Thawing Degree Days in Figure 5.1. According to 3.1.2, thermal deterioration of the ice cover started from mid-April 2020 onwards. This is also visible in the SAR images. The backscatter of Sentinel-1 starts to decrease from 15 April 2020 onwards. For RCM, the first image that shows this drop in backscatter was acquired on April 18. From this moment on, the SWE also clearly starts to drop (Figure 5.2).

From 23 April 2020 on, a large part of the Athabasca River is open again (upstream of 330 km), which was both reported by AEP and is visible in the SAR images, for example in the RCM image of 24 April 2020 (afternoon) and in the Sentinel-1 image of 23 April 2020. However, not the entire stretch is open yet. At April 24, AEP reported a 21 km long ice jam located between km 308 and km 329. The next day, this ice jam was partly released. Nevertheless, the head of the ice had grown in upstream direction, resulting in an ice jam between km 325 and km 345. The ice jam was released at 26 April and formed a new ice jam downstream, at the city of McMurray between 285 and 305 km. For four days, until 30 April 2020, this ice jam stayed at this location at the city of Fort McMurray, which resulted in enormous floodings. The ice jam is clearly visible in the SAR images of 27 April 2020 from both Sentinel-1 and RCM. The SAR backscatter for both missions reached values around -9 dB. After 30 April 2020, the entire river stretch was open again.

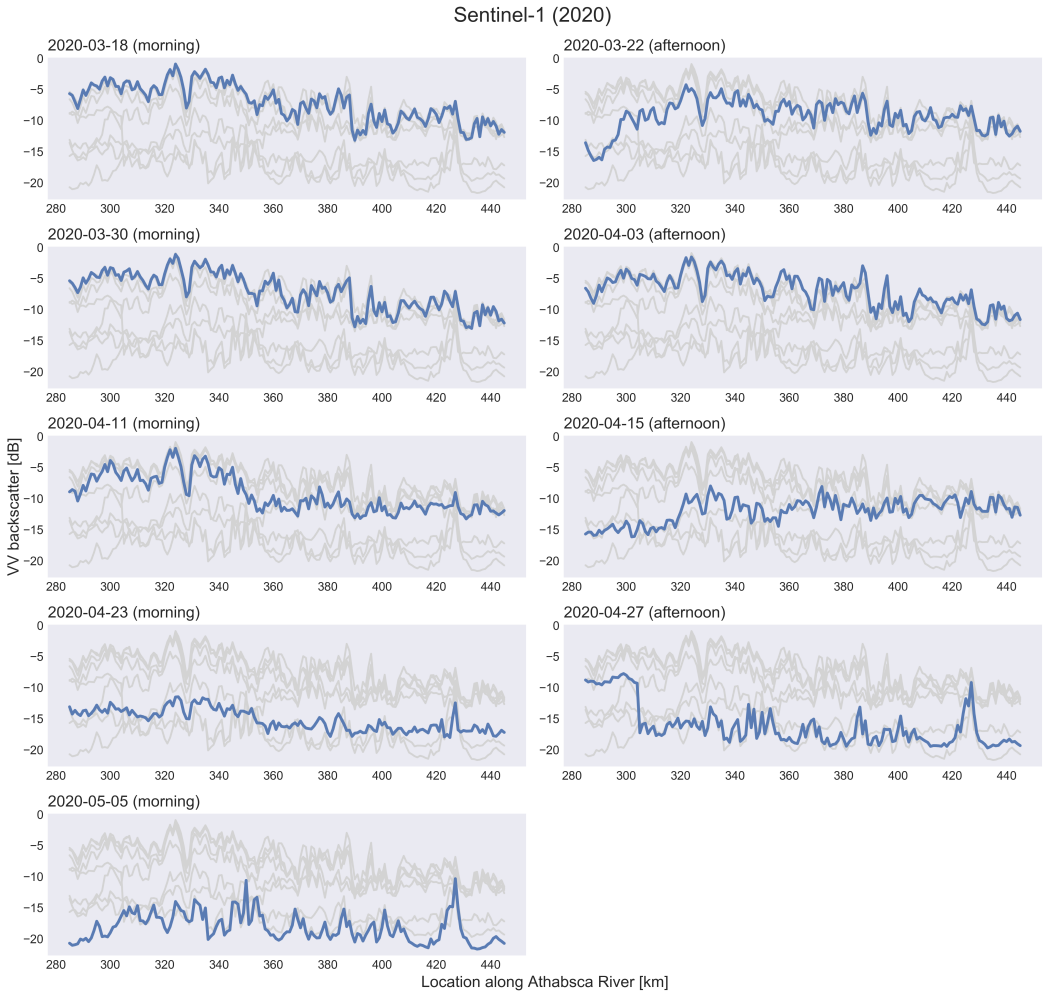

Figure 5.5: VV backscatter acquired by Sentinel-1 over the Athabasca River during breakup season 2019-2020. The first decrease in backscatter can be found in the upstream part of the river. The large ice jam that caused the Fort McMurray flooding is clearly visible in the SAR image of 27 April. To ease the comparison, each figure shows the backscatter values of all days (in grey), with a specific day highlighted (in blue).

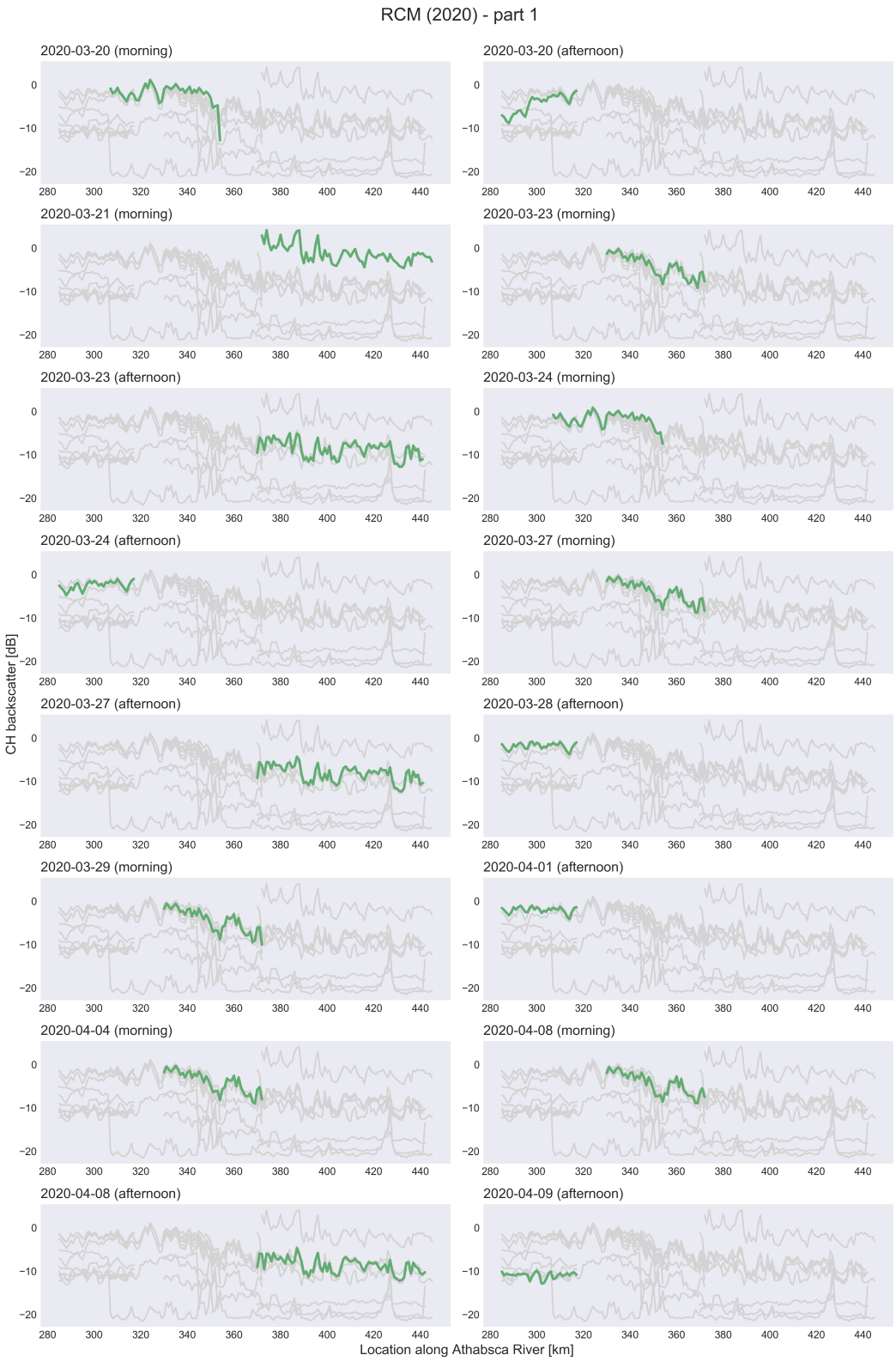

Figure 5.6: CH backscatter acquired by RCM over the Athabasca River during breakup season 2019-2020 (part 1). The upstream part of the river stretch shows the first signs of ice degradation. At the beginning of April, snow and ice melt were present on most parts of the river. To ease the comparison, each figure shows the backscatter values of all days (in grey), with a specific day highlighted (in blue).

Figure 5.7: CH backscatter acquired by RCM over the Athabasca River during breakup season 2019-2020 (part 2). The second half of the breakup season starts with further decay of the ice cover. The last image, acquired at 27 April 2020, shows the large ice jam that resulted in severe flooding.

5.2. EFFECT OF SAR CHARACTERISTICS ON BACKSCATTER

Before comparing the feature values of sample areas that were used to train and validate RF classifiers, it is important to understand the effect of different SAR characteristics on the radar backscatter. In this study, four variables were studied: polarization channels, acquisition time, incidence angle and noise floor.

5.2.1. POLARIZATION CHANNELS

For simplification, in this report the polarization channels were divided into two groups, which were labeled as *co-pol* channels (Sentinel-1: VV, RADARSAT-2: HH and VV, RCM: CH and CV) and *cross-pol* channels (Sentinel-1: VH, RADARSAT-2: HV and VH). Please note that CH and CV are not actual co-pol channels.

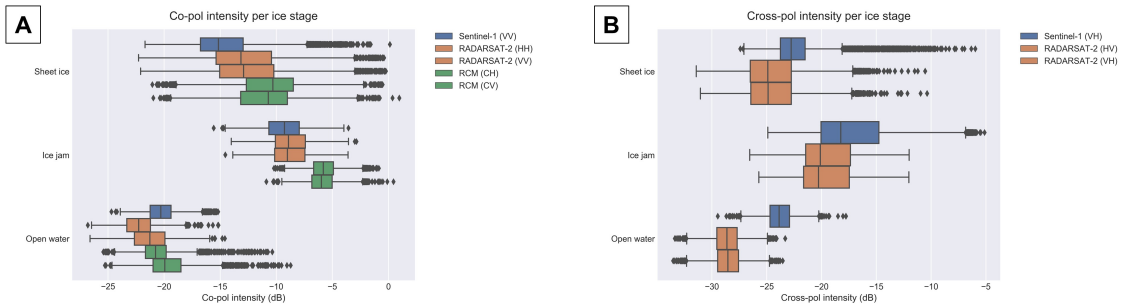

Figure 5.8: Backscattering values of co-polarization and cross-polarization channels for the different ice stages.

Figure 5.8 [A] shows a boxplot of the co-pol backscatter for all analyzed polarization channels. Open water shows the lowest average backscatter for all co-pol channels (between -22 dB and -20 dB). As expected, the smooth surface results in specular reflection away from the sensor, resulting in low backscatter values. Conversely, ice jams give the highest average backscatter (between -9 dB and -6 dB). The rough surface and, when the surface is dry, the ability for penetration leads to diffuse surface scattering and volume scattering. Sheet ice shows the largest range of received backscatter. The large variability of sheet ice (e.g. winter conditions, wet snow on top of ice layer, melting conditions) leads to this wide spread and makes it difficult to distinguish sheet ice from the two other ice stages, based on co-pol intensity alone.

Figure 5.8 [B] shows the cross-pol backscatter. Please note that RCM does not have cross-pol channels, so only Sentinel-1 and RADARSAT-2 were analyzed. Similar patterns as in Figure 5.8 can be observed. However, cross-pol channels give a relatively lower backscatter for sheet ice. For this study, mainly sheet ice under melting conditions was observed. Even a thin layer of water on the ice cover, dramatically reduces depolarization, and thus the cross-pol backscatter. This can be explained by the smooth surface, resulting in specular surface scattering. Moreover, the wet surface leads to minimal penetration of the radar signal, resulting in very limited volume scattering.

From Figure 5.8 [A] and [B] it can be concluded that both co-pol and cross-pol channels from different satellite missions are comparable. Likewise polarizations from the same satellite mission (i.e. HH and VV - RADARSAT-2, HV and VH - RADARSAT-2, CH and CV RCM) have a correlation coefficient close to 1 (more about this in Section 5.3), and thus not provide added value when solely looking at backscatter.

5.2.2. ACQUISITION TIME

Figure 5.9 show the influence of the overpass time on the co-pol backscatter of Sentinel-1 (VV), RADARSAT-2 (HH) and RCM (CH). For all three satellite missions, an increase of 1 to 2 dB is visible when comparing the sheet ice and ice jam afternoon with morning overpasses. In the hours before the acquisition of the afternoon images, for most days there have been hours of solar radiation and temperatures above 0°, resulting in melt water and hence a decrease in backscatter. During the night, the temperatures start to lower and parts of the melt water might refreeze, resulting in a higher backscatter for the morning overpasses. This effect is not visible for open water, since sample areas were only labeled as open water as the area was completely open. Hence, the open water class will not be influenced by the acquisition time, but by other factors, like the influence of wind speed and wind direction.

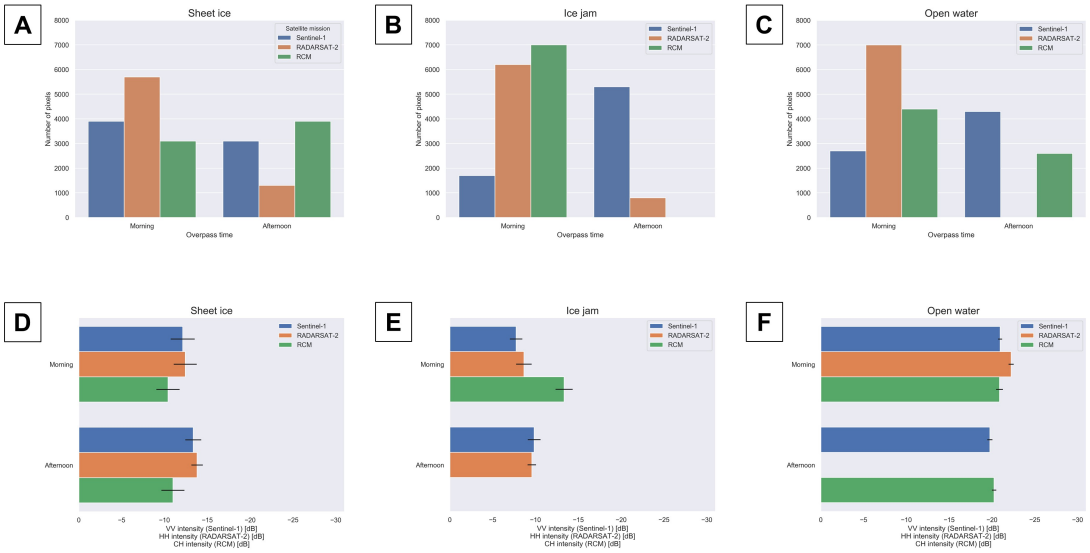

Figure 5.9: Influence of overpass time on SAR backscatter. [A],[B] and [C] show the ratio between sample areas that were acquired in the morning and the afternoon. [D], [E] and [F] show the average backscatter for the morning and afternoon overpasses per ice stage. Sheet ice and ice jams have a lower average backscatter in the afternoon overpasses.

5.2.3. INCIDENCE ANGLE

Another influencing SAR characteristic, that differs per SAR image and even within SAR acquisitions, is the incidence angle. Even though the calibrated gamma nought product was used, which minimizes the effect of the incidence angle, the influence of the incidence angle is clearly visible. Again, we see that sheet ice and ice jams are mainly influenced by the incidence angle, for open water this effect is less clear.

For smooth surfaces, such as sheet ice, the backscatter decreases with increasing incidence angle, as is indicated by Figure 2.9. This is clearly visible in Figures 5.10 [D], [E] and [F]. Sentinel-1 acquisitions of sheet ice were only obtained in a small range, between 37° and 44°. The influence of the backscatter is more reliable for RADARSAT-2, which acquired sheet ice SAR images for incidence angles ranging from 19° to 49°. RCM incidence angles also have a large spread and range from 17° to 47°. The decrease in backscatter for RADARSAT-2 is estimated on -1.7 ± 0.3 dB per 10° increase of incidence angle. For RCM a slightly smaller decrease of backscatter was found, namely -0.8 ± 0.4 dB per 10° increase in incidence angle.

For rough surfaces as ice jams, this decrease in backscatter is less pronounced. Rough surfaces cause diffuse scattering, which is to a lesser extent dependent on the look angle of a SAR sensor. Also for open water, a clear relation between backscatter and incidence angle is more difficult to identify. In a study on ocean wind, Geldsetzer et al. (2015) concluded that the backscatter of open water is not only correlated to incidence angle, but also to wind speed and wind direction. The latter two factors are not studied in this research.

Figure 5.11 shows the backscatter intensities of all pixels in the sample areas as a function of incidence angle. Only RADARSAT-2 and RCM data are presented, since Sentinel-1 acquisitions were obtained in a small range of incidence angles. In the Figures 5.11 [A] and [B] the predicted backscatter for sheet ice, ice jam and open water are defined by linear regression models. These lines are plotted in Figure 5.11 as solid lines. The 80% prediction interval is marked by dashed lines. The width of the prediction interval is due to speckle and diversity within an ice stage, such as roughness and dielectric constant. The prediction intervals of open water in Figures 5.11 [A] and [B] (in blue) do most likely not reflect the actual effect of incidence angle on water. A large negative slope is expected for open water pixels, as was illustrated in Figure 2.9. The open water pixels do not cover all wind situations nor all incidence angles, resulting in possible incorrect regression models.

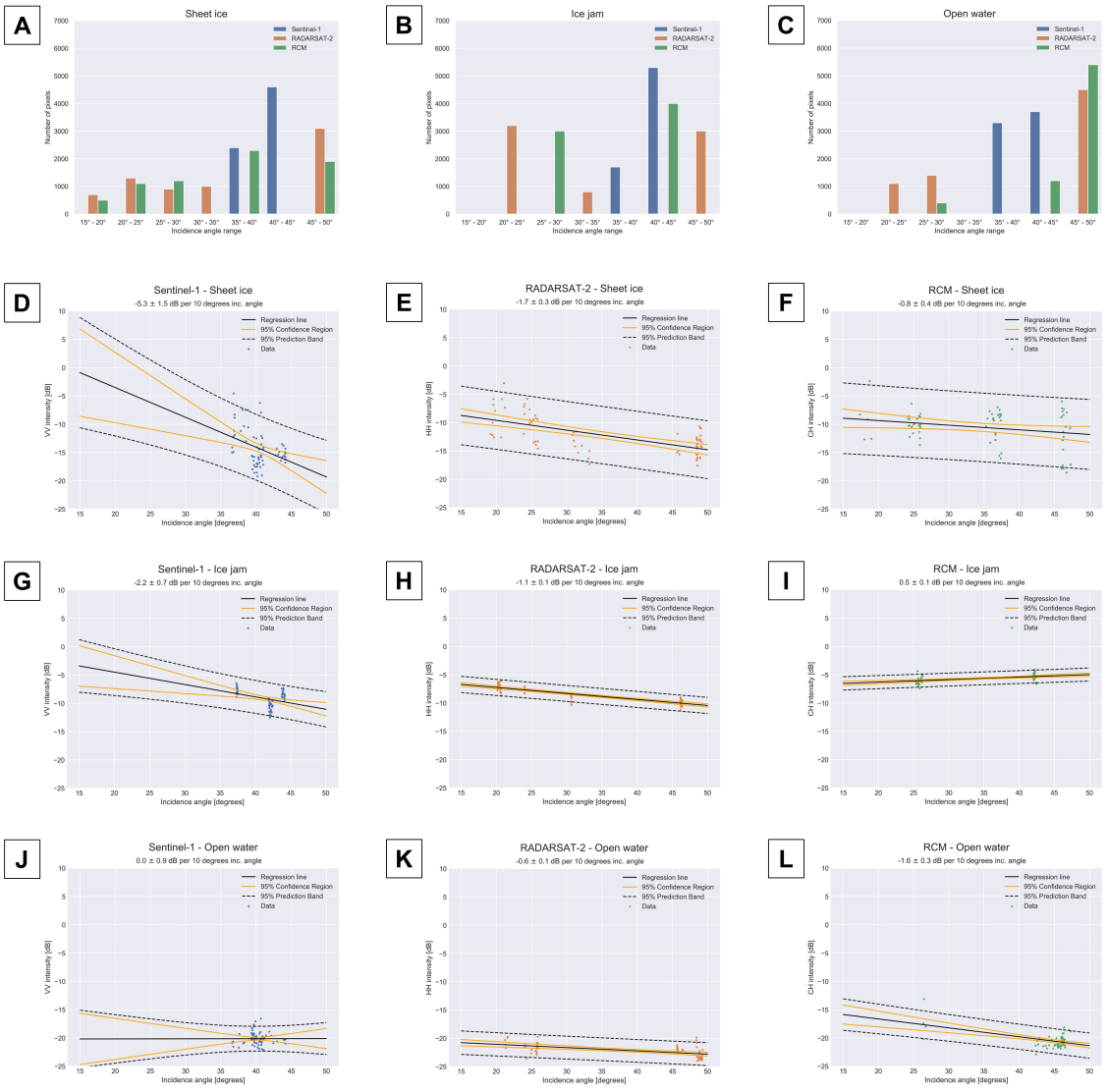

Figure 5.10: Influence of incidence angle on SAR backscatter. [A], [B] and [C] identify the range of incidence angles per ice stage for which SAR images were acquired. Sentinel-1 has a smaller range than RADARSAT-2 and RCM. Figures [D] - [L] show the effect on the SAR backscatter when the influence angle increases.

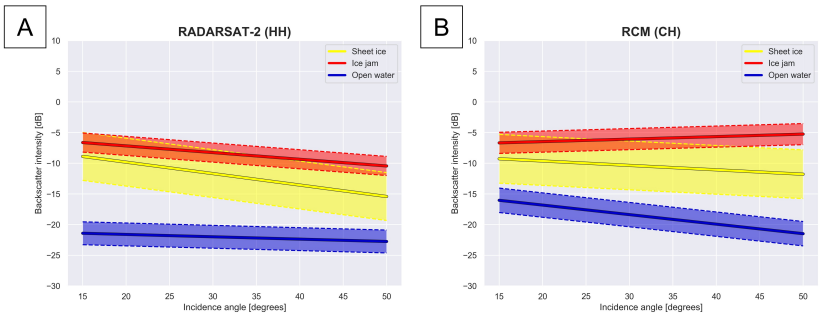

Figure 5.11: Influence of incidence angle on SAR backscatter per ice stage. Figure [A] shows the influence of incidence angle for RADARSAT-2 and Figure [B] for RCM. Sentinel-1 was not included, because sample areas over only a small range of incidence angles were studied. The solid lines represent linear regression models, the dashed lines the corresponding 80% prediction intervals.

5.2.4. NOISE FLOOR

Noise-Equivalent Sigma Zero (NESZ) is a measure of the sensitivity of a SAR system to low radar backscatter. A smaller NESZ is desired, since this enables a sensor to detect lower backscatter values. NESZ is given by the value of the backscatter coefficient corresponding to a Signal-to-Noise Ratio (SNR) of unity (Younis et al., 2009).

The cross-pol open water and sheet ice under melting condition values are typically very low and close to the noise floor. Often, these pixels are affected with noise. When a sensor has a lower noise floor, the measured difference in backscatter value between open water and ice can become larger, which might improve classification accuracies.

In Figure 5.8 [B] the cross-pol backscattered intensities are presented for the three ice stages of interest. Water has a very low backscatter, especially under larger incidence angles and specific wind speeds and directions (Geldsetzer et al., 2015). Figure 5.8 [B] gives an interesting view on the noise floor, because the backscatter of water is so low that it is close to the noise floor. Sentinel-1 did not measure values below -30 dB. RADARSAT-2 on the other hand, was able to detect smaller backscatter values of ± -33 dB. Please note that the noise floor depends on the imaging mode that is used and also varies within one SAR scene as a function of the incidence angle. Typically a poorer NESZ is found in images with a higher spatial resolution.

In literature, the minimum NESZ of Sentinel-1 IW was found to have a minimum of -22 dB (Potin, 2013). RADARSAT-2 quad-pol standard mode data has lower noise of -36 dB, the wide swath RADARSAT-2 ScanSAR have higher noise of -30 dB (Hwang et al., 2014). The NESZ of RCM is quite similar to Sentinel-1, and is calculated on -25 dB for 16 meter resolution compact-pol images and -24 dB for 30 meter compact-pol images (Thompson, 2015).

5.3. FEATURE ANALYSIS

In this work, nine features were extracted from Sentinel-1, fifteen from RADARSAT-2 data and six from RCM images. Figures 5.12, 5.13 and 5.14 present the values of these features per ice stage. The boxplots show the distribution of the feature values for the studied sample areas per satellite mission.

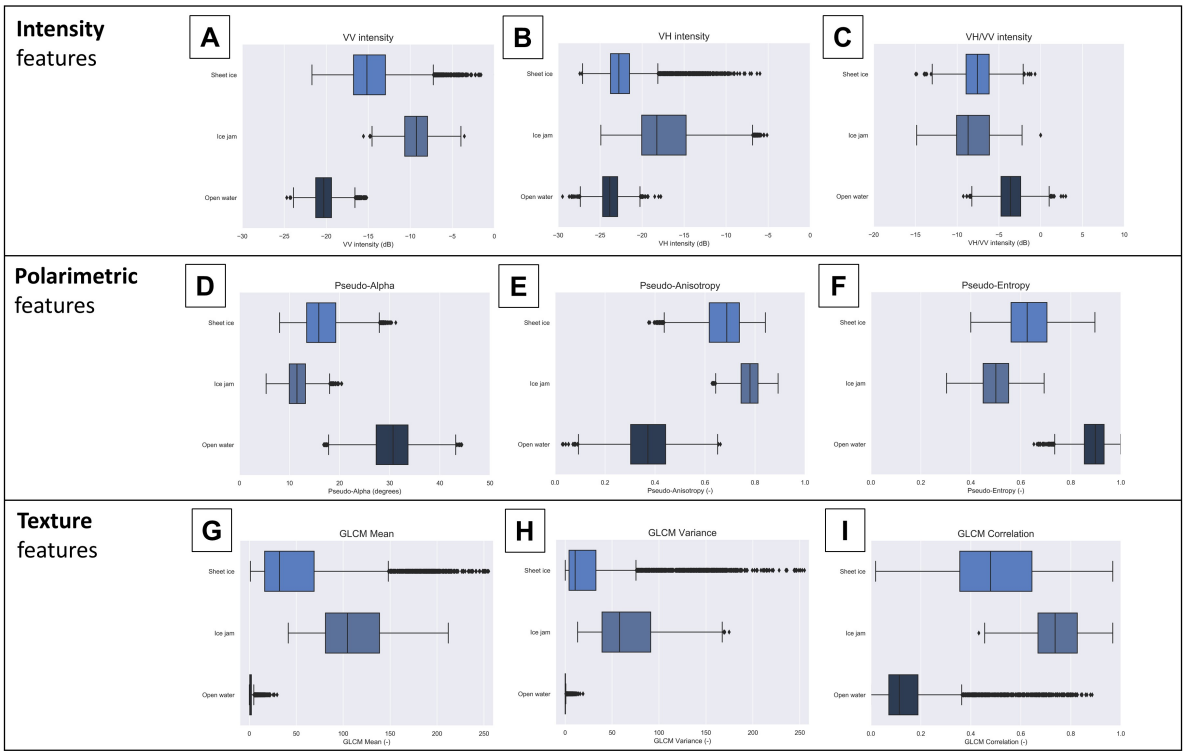

Figure 5.12: Feature analysis Sentinel-1. Nine features were investigated in this study: three intensity features, three polarimetric features and three texture features (based on VV).

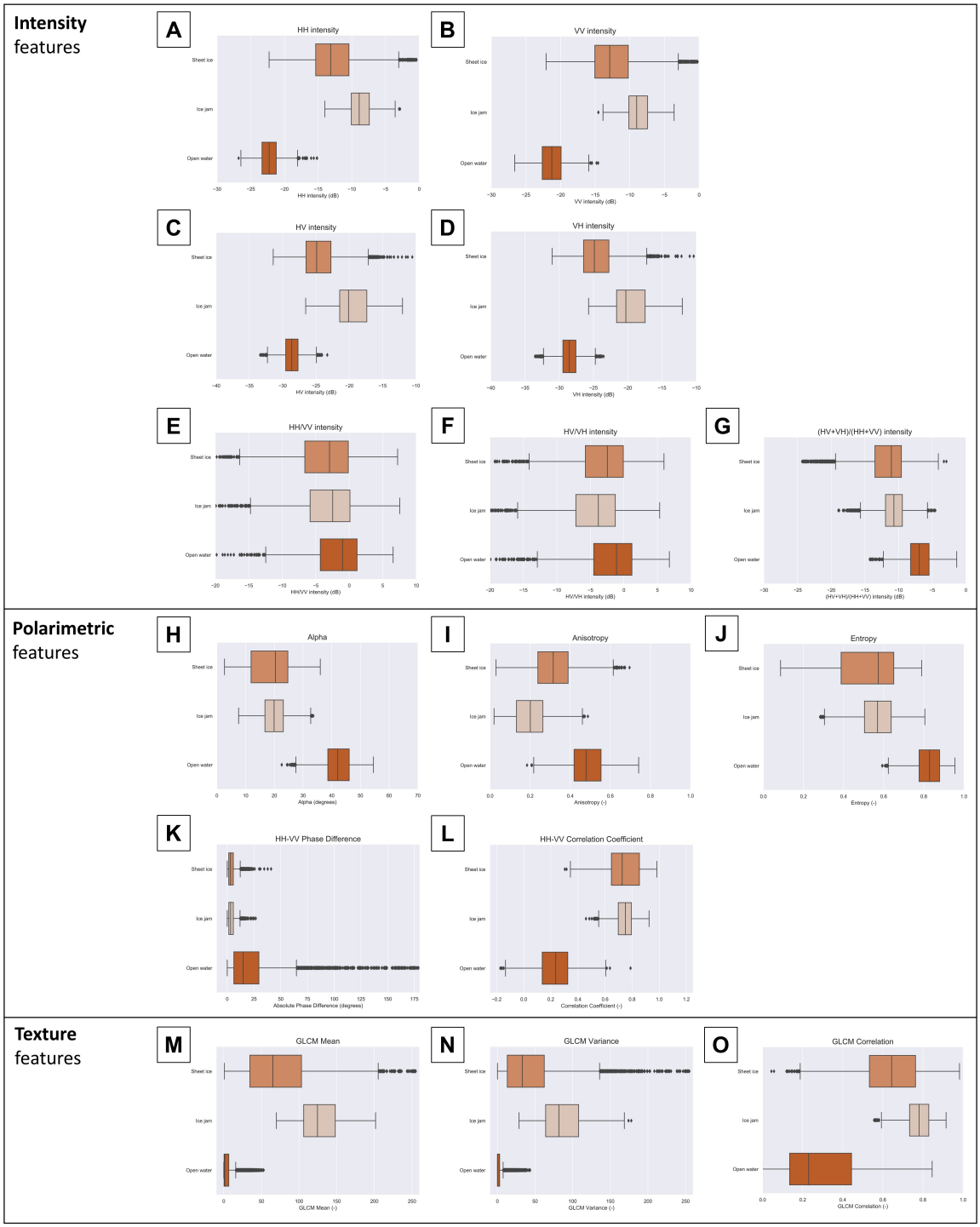

Figure 5.13: Feature analysis RADARSAT-2. Fifteen features were investigated in this study: eight intensity features, five polarimetric features and three texture features (based on HH).

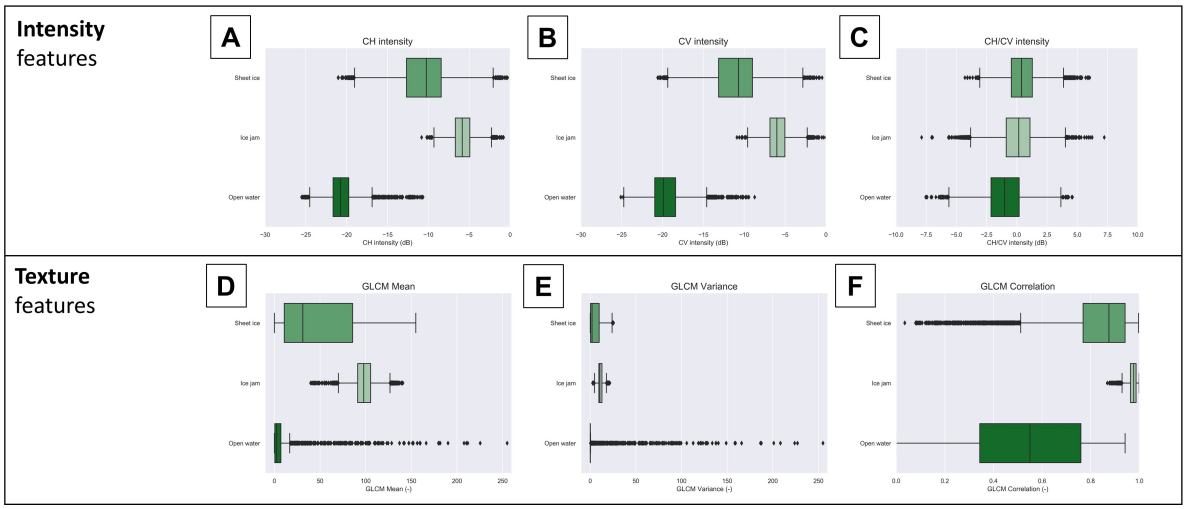

Figure 5.14: Feature analysis RCM. Six features were investigated in this study: three intensity features and three texture features (based on CH). Polarimetric features could not be computed, since there was no SLC data available.

It immediately can be seen that some features offer more utility for differentiating between ice stages than others. From the intensity features, the co-pol features seem best able to distinguish between open water, sheet ice and ice jams. Cross-pol backscatter intensities lay closer together for the three ice stages. In general, both for co- and cross-pol channels, ice jams have a higher backscatter than sheet ice. This could be explained by the rough surface and anisotropic nature, resulting in high scattering levels. The rough surface and anisotropic nature also cause radar signals to depolarize, explaining the high cross-pol values.

Pseudo-polarimetric and polarimetric features were extracted for Sentinel-1 and RADARSAT-2 respectively. For RCM there was no SLC data available, so no polarimetric information was available. Among the H-A-α decomposition parameters, Pseudo-Anisotropy and Pseudo-Alpha (for Sentinel-1) and Alpha (for RADARSAT-2) seem to be most suited to distinguish between the three ice classes. Alpha indicates the scattering type (surface, double-bounce and volume scattering). For sheet ice and ice jams, we see mainly surface scattering (values close to 0°). For open water there is a large spread in alpha variables (between 25° and 55°), while dominant surface scattering was expected for water pixels. These higher alpha angles, might be caused by noise.

Besides decomposition parameters, also the HH-VV correlation coefficient and HH-VV phase differences were computed. Open water has a low correlation between the HH and VV channels. It was found that the correlation coefficient was decreasing with increasing incidence angle. This could be due to the very low backscatter that the SAR antenna receives from smooth surfaces under large incidence angles, as was presented by Figure 2.9. The phase differences between the HH and VV channels are close to zero, with exception of some open water pixels were even values of 180° were reached. These high phase differences were reached at the RADARSAT-2 acquisition of 22 April 2019, for which the incidence angle was very large (around 50°). Although the open water pixels had a weak return signal (-23 dB on average), some of the energy that was reflected from the water surface resulted in a phase difference between HH and VV.

From the texture features GLCM mean seems to be best able to distinguish ice classes. The open water pixels are consistently black, resulting in the low GLCM mean values. The texture of sheet ice differs throughout the breakup season. Sheet ice in the early phase of the breakup season has a uniform high backscatter and a low variability in backscatter, which results in a high GLCM mean value. Later in the season, when it starts to melt, lower GLCM mean values are found. However, the backscatter pattern is less uniform than for open water, with a larger variability in backscatter over the melting area. Hence slightly higher GLCM mean values are found for sheet ice under melting conditions than for open water are found.

Now that all features have been presented in Figures 5.12, 5.13 and 5.14, only the best features will be selected for the RF classifications. Feature selection aims to reduce the number of features that describe the different classes. The benefit of this is a better performance of the classifier, since highly correlated and noise-

describing features are removed and calculation time is reduced. Figure 5.15 presents a correlation matrix per satellite mission, which enables the identification of possible dependencies between the analyzed features. From parameter pairs with a correlation higher than ±0.85, the least representative should be removed.

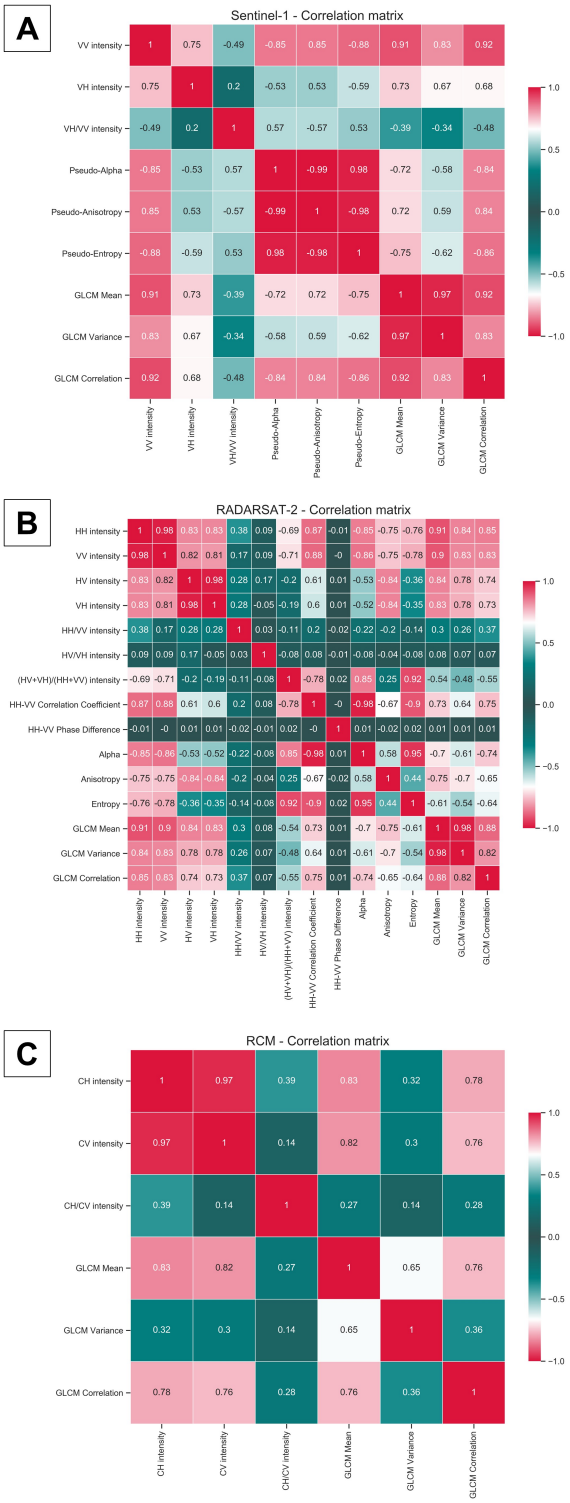

Figure 5.15: Feature correlation matrices of Sentinel-1, RADARSAT-2 and RCM. Many of the studied features are correlated over 80%. For highly correlated features only the feature with the highest descriptive value was kept.

Figure 5.15 shows the correlation coefficients between all used features. Plot [A] in Figure 5.15 presents the correlation matrix of Sentinel-1 features. The pseudo-polarimetric features are highly correlated. The same holds for the texture features (GLCM mean, GLCM variance, GLCM correlation). Also for RADARSAT-2 in plot [B], the texture features are highly correlated. However, the polarimetric decomposition parameter Anisotropy has a weak correlation with the other two decomposition parameters. A very high correlation between double co-pol channels (RADARSAT-2: HH and VV, RCM: CH and CV) and cross-pol (RADARSAT-2: HV and VH) is found, as previously explained based on Figure 5.8.

Figure 5.16 shows the importance of each feature in a RF classification and the classification accuracy based on the number of features used. The figures on the left, [A], [C] and [E] present the feature importance for the three satellite missions based on the Recursive Feature Elimination with Cross-Validation approach.

Some features that showed a high distinctive value between ice stages have relatively little importance. This is explained by the high correlation between some of the features, as was presented in Figure 5.15. When two features provide the same information, the feature importance of one will decrease. Several intensity and polarimetric features are not included in the graphs, since they only added noise to the RF classifier. For RADARSAT-2, the intensity ratios, phase information and correlation coefficient were not included. For RCM, the CH/CV intensity ratio did not have any additional value, so was excluded as well.

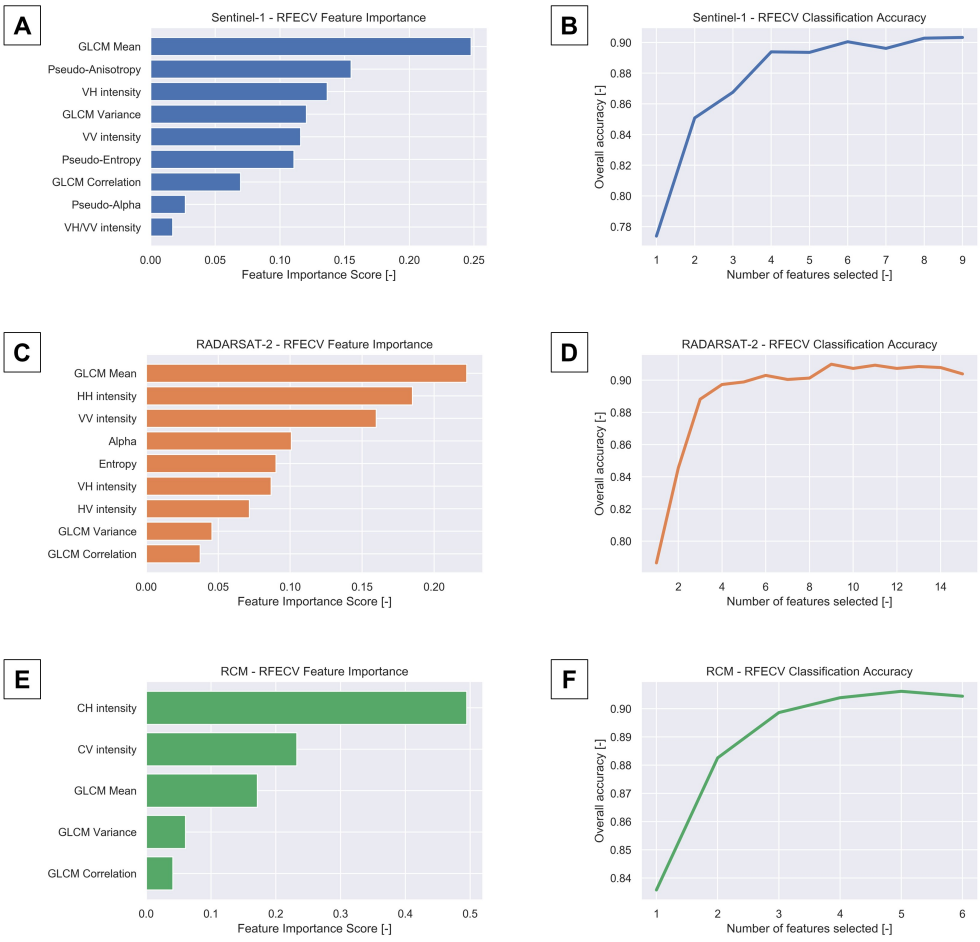

Figure 5.16: Recursive Feature Elimination with Cross-Validation (RFECV) to find optimal features for Random Forest classification of Sentinel-1, RADARSAT-2 and RCM. GLCM mean is the most important feature for Sentinel-1 and RADARSAT-2. For RCM the intensity features are most important when classifying sheet ice, ice jams and open water.

Figure 5.16, [B], [D] and [F] identify the classification accuracies based on the number of features used. The first feature being the most important feature, the second feature the second most important one, etc. For all satellite missions, the accuracy does not increase significantly after three or four added features. Because several of the features are highly correlated, it is not a surprise that most of them do not improve the classification accuracy.

Table 5.1: Selected features for each classification. 'Int' indicating that only intensity features could be selected, 'IntPolTex' means intensity, polarimetric and/or texture features were used.

	S1-Int	S1-IntPolTex	R2-Int	R2-IntPolTex	RCM-Int	RCM-IntPolTex
Intensity features	VV, VH	VH	HH, VH	VH	CH	CH
Polarimetric features	-	Pseudo-Anis	-	Alpha	-	-
Texture features	-	GLCM mean	-	GLCM mean	-	GLCM mean, GLCM var.

Based on the correlation matrices presented in Figure 5.15 and the feature elimination plots in Figure 5.16 only a limited number of features were selected to base the RF classifications on. Three classes of features were analyzes in this study, i.e. intensity, polarimetric and texture features. Most river ice classifications that are currently used only use the first class, i.e. intensity features. The added value of including polarimetric and/or texture features will be researched as well. Hence, for each satellite mission, two RF classifiers were built: an intensity features only RF classifications ('Int') and an intensity-polarimetric-texture RF classification ('IntPolTex'). Table 5.1 identifies the used features for all six classifiers.

5.4. ADDED VALUE OF POLARIMETRIC AND TEXTURE FEATURES

Based on the selected features that are presented in Table 5.1 six RF classifications were performed, namely S1-Int, S1-IntPolTex, R2-Int, R2-IntPolTex, RCM-Int and RCM-IntPolTex. The first two classification methods (S1-Int and S1-IntPolTex) were tested on sample areas from 12 Sentinel-1 images. R2-Int and R2-IntPolTex were tested on sample areas of eleven RADARSAT-2 images. The last two classifiers RCM-Int and RCM-IntPolTex were tested on sample areas of thirty-one different RCM scenes.

Table 5.2: Statistical metrics of RF classifications. 'Int' indicating that only intensity features could be selected, 'IntPolTex' means intensity, polarimetric and/or texture features were used.

	S1-Int	S1-IntPolTex	R2-Int	R2-IntPolTex	RCM-Int	RCM-IntPolTex
Overall Accuracy	0.823	0.856	0.876	0.912	0.840	0.910
Cohen's Kappa	0.735	0.784	0.814	0.867	0.760	0.865
Variance of Cohen's Kappa	5.399e-05	4.601e-05	4.016e-05	3.016e-05	5.046e-05	3.063e-05

Per satellite mission 60 sample areas (each consisting of 100 pixels) were used for validation. The RF methods performed very well overall. Each satellite mission had an average accuracy over 82% based on intensity features only and over 85% when also polarimetric and texture features were included. RADARSAT-2 and RCM had the highest agreement with reference data, resulting in an average accuracy of 91%. Table 5.2 details the classification accuracy of each class and satellite mission. Based on the Cohen's Kappa statistics the $\Delta\hat{K}$ can be computed. The results are presented in Table 5.3.

Table 5.3: Hypothesis testing for significant difference between 'Int' and 'IntPolTex' classifiers. The significant difference between the classification results were carried out at a 95% confidence level.

	S1-Int vs. S1-IntPolTex	R2-Int vs. R2-IntPolTex	RCM-Int vs. RCM-IntPolTex
Kappa statistic $\Delta\hat{K}$	4.925	6.320	11.716

The Kappa statistics presented in Table 5.3 indicate that, at the 95% confidence level, the 'IntPolTex' classifiers are significantly better than the 'Int' classifiers for all three satellite missions. Hypothesis testing was not performed to compare Sentinel-1, RADARSAT-2 and RCM classification results. For each satellite mission, different sample areas were selected, which complicates comparison between the missions.

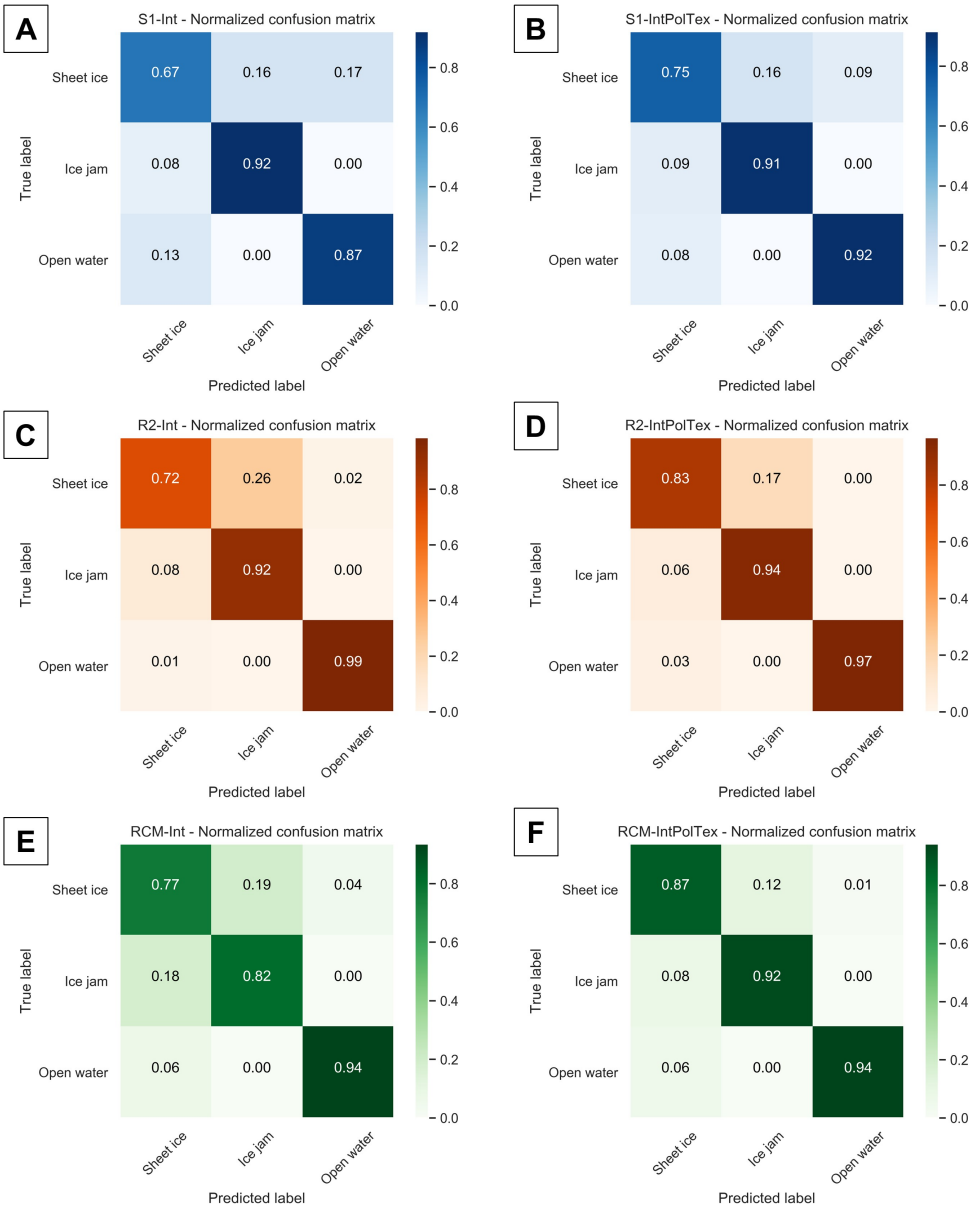

Figure 5.17: Normalized confusion matrices of RF classification for Sentinel-1, RADARSAT-2 and RCM. [A], [C] and [E] show the confusion matrices for RF classifications based on intensity features only. [B], [D] and [F] show the matrices for classifications based on intensity, polarimetric and texture features.

In Figure 5.17 the confusion matrices of all classification methods are presented. Both for 'Int' and 'IntPolTex' the highest accuracies are reached for the ice jams and open water classes and the lowest for sheet ice. In the Sentinel-1 classifiers, sheet ice was sometimes misclassified as ice jams (for both classifiers: 16%) and sometimes as open water (S1-Int: 17%, S1-IntPolTex: 9%). Due to the large spread in feature values, sheet ice is difficult to correctly classify. In the beginning of the breakup season, volume scattering results in a high signal return. When the breakup season evolves and temperatures increase, the sheet ice starts to melt. This leads to a decreasing signal, which is (almost) similar to water.

The overall accuracy, when including polarimeric and texture features, increases with 3.3% for Sentinel-1,

3.6% for RADARSAT-2 and 7.0% for RCM. The kappa statistics indicate that all 'IntPolTex' perform significantly better than the 'Int' classifiers. The increased accuracy of Sentinel-1 can be assigned to an improved distinction between sheet ice and open water. Less sheet ice pixels were labeled as open water (8% less) and less open water pixels were labeled as sheet ice (5%). This improvement was accomplished mainly because GLCM mean was included in the S1-IntPolTex classifier. The boxplot of the GLCM mean feature in Figure 5.12 shows the extremely low values for open water. Because open water is a monotonic dark area in SAR images, it gives very low GLCM mean values. Melting sheet ice shows a less uniform backscattering pattern in a larger window box and also includes some brighter pixels. Because GLCM mean uses a relatively large window of 11 x 11, the GLCM features are rather homogeneous. Even though the SAR images are not speckle filtered before computing the GLCM features (see preprocessing scheme *C* in Figure 4.2), speckle noise is less pronounced. Accuracy improvements of the RADARSAT-2 and RCM classifications were mainly achieved because more ice jam and sheet ice pixels were classified correctly. Most pixels that were misclassified as ice jams instead of sheet ice, had small incidence angles.

More in-depth details about the relation between SAR characteristics and misclassified pixels can be found in Figures 5.18 and 5.19. These figures were created based on the S1-IntPolTex, R2-IntPolTex and RCM-IntPolTex classification results. Figure 5.18 gives an insight on the dates at which there was confusion between ice stages. Figure 5.17 shows that Sentinel-1 sheet ice pixels were misclassified as ice jams and as open water. For RADARSAT-2 and RCM, sheet ice pixels were occasionally misclassified as ice jams and vice versa. Only the ice stages with high confusion are presented in Figures 5.18 and 5.19.

Figure 5.18 [A] and [B] show that sheet ice was misclassified as open water at 24 March 2019, 28 March 2019 and 23 April 2020. The reference data show that parts of the ice layer were covered by melt water. Figure 5.18 [C] show that almost 60% of the sheet ice pixels were misclassified as water. An explanation can be given by the recent snowfall event which took place at 4 April 2019, resulting in a snow layer with a rough surface on top of the ice.

The misclassification between sheet ice and ice jams presented in Figure 5.18 [E], [F], [G] and [H] is best explained by 5.19. This figure shows that for RADARSAT-2 and RCM most pixels that were misclassified as ice jams instead of sheet ice, have small incidence angles. For example Figure 5.19 [E] shows that almost 50% of the RADARSAT-2 sheet ice pixels were misclassified as ice jam, when the incidence angle was smaller than 20°. This can be explained by Figure 2.9, which shows that smooth surfaces like sheet ice, the SAR sensor measures a high backscatter under small incidence angles.

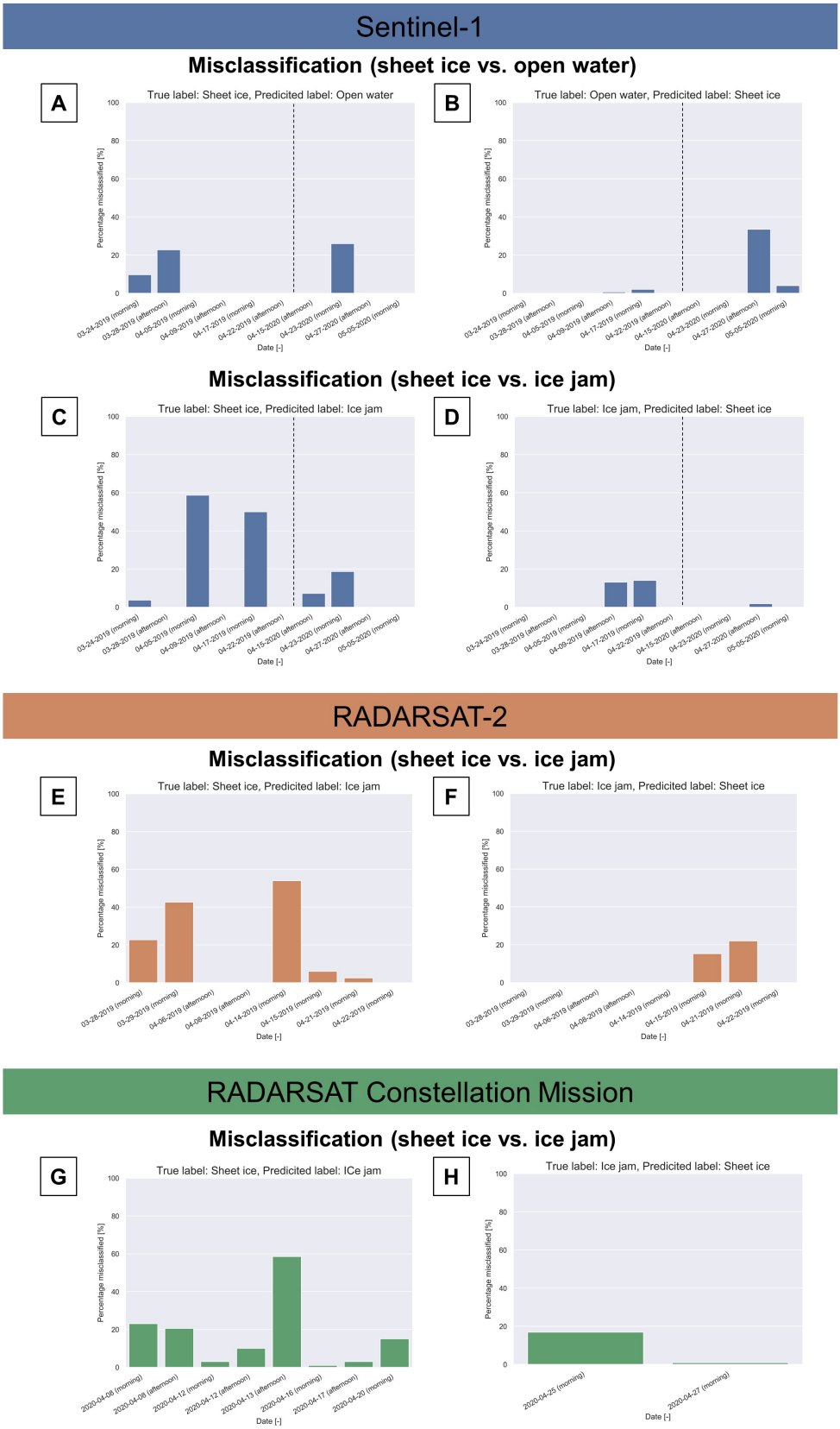

Figure 5.18: Percentage of misclassified pixels per date. [A] and [B] show the confusion between sheet ice and open water for Sentinel-1. [C] and [D] show at which dates there was confusion between sheet ice and ice jam for Sentinel-1, [E] and [F] for RADARSAT-2 and [G] and [H] for RCM.

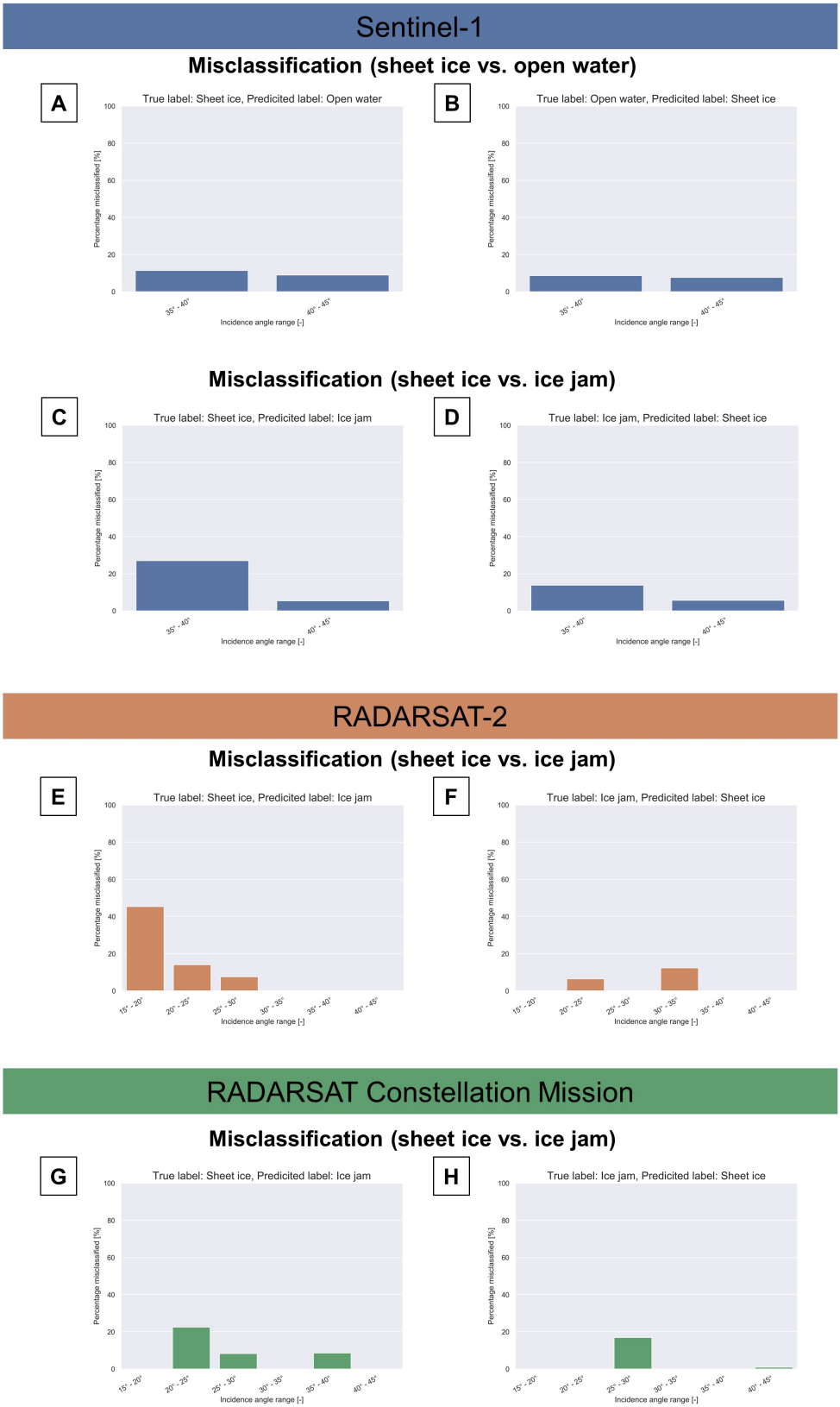

Figure 5.19: Percentage of misclassified pixels per incidence angle. [A] and [B] show the confusion between sheet ice and open water for Sentinel-1. [C] and [D] show at which incidence angles there was confusion between sheet ice and ice jam for Sentinel-1, [E] and [F] for RADARSAT-2 and [G] and [H] for RCM.

5.5. CLASSIFICATION MAPS

In Appendix E classification maps of the entire studied river stretch are presented. In Figures E.1, E.2 and E.3 it is visible that there are small differences between the 'Int' and 'IntPolTex' classification results. Unfortunately, there are no reference data available for every date there was a SAR acquisition. For some dates however, there are reference photos at hand, together with the interpretation of the ice stages performed by AEP (see Tables A.1 and A.2 in Appendix A). Figures 5.20, 5.21 and 5.22 present 'Int' and 'IntPolTex' classification results and compare the results with reference photos acquired by AEP.

In the classification maps that are shown in Figures 5.20, 5.21 and 5.22, the 'IntPolTex' classifiers show a smoother result than the 'Int' classifiers. This can be explained by the additional texture features in the 'IntPolTex' classifiers, because the texture features also take the values of neighbouring pixels into account. The effect on the computed texture features differs per SAR image, since the spatial resolution has a large effect on the texture. All Sentinel-1 images used in this study have a nominal spatial resolution of 5 x 20 meters (see Table 3.1). The spatial resolution of RADARSAT-2 scenes differ from image to image. Most of the images have a spatial resolution of around 20 x 20 meters (see Table 3.2). For RCM, two different spatial resolutions were used, 16 x 16 meters and 30 x 30 meters (see Table 3.3).

Figure 5.20 [A], obtained at 5 April 2019, shows a downstream stretch of the Athabasca River with an intermitted ice cover. Both classifiers, S1-Int and S1-IntPolTex, classify some of the pixels as ice jam. The S1-Int classifier captures some of the open water leads that are present in this part of the river at 5 April 2019. The 'IntPolTex' classifier on the other hand, misses most of these open water leads and classifies these areas as sheet ice. Maps in Figure 5.20 [B], dated at 22 April 2020, give a closer look into misclassified open water pixels. In reality, in these locations the ice has started to melt. However, this is not recognized by the classifiers. It should be noted that this is a limitation of radar earth observation. It is visible that the 'IntPolTex' does a slightly better job than the 'Int' classifier. This difference was also shown in the confusion matrices of Figure 5.17. The third images were acquired at 27 April 2020, see Figure 5.20 [C]. The head of the ice jam is clearly visible in the AEP helicopter photo. Both classifiers are well able to detect the ice jam and classify most pixels correctly. However, the 'IntPolTex' classifier shows an artifact. At the transition of open water to ice jam, a small edge of sheet ice shows up. This is an artifact from the texture feature, calculated using a window of 11 x 11. The 'Int' classifier labeled some of the pixels as sheet ice in the open water lead, where the observation photos show open water. The 'IntPolTex' classifier is able to detect this correctly.

Figure 5.21 [A] shows a downstream stretch of the Athabasca River, where the river is covered with sheet ice. This part of the river is just downstream the Athabasca River Bridge, located near downtown Fort McMurray. In both classifiers, R2-Int and R2-IntPolTex, some pixels are misclassified as open water. The 'IntPolTex' classifier labeled pixels as open water close to the bridge. In the 'Int' classifier some pixels in the sheet ice part are misclassified. Figure 5.21 [B] shows an intermitted ice cover at 15 April 2019. Both classifiers show comparable results to the AEP reference photo. Again, it is visible that the classification of 'IntPolTex' is more smooth. The final image presented in Figure 5.21 shows ruble ice. In the observation photo, an ice jam and an ice run are visible. The SAR acquisition was obtained the morning after the observation photo. It is possible that the ice run was not present at the time of the SAR acquisition. Both classifiers show that a part of the river was free of ice on the morning of 22 April 2019, except for some ice remnants stranded on shoals and along shores.

For the classification maps of RCM in Figures 5.22 [A] and [B], obtained at 21 and 25 April 2020, the differences between the 'Int' and 'IntPolTex' classifiers are small. In these cases, the 'IntPolTex' classifiers show slightly more correctly classified pixels. Figure 5.22 [C] shows a toe of the ice jam. Both classifiers can capture the head of the ice jam accurately. However, similar to the classification result of S1-IntPolTex in Figure 5.20 [C], there is an artifact of the texture features. An edge of sheet ice shows up, at the transition of open water to ice jam.

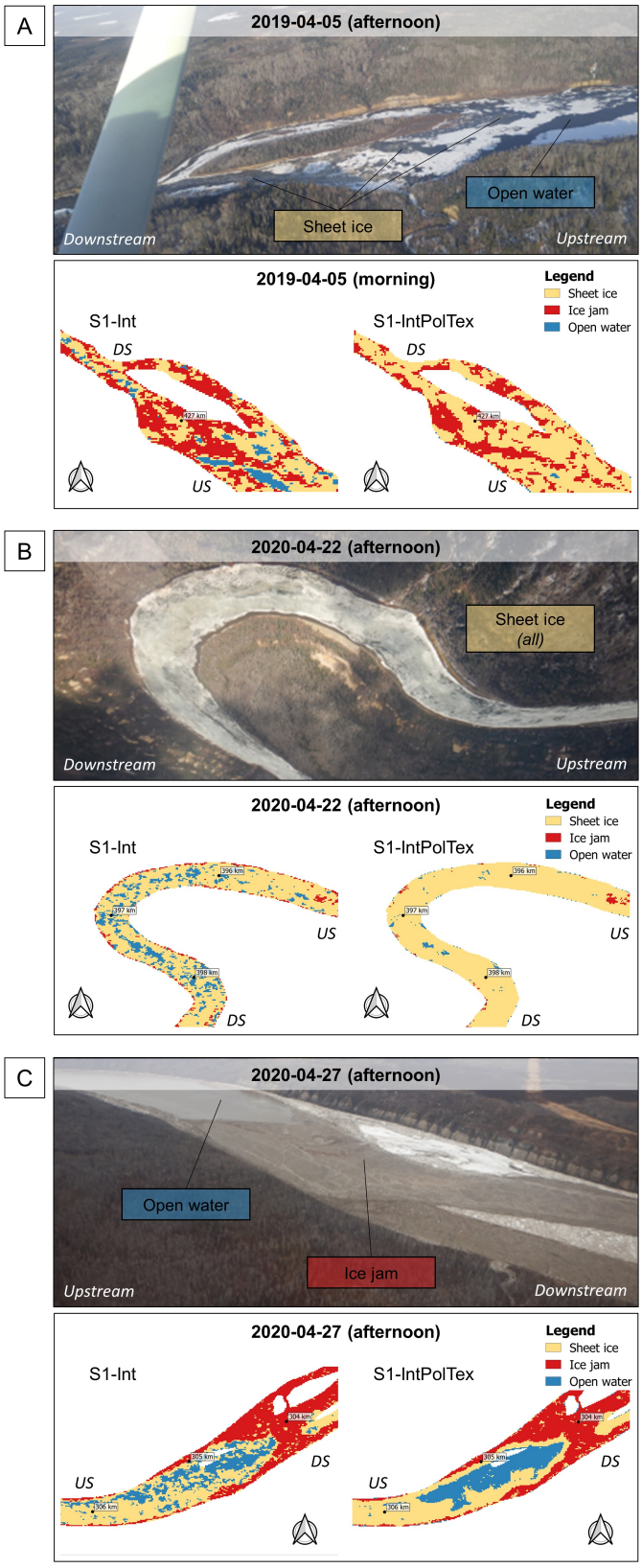

Figure 5.20: Classification comparison between S1-Int (based on: VV, VH features) and S1-IntPolTex (based on: VH, pseudo-anisotropy and GLCM mean features) for three selected areas. Image [A] and [B] show sheet ice under melting conditions. Image [C] shows that both classifiers are able to detect the ice jam of end-April 2020.

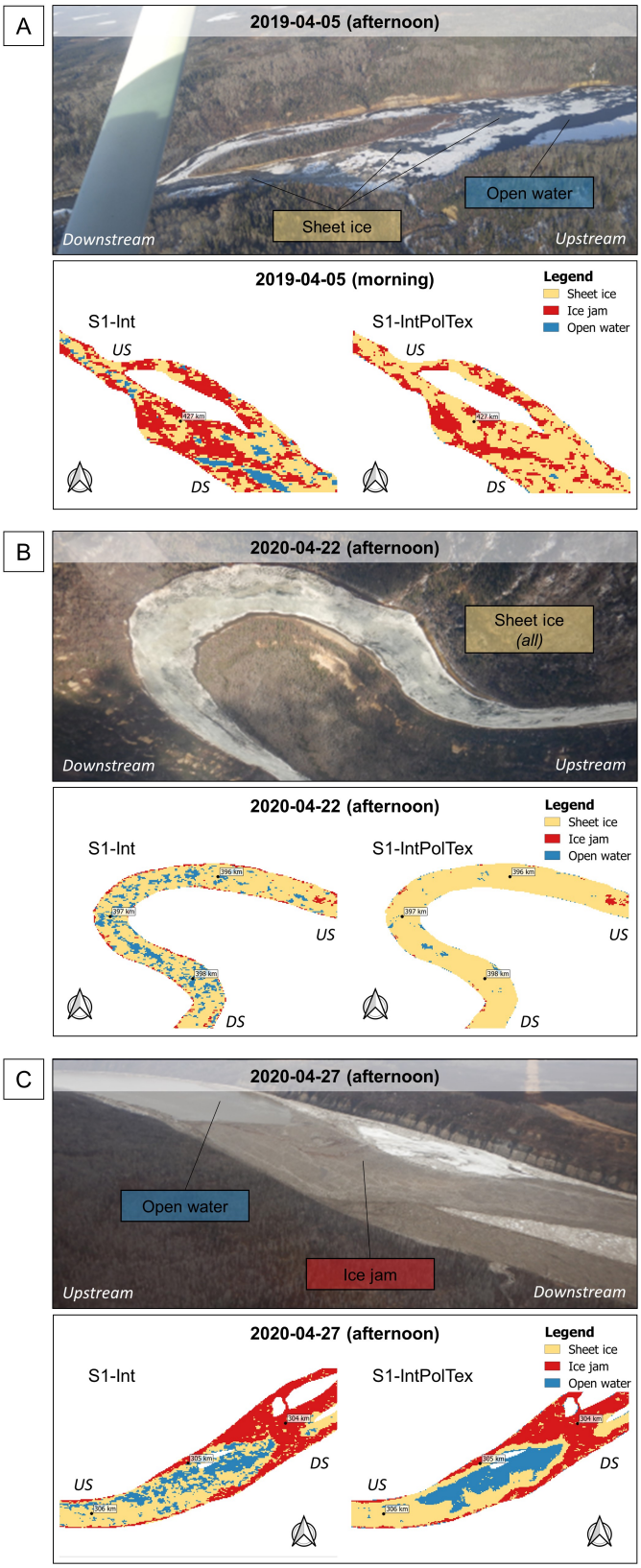

Figure 5.21: Classification comparison between R2-Int (based on: HH, VH features) and R2-IntPolTex (based on: VH, alpha, GLCM mean features) for three selected areas. The first two comparisons [A] and [B] show that both classifiers have trouble correctly classifying sheet ice under winter conditions. Image [C] shows an ice run, which was not captured by the classification maps

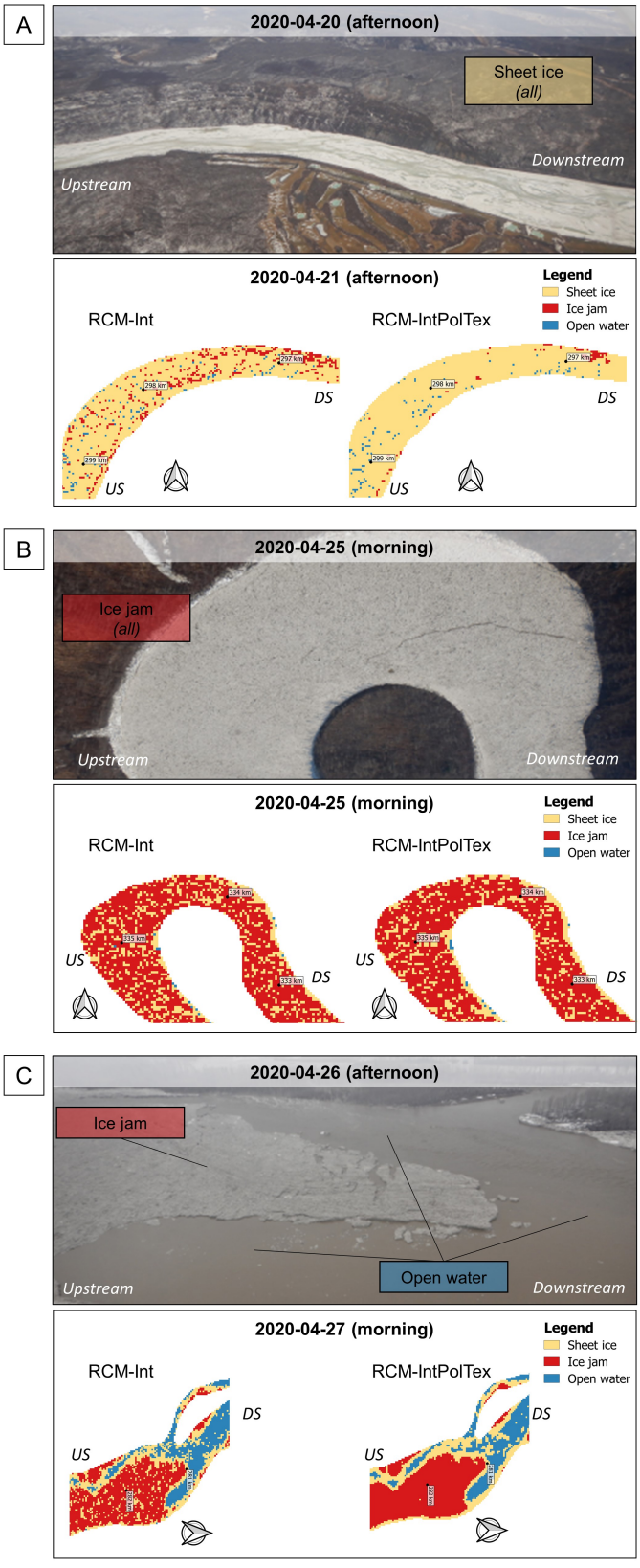

Figure 5.22: Classification comparison between RCM-Int (based on: CH feature) and RCM-IntPolTex (based on: CH, GLCM mean and GLCM variance feature) for three selected areas. The first image [A] shows a stretch of the Athabasca River where the river is covered with sheet ice. Images [B] and [C] show an ice jam. The rubble ice was captured by all classifiers. However, the RCM-IntPolTex classifier shows an artifact at 27 April 2020.

6

DISCUSSION

The discussion consists of two parts. Section 6.1 discusses this study in a wider context. The added value of SAR polarimetry for river ice classification during breakup is discussed. Section 6.2 examines some of the decisions and assumptions that were made during this research.

6.1. RADAR POLARIMETRY

The main purpose of this study was to examine the possibility of using intensity, polarimetric and texture features to improve river ice classification. The results presented in the previous chapter showed that classifiers that included intensity, polarimetric and texture features (i.e. the 'IntPolTex' classifiers) gave significantly better classification results than classifiers that solely used intensity features (i.e. the 'Int' classifiers). However, the greatest added value in the 'IntPolTex' classifiers came from texture features, not from polarimetric features (see the importance of each feature in Figure 5.16). Texture features can be computed based on non-polarimetric data. This raises the question of whether polarimetric SAR data are required to capture the different ice stages during breakup or whether non-polarimetric SAR data also satisfy.

This was not the only reason this question arose. The fully polarized RADARSAT-2 data do not show better results than the dual-pol Sentinel-1 and non-polarimetric compact-pol RCM. Data from RADARSAT-2 is fully polarimetric and consists of four polarimetric channels (HH, HV, VH and VV) and phase information. Sentinel-1 is a phase-preserving dual-pol SAR system. For RCM only GRD data were available, so non-polarimetric compact-pol data were used. Even though in this study no direct comparison between classification results of Sentinel-1, RADARSAT-2 and RCM was performed, it is clear that high accuracies were obtained for all satellite missions (i.e. 85.6% (Kappa = 0.78) for S1-IntPolTex, 91.2% (Kappa = 0.87) for R2-IntPolTex and 91.0% (Kappa = 0.87) for RCM-IntPolTex).

This study did not compare whether 'IntPol' classifiers perform better than 'Int' classifiers. Based on the boxplots presented in Figures 5.12, 5.13 and 5.14 it is expected that the polarimetric features will not greatly improve classification accuracies. This means that when classification would be performed with GRD data, results are expected to be comparable to current 'Int' results. It is recommended to validate this in further research.

However, even though polarimetry is not expected to improve classification accuracy, polarimetry does add additional information. When more polarimetric channels are available, more information about the ice stages can be retrieved from the (de)polarized signals. Moreover, decomposition parameters allow separation of scattering mechanisms in surface and volume scattering, which gives more information about the river ice processes. There are great potentials for more advanced river ice classifications, in which radar polarimetry can play a major role.

6.2. REFLECTION OF RESULTS

This research shows a classification method that results in an accurate discrimination between sheet ice, ice jams and open water. However, the used research method is based on several assumptions that strongly

influence the certainty of the classification results per location. In this section, critical assumptions and other factors that constrain direct applicability of the results are discussed and comparisons are made with previous findings in literature. Firstly, the use of a Random Forest model is discussed and compared with the more commonly used threshold method in 6.2.1. Secondly, the quality of the selected features is discussed in 6.2.2. Finally, the method that was used to obtain training and validation data is critically reviewed in 6.2.3.

6.2.1. COMPARING THRESHOLDING WITH MACHINE LEARNING CLASSIFIERS

Several studies use supervised classification methods to monitor ice decay from SAR images. Most of these studies use threshold-based methods, for example Mermoz et al. (2009) who studied river ice under winter conditions and Geldsetzer et al. (2010) and van der Sanden and Geldsetzer (2015) who studied lake ice. Fixed backscatters are used to distinguish ice and water pixels. In this study a different approach was used, several machine learning classifiers were tested (see Section 2.5) and eventually a Random Forest classification was carried out.

Both threshold-based and machine learning classifiers have their advantages and disadvantages. A machine learning model utilizes statistical rules rather than a deterministic approach, while a threshold classifier could be considered as having "fixed" intelligence. Even though a machine learning system still uses a layer of underlying rules, the machine has the ability to learn new rules on its own and discard ones that are not useful. Moreover, more features can be added very easily to a machine learning classifier, which was found to be highly beneficial for classification accuracies (see Table 5.2 for comparison 'Int' vs 'IntPolTex'). A Random Forest model is able to calculate the importance of each feature, which can be used to better understand the underlying processes of radar and river ice interaction.

On the other hand, the RF approach used in this study is less interpretable than a basic threshold method. However, in the author's opinion, this disadvantage of a black box approach does not outweigh the aforementioned advantages. Besides these benefits, RF is able to handle non-linear data and is resistant to outliers.

6.2.2. ADDITION OF POLARIMETRIC AND TEXTURE FEATURES

Many studies on the monitoring of river ice only used co-pol intensities as input for classification (e.g. Floyd et al., 2014, Gauthier et al., 2010, Sobiech and Dierking, 2013). This study aimed to get more out of the SAR data than co-pol backscatter alone and studied the added value of multiple polarimetric channels, phase information, decomposition parameters and texture features.

The RF-recursive feature elimination in Figure 5.16 showed the importance of texture feature GLCM mean. Already in 2006, Gauthier et al. (2006) found that texture features performed better than intensity features as inputs of a fuzzy-k-means classification. Similar to this study, it was found that the texture-based classification was more efficient in discriminating areas with smooth surfaces to moderately rough surfaces, such as open water and sheet ice under melting conditions.

In this study, three different feature classes (intensity, polarimetric and texture) were used to describe the three ice stages. Table 5.2 shows that the additional polarimetric and texture features increased classification accuracies up to 7%. Even though the classification already improved significantly by adding polarimetric and texture features, the classification performance may increase even further by refining the features. Several points of discussion are highlighted below.

Firstly, the distribution of the sample areas directly affects the feature values. Since only pixels in homogeneous areas were used for training and validation data, some patterns may not be captured. This means that the selected features might not be representative in complex regions of the river. More detailed ground-truth data may resolve this issue.

Secondly, the selected features may not be the most important feature for each SAR image. Especially texture, which heavily relies on window size, is dependent on spatial resolution. The Sentinel-1 and RADARSAT-2 images that were used in this study have a consistent spatial resolution (around 20 m). On the other hand, RCM images were acquired under different spatial resolutions (16 m and 30 m). However, neither of these spatial resolution modes had enough images available to develop a proper training and validation data set on its own. Therefore, the 16 m and 30 m RCM data sets were combined, resulting in selected texture features that do not lead to optimal discrimination between the different ice stages. When more RCM SAR data are available (for example breakup season 2020-2021), separate classifiers could be trained and validated for each beam mode.

Moreover, the results show that the acquisition time and incidence angle influence the feature values. However, the RF classifiers developed in this study did not account for these effects. The performance of the classifiers may improve when these influencing SAR characteristics are added as variables. However, in this thesis a lack of data made these improvements impossible. For example, no ice jams were captured during RCM afternoon overpasses. Also, not all ice stages were imaged under varying incidence angles.

Finally, only ground range detected RCM data products were available. Therefore no compact-polarimetric information was available, leading to a limited amount of features that could be computed. Single look complex data may significantly improve the RCM classification, as simulated RCM phase information has proven useful in previous studies dealing with sea ice (Dabboor and Geldsetzer, 2014) and lake ice (van der Sanden et al., 2014).

6.2.3. UNCERTAINTIES IN SAMPLE AREA SELECTION

Many studies on river ice classification used unsupervised classification approaches, such as the fuzzy k-means classification method (e.g. Chu and Lindenschmidt, 2016, Gauthier et al., 2006, Sobiech and Dierking, 2013). However, unsupervised classification has some large drawbacks compared to supervised approaches, since one has little control over the selected classes and often the spectral classes do not correspond to features on the ground (Campbell and Wynne, 2011).

In this study, a supervised classification approach was used, which required prior training. All training and validation sample areas were drawn and labeled manually based on the author's interpretation of the reference data. Supervised classification can be much more accurate than unsupervised classification, but depends heavily on the quality of the training data. Three sources of uncertainties that may lead to errors or deficiency in the sample areas are mentioned below.

First of all, misinterpretation of the reference data can lead to incorrectly labeled sample areas. The observation reports from AEP labeled the river ice stages per kilometer. However, differences in ice stages also occur on smaller scales. Also, time differences between the acquisition of the SAR images and Sentinel-2 imagery or AEP observation flights can also reduce training data quality. Even though AEP conducted daily observation flights during the breakup seasons, time differences between SAR imagery and AEP flights of up to 8.5 hours can occur.

Secondly, the number of labeled classes may have impacted the results. During sample selection, areas were labeled into three classes: sheet ice, ice jam and open water. However, scattering behaviour of river ice under winter conditions and sheet ice under melting conditions differ significantly. Even though, in this study it was aimed to not select areas with ice under winter conditions for the sample selection, this did not also succeed. Some of the selected sheet ice sample areas show a very high backscatter, as is found for river ice under winter conditions (for example after the snowfall event of 4 April 2019). In future research, the current sheet ice class should be split up.

Finally, in order to efficiently select the sample areas, only pixels in homogeneous areas were selected, for which the author was confident about the ice stage. As a result, areas with ambiguities, such as ice-water boundaries, were avoided. Hence, these complex regions were underrepresented in the training data. If ground-truth data would have been available at these regions, RF classification could be improved.

A preferred approach is to collect field data on the same day as SAR images are acquired. Several other studies (e.g. Mermoz et al., 2009, van der Sanden et al., 2009, Weber et al., 2003) improved their classification by adding field observations. In these studies, ground-truth data were collected from observation flights scheduled to be simultaneous with SAR image acquisitions. During critical stages of a dynamic ice breakup, time-lapse pictures with a high temporal resolution (e.g. one image per minute) are required to capture all the changes.

7

CONCLUSIONS

This study assessed the classification potentials and limitations of Sentinel-1, RADARSAT-2 and RCM for river ice classification during breakup. The key findings obtained during this study are presented in Section 7.1. First, the sub-questions are discussed, followed by the main research question. During this thesis research, hypotheses were developed for the estimated feature values per ice stage (Figure 2.16). Most of these hypotheses could not be rejected. However, there are also some proposed improvements, see Section 7.2. Finally, three recommendations for future research are listed in Section 8.

7.1. KEY FINDINGS

What is the effect of the characteristics of the different SAR acquisitions on river ice classification?
The contrast between ice and water depends on the satellite configuration used. Hence, a simple threshold approach that would work for all satellite missions is not possible. In this thesis, the effect of radar polarization, incidence angle and acquisition time was studied.

When looking at **polarization channels** a distinction between co-pol and cross-pol channels was made in this study. Co-pol channels HH, VV, CH and CV (the latter two are not actual co-pol channels) and cross-pol channels HV and VH were considered. During breakup, the depolarization rates are very small for most ice stages, resulting in low cross-pol values with a low signal-to-noise ratio. Therefore, when solely using cross-pol intensities, classification possibilities are very limited. Co-pol intensities show a better separation between the ice classes. Among co-polarization channels, circular polarization (CH, CV) performed better than linear polarization (HH, VV). A clear reason has not been identified and more research on this is required.

Secondly, the **incidence angle** influences the backscatter measured by a SAR sensor. SAR images acquired under small incidence angles result in a high returned radar signal for all ice stages. During breakup, the backscatter of both sheet ice and open water mainly consists of specular surface reflection. This specular reflection results in high backscatter under small incidence angle, making classification difficult (see Figure 5.11). Therefore, it would be optimal to only use SAR images with large incidence angles, e.g. over 40 °. However, this would drastically reduce the amount of SAR images available for classification. Based on the misclassification plots of RADARSAT-2 and RCM presented in Figure 5.19, it is recommended to avoid SAR images with incidence angles smaller than 30°. Unfortunately, in this study the SAR images acquired with incidence angles < 30° could not be ignored, due to a limited amount of data.

The effect of the difference in **acquisition time**, i.e. morning vs. afternoon overpasses, is less pronounced than the effect of polarization channels or incidence angle on the backscatter. Nevertheless, for sheet ice pixels there is a small difference in backscatter between the morning and afternoon acquisitions. Due to the melt development after a day of solar radiation and higher temperatures, the backscatter shows lower values in the afternoon overpasses. Therefore, SAR images obtained during morning overpasses are better able to distinguish between open water and sheet ice and result in higher accuracy.

The **noise floor** of each satellite mission was studied. The noise floor varies between imaging modes. Similar to what was found in literature, quad-pol RADARSAT-2 has a significantly lower noise floor than dual-pol

Sentinel-1 and compact-pol RCM. A low noise floor is beneficial for the discrimination of ice types with a low backscatter, such as open water and sheet ice under melting conditions.

The mentioned characteristics certainly induce limitations when it comes to river ice classification using. During classifier development, these limitations should be taken into account. It would be desirable to only use 'optimal data'. When the classifier is in use, the limitation of the classifier must be taken into account when interpreting the results.

Which features are most suited to base the river ice classification on during breakup season? Why do some features perform better than others?
Co-pol (intensity) and GLCM mean (texture) features showed the best separability between sheet ice, ice jams and open water. GLCM mean was the most important feature for Sentinel-1 and RADARSAT-2 and might also become the most important feature for RCM, if spatial resolution differences are accounted for. The main advantage of GLCM mean is the accurate discrimination of ice cover types associated with low texture, such as water, border ice and sheet ice under melting conditions. Another great advantage of GLCM mean is the reduced sensitivity to speckle. Even though speckle was greatly reduced in intensity SAR images due to extensive preprocessing, still pixels were misclassified in the 'Int' classifiers due to grey level variations between adjacent resolution cells.

The third class of features that were studied are polarimetric features. Even though these features did not show the best separability between the ice stages, they are of great added value. Polarimetric features provide information on the scattering mechanisms and might help indicate the start and development of the breakup season.

The strengths and weaknesses of each feature were studied. No individual feature was able to accurately discriminate between the ice stages during breakup. The features should be combined to get an optimal classification.

How does river ice classification improve when polarimetric and texture features are included in a Random Forest model compared to a basic backscatter intensity classification approach?
RF classification accuracies improved significantly with the inclusion of polarimetric and texture features. Table 5.2 shows that 'IntPolTex' classifiers for Sentinel-1, RADARSAT-2 and RCM have an increased overall accuracy of 3.3%, 3.6% and 7.0% respectively, compared to 'Int' classifiers. Even higher accuracies are expected for RCM, when the RF classification could be performed on SLC data.

For Sentinel-1 the majority of the confusion between classes was due to similarities in backscatter signatures between open water and sheet ice under melting conditions. For RADARSAT-2 and RCM, sheet ice was misclassified as ice jams as a result of volume scattering. Moreover, many pixels acquired under small incidence angles could not be classified correctly. These confusions were still present in the 'IntPolTex' classifications, but to a much lesser extent.

A combination of different features shows greater potentials for river ice classification than a classifier based on intensity features alone. However, even when 'IntPolTex' features are used, a maximum accuracy of around 90% is reached.

What are the potentials and limitations of Sentinel-1, RADARSAT-2 and RADARSAT Constellation Mission on river ice type classification during breakup season?
By including intensity, polarimetric and texture features in a RF classifier, high overall classification accuracies were obtained. The main potentials and limitations for the three satellites are discussed separately.

The further development of a Sentinel-1 classifier is confined. Ice jams can easily be detected, but due to the limited feature possibilities of the dual-pol satellite, a further improvement in classification between sheet ice and open water is very hard.

In RADARSAT-2 the feature possibilities are much more extensive. The quad-pol data offers plenty of polarimetric features that can be studied further. However, not all SAR images are useful, due to incidence angles under 30°. This significantly reduces the amount of data available.

The amount of RCM data was also a big limitation. Both the quality and quantity of RCM data proved to be a limitation. First of all, the recent launch of the satellite mission limited the amount of data, which meant only one breakup season was imaged. Secondly, the absence of single look complex data meant only a small number of features could be computed. Finally, only moderate and low resolution data were available. These are all issues that could be overcome in later studies. RCM is not fully explored in this study, but shows great potential in river ice classification.

In general, SAR data showed great potential for the classification of ice jams. Sometimes sheet ice at the beginning of the breakup season was mislabeled as an ice jam. Upon further studying the scattering mechanisms, this problem might be solved. When the breakup season evolves and temperatures increase, sheet ice and open water look very similar in SAR images, especially when incidence angles are small. This will remain a substantial limitation.

7.2. REVISED HYPOTHESIS

In Section 2.5.3 hypotheses were given about the expected feature values per ice stage (see Figure 2.16). The majority of the hypothesized feature values for the ice jam and open water stages coincides with the measured pixel values of the sample areas. However, often sheet ice pixels showed a different result than was hypothesised. During the research, it was found that there is a large variability in sheet ice pixels. Sheet ice pixels range from mid-winter, where the sheet ice pixels are almost comparable to ice jams due to high backscatter, to sheet ice under melting conditions, where the pixels are difficult to distinguish from open water. The hypothesis matrix presented in Figure 2.16 could be improved by subdividing sheet ice in different classes, such as sheet ice in winter conditions, sheet ice covered by snow and sheet ice under melting conditions.

Even though the backscatter of a sheet ice pixel can be very high (-7 dB, before breakup) or very low (-20 dB, under melting conditions) for co-pol channels, this study showed that there are features that could help to classify the pixels correctly. Polarimetric decomposition shows that the ratio surface to volume scattering is higher for ice jams than for sheet ice. GLCM texture features showed larger values for sheet covered by a wet layer than for open water pixels. The inclusion of these features is recommended to improve river ice classification during breakup.

8

RECOMMENDATIONS

Now that the potentials and limitations of SAR data for river ice classification are understood, recommendations for further development are discussed. In this study, all classifications were performed using single SAR images. However, when temporal changes between these images are taken into account, a better classification might be possible. This is discussed in Section 8.1. In Section 8.2 recommendations are given on the development of a year-round classifier, that could identify ice jams during freeze-up and breakup season. Finally, an outlook on the creation of a breakup forecasting system is given in Section 8.3, that is able to predict the course of a breakup.

8.1. USING TEMPORAL PATTERNS AND EXPERT KNOWLEDGE FOR TRACKING

Confusion between open water and sheet ice under melting conditions is a large source of uncertainty for the ice classification, because both classes have comparable feature values. Temporal patterns could help improve the classification accuracies.

One could imagine that a region with pixels that are labeled as sheet ice, cannot be all changed into open water in a few days. The ice cover deterioration normally starts with melt and cracks in the ice cover. In the presented temporal and spatial plots it was shown that the breakup process takes some time. When pixels are classified as open water, there is a probability that a layer of melted snow or ice is covering the ice layer, resulting in a low backscattered signal.

Time series modeling could overcome this confusion. This is also recommended by van der Sanden et al. (2020). They propose to monitor the backscatter intensity of the ice cover for sample areas to evaluate the progress of the breakup. For further research, it is recommended to further study the temporal breakup patterns and use this expert knowledge for river ice classification improvements.

8.2. TOWARDS YEAR-ROUND ICE CLASSIFICATION

Currently, expert knowledge is required to indicate the start of the breakup season. To determine the onset of ice breakup from a time series, other methods (e.g. visual image inspection, change detection or thresholding) are needed. From the moment that snow starts to melt, the breakup classifier developed in this study can be used to monitor the river ice development. It would be ideal to have a year-round classifier that can monitor ice development permanently and detect ice jams during all stages of the river ice formation and deterioration.

Other studies like Jasek et al. (2013) and Das et al. (2015) used SAR data to monitor ice cover formation during freeze-up. Rivers like the Peace River, also located in Alberta, are prone to ice jams in both freeze-up and breakup season. For these types of rivers, it would be especially beneficial for monitoring purposes to have access to a year-round river ice classifier.

An in-depth understanding of the behaviour of intensity, texture and polarimetric feature during freeze-up, winter and breakup season should make it possible to develop such a year-round automatic classification

approach. The ratio between surface and volume scattering might provide a concrete starting point to deal with the transition from freeze-up to winter conditions and breakup season.

8.3. FORECASTING ICE JAMS DURING RIVER ICE BREAKUP

New and exciting opportunities exist to advance our current stage of river ice monitoring to river ice forecasting, which can help to improve ice jam risk management. Since we are better capable of classifying the river ice during breakup, also predictions about the future could be made to help better anticipate river ice jams.

Several levels of information should be integrated in order to make accurate predictions. First of all, hydrometeorological patterns that are associated with dynamic breakup should be gathered. Second, the river morphology should be studied, to understand the channel's predisposition to ice jams. Lastly, this study could be used to monitor the maturity of the ice cover. When the meteorological predictions and ice cover maturity data are combined with geospatial data, a warning could be issued when an ice jam event is predicted in a risk area.

Recently, two studies were published that also discuss the need of a river ice forecasting system. First of all, Lindenschmidt et al. (2019) discuss the necessary steps to develop an ice jam forecasting system for the Lower Oder River, a large river located in Central-Europe. In the Lower Oder River, ice jams may occur during freeze-up and breakup phases. Lindenschmidt et al. (2019) propose to develop an empirical and geospatial model to estimate the predisposition of river reaches to certain ice types. Moreover, they propose to develop a deterministic model which includes remote sensing observations. Secondly, a system named *DAVE* is under development, which should improve ice jam risk management across Canada (Gauthier et al., 2020). Gauthier et al. (2020) integrate three levels of information that were also mentioned in this section: hydrometeorological patterns, the current maturity of an ice cover and the predisposition of a river to ice jams.

A

REFERENCE DATA

A.1. OBSERVATION FLIGHTS AEP

Table A.1: Ice classification per date Athabasca River 2019, by Alberta Environment and Parks. During breakup season, AEP conducts helicopter flights almost daily. From the georeferenced photos that are created during the flights, different ice classes are identified.

Date	Ice Classification (AEP Observation Flight)
04-06-2019	290 km - 352 km: Intact ice cover 352 km - 360 km: Intermittent ice cover 360 km - 367 km: Intact ice cover 367 km - 368 km: Open water 368 km - 392 km: Intact ice cover 392 km - 393 km: Open water 393 km - 395 km: Intact ice cover 395 km - 396 km: Open water 396 km - 425 km: Intact ice cover 425 km - 427 km: Intermittent ice cover 427 km - 445 km: Intact ice cover
04-08-2019	290 km - 341 km: Intact ice cover 341 km - 346 km: Intermittent ice cover 346 km - 350 km: Ice jam 350 km - 375 km: Open water 375 km - 404 km: Intermittent ice cover 404 km - 415 km: Intact ice cover 415 km - 423 km: Open water 423 km - 431 km: Intermittent ice cover 431 km - 441 km: Ice run 441 km - 445 km: Open water
04-09-2019	285 km - 290 km: Intermittent ice cover 290 km - 330 km: Intact ice cover 330 km - 346 km: Ice jam 346 km - 445 km: Open water
04-10-2019	285 km - 292 km: Intermittent ice cover 292 km - 330 km: Intact ice cover 330 km - 347 km: Ice jam 347 km - 361 km: Open water 361 km - 380 km: Ice run 380 km - 445 km: Open water

Table A.1 continued from previous page

04-11-2019	285 km - 292 km: Intermittent ice cover 292 km - 330 km: Intact ice cover 330 km - 349 km: Ice jam 349 km - 445 km: Open water
04-12-2019	285 km - 290 km: Intermitent ice cover 290 km - 297 km: Intact ice cover 297 km - 302 km: Intermittent ice cover 302 km - 307 km: Intact ice cover 307 km - 342 km: Ice run 342 km - 445 km: Open water
04-14-2019	285 km - 290 km: Open water 290 km - 296 km: Intact ice cover 296 km - 304 km: Intermittent ice cover 304 km - 307 km: Intact ice cover 307 km - 322 km: Ice jam 322 km - 345 km: Open water
04-15-2019	285 km - 290 km: Open water 290 km - 296 km: Intact ice cover 296 km - 304 km: Intermittent ice cover 304 km - 307 km: Intact ice cover 307 km - 320 km: Ice jam 320 km - 330 km: Open water
04-16-2019	285 km - 290 km: Open water 290 km - 296 km: Intact ice cover 296 km - 304 km: Inttermittent ice cover 304 km - 307 km: Intact ice cover 307 km - 319 km: Ice jam 319 km - 330 km: Open water
04-17-2019	285 km - 290 km: Open water 290 km - 296 km: Intact ice cover 296 km - 304 km: Intermittent ice cover 304 km - 307 km: Intact ice cover 307 km - 317 km: Ice jam 317 km - 330 km: Open water
04-19-2019	285 km - 290 km: Open water 290 km - 292 km: Intact ice cover 292 km - 304 km: Intermittent ice cover 304 km - 307 km: Intact ice cover 307 km - 311 km: Ice jam 311 km - 445 km: Open water
04-20-2019	285 km - 290 km: Open water 290 km - 304 km: Intermittent ice cover 304 km - 307 km: Intact ice cover 307 km - 445 km: Open water
04-21-2019	285 km - 292 km: Open water 292 km - 293 km: Intermittent ice cover 293 km - 296 km: Ice jam 296 km - 445 km: Open water
04-22-2019	285 km - 445 km: Open water

Table A.2: Ice classification per date Athabasca River 2020, by Alberta Environment and Parks. During breakup season, AEP conducts helicopter flights almost daily. From the georeferenced photos that are created during the flights, different ice classes are identified.

Date	Ice Classification (AEP Observation Flight)
04-21-2020	285 km - 422 km: Intact ice cover 422 km - 428 km: Intermittent ice cover 428 km - 445 km: Intact ice cover
04-23-2020	285 km - 352 km: Intact ice cover 352 km - 355 km: Intermittent ice cover 355 km - 422 km: Intact ice cover 422 km - 428 km: Intermittent ice cover 428 km - 445 km: Intact ice cover
04-24-2020 (n1)	285 km - 327 km: Intact ice cover 327 km - 380 km: Ice run 380 km - 442 km: Open water
04-24-2020 (n2)	285 km - 308 km: Intact ice cover 308 km - 329 km: Ice jam 329 km - 442 km: Open water
04-25-2020	285 km - 290 km: Intermittent ice cover 290 km - 325 km: Intact ice cover 325 km - 345 km: Ice jam 345 km - 384 km: Open water
04-26-2020	285 km - 305 km: Ice jam 305 km - 316 km: Ice run 316 km - 322 km: Open water
04-27-2020	285 km - 305 km: Ice jam 305 km - 310 km: Open water
04-28-2020	285 km - 303 km: Ice jam 303 km - 445 km: Open water
04-29-2020 (n1)	285 km - 296 km: Ice jam 296 km - 305 km: Open water
04-29-2020 (n2)	285 km - 294 km: Ice jam 294 km - 297 km: Open water
04-30-2029	285 km - 290.5 km: Ice jam 290.5 km - 445 km: Open water
05-01-2020	285 km - 445 km: Open water
05-02-2020	285 km - 445 km: Open water

A.2. OPTICAL IMAGERY SENTINEL-2

Table A.3: Sentinel-2 data products that were used for reference in this study (breakup seasons 2018-2019).

ID	Local date	Local time	Comments
S2-AR19-1	1-Mar-2019	12:53:11	Not used (clouds)
S2-AR19-2	3-Mar-2019	12:42:59	Used
S2-AR19-3	5-Mar-2019	12:52:02	Not used (clouds)
S2-AR19-4	6-Mar-2019	12:52:39	Used
S2-AR19-5	8-Mar-2019	12:52:01	Not used (clouds)
S2-AR19-6	10-Mar-2019	12:42:02	Not used (clouds)
S2-AR19-7	11-Mar-2019	12:52:01	Not used (clouds)
S2-AR19-8	13-Mar-2019	12:41:39	Used
S2-AR19-9	16-Mar-2019	12:51:29	Used
S2-AR19-10	18-Mar-2019	12:41:01	Not used (clouds)
S2-AR19-11	21-Mar-2019	12:50:51	Used
S2-AR19-12	23-Mar-2019	12:40:39	Not used (clouds)
S2-AR19-13	26-Mar-2019	12:50:19	Not used (clouds)
S2-AR19-14	28-Mar-2019	12:40:31	Not used (clouds)
S2-AR19-15	30-Mar-2019	12:52:02	Not used (clouds)
S2-AR19-16	2-Apr-2019	12:39:29	Not used (clouds)
S2-AR19-17	5-Apr-2019	12:49:19	Not used (clouds)
S2-AR19-18	7-Apr-2019	12:39:21	Not used (clouds)
S2-AR19-19	9-Apr-2019	12:49:21	Used
S2-AR19-20	10-Apr-2019	12:49:01	Not used (clouds)
S2-AR19-21	12-Apr-2019	12:39:29	Used
S2-AR19-22	14-Apr-2019	12:48:02	Not used (clouds)
S2-AR19-23	15-Apr-2019	12:49:19	Used
S2-AR19-24	17-Apr-2019	12:39:21	Not used (clouds)
S2-AR19-25	19-Apr-2019	12:48:49	Not used (clouds)
S2-AR19-26	20-Apr-2019	12:49:21	Not used (clouds)
S2-AR19-27	22-Apr-2019	12:39:29	Not used (clouds)
S2-AR19-28	24-Apr-2019	12:49:21	Not used (clouds)
S2-AR19-29	25-Apr-2019	12:49:29	Not used (clouds)
S2-AR19-30	27-Apr-2019	12:39:21	Used
S2-AR19-31	29-Apr-2019	12:47:48	Not used (clouds)
S2-AR19-32	30-Apr-2019	12:49:21	Not used (clouds)
S2-AR19-33	2-May-2019	12:39:29	Not used (clouds)
S2-AR19-34	4-May-2019	12:39:21	Not used (clouds)
S2-AR19-35	5-May-2019	12:49:29	Not used (clouds)

Table A.4: Sentinel-2 data products that were used for reference in this study (breakup seasons 2019-2020).

ID	Local date	Local time	Comments
S2-AR20-1	2-Mar-2020	12:42:51	Not used (clouds)
S2-AR20-2	5-Mar-2020	12:54:41	Not used (clouds)
S2-AR20-3	7-Mar-2020	12:45:19	Not used (clouds)
S2-AR20-4	10-Mar-2020	12:51:09	Not used (clouds)
S2-AR20-5	12-Mar-2020	12:41:41	Not used (clouds)
S2-AR20-6	15-Mar-2020	12:52:01	Not used (clouds)
S2-AR20-7	17-Mar-2020	12:40:09	Not used (clouds)
S2-AR20-8	20-Mar-2020	12:49:59	Used
S2-AR20-9	22-Mar-2020	12:40:31	Used
S2-AR20-10	25-Mar-2020	12:40:11	Not used (clouds)
S2-AR20-11	27-Mar-2020	12:39:29	Not used (clouds)
S2-AR20-12	29-Mar-2020	12:49:29	Not used (clouds)
S2-AR20-13	1-Apr-2020	12:39:21	Not used (clouds)
S2-AR20-14	4-Apr-2020	12:49:11	Used
S2-AR20-15	6-Apr-2020	12:39:19	Not used (clouds)
S2-AR20-16	9-Apr-2020	12:49:19	Not used (clouds)
S2-AR20-17	11-Apr-2020	12:39:21	Not used (clouds)
S2-AR20-18	14-Apr-2020	12:49:21	Used
S2-AR20-19	16-Apr-2020	12:39:29	Used
S2-AR20-20	19-Apr-2020	12:49:09	Not used (clouds)
S2-AR20-21	21-Apr-2020	12:39:21	Not used (clouds)
S2-AR20-22	24-Apr-2020	12:49:21	Not used (clouds)
S2-AR20-23	26-Apr-2020	12:39:19	Not used (clouds)
S2-AR20-24	29-Apr-2020	12:49:19	Used
S2-AR20-25	1-May-2020	12:39:21	Not used (clouds)
S2-AR20-26	4-May-2020	12:49:21	Used
S2-AR20-27	5-May-2020	12:39:19	Used

B

PREPROCESSING OF SAR IMAGES IN SNAP

This appendix consists of three sections that discuss the SNAP configurations that were used in this study. In Section B.1 the selection of the speckle filter is justified. Next, the used settings to obtain the decomposition parameters are discussed in Section B.2. Finally, in Section B.3 the SNAP configurations to calculate the GLCM texture features are presented.

B.1. SPECKLE FILTERING

This appendix consists of an pre-study which was done to find the appropriate preprocessing steps of the SAR images. A variation of preprocessing steps was conducted in SNAP to come to the used preprocessing scheme as was presented in Figure 4.2. Some steps are always required in a preprocessing scheme: reading the file, calibration, terrain correction and writing to an output folder. Other steps are desired, like applying an orbit file, masking to an area of interest and converting the linear dimensionless backscatter to dB-scaled values. However, steps as multilooking an speckle filtering are not always implemented and are dependent on the desired research goal.

Before applying the preprocessing scheme to the Athabasca River, an experiment was conducted with the different schemes on an area with tropical forest located in Guyana. This area is very well suited for preprocessing tests, as the pixel fluctuations are assumed to be due to speckle. The Equivalent Number of Looks (ENL) was computed for a few polygons that covered a dense and even forest. In literature, the ENL is used to assess the amount of speckle in SAR images, it is generally computed as:

$$ENL = \frac{\mu^2}{\sigma^2} \tag{B.1}$$

μ and σ respectively represent the mean and standard deviation of a homogeneous area. The larger value of the ENL, the better performance of speckle suppression. However, a trade-off is made, as speckle filtering also reduces the spatial resolution. A value of 10 for the ENL is desired, as this results in a balances trade-off between noise and resolution.

Speckle filtering is not an exact science, but is image and target dependent. An ideal speckle filter will do several things, according to Lee et al. (1994):

- Reduce speckle;
- Preserve edge sharpness;
- Preserve line and point target contrast;
- Retain mean values in homogeneous regions;
- Retain texture information.

SNAP offers a range of Speckle filters. The filters were compared based on the above mentioned requirements and on the acquired ENL after filtering. In Figure B.1 a part of the Athabasca River at 12 March 2019 is shown. In this part of the river a cracks in the ice cover are visible. After several experiments, the Gamma Map filter and Refined Lee filter (with window size 3 x 3) were two options that reached an ENL around 10 after only one time of speckle filtering.

After a visual inspection over the Athabasca River it can be concluded that differences between the filters are small. However, the Refined Lee filter makes the river look slightly less homogeneous than the Gamma Map filter does. Even though the differences are limited, for classification purposes the Gamma Map filter shows more promising results.

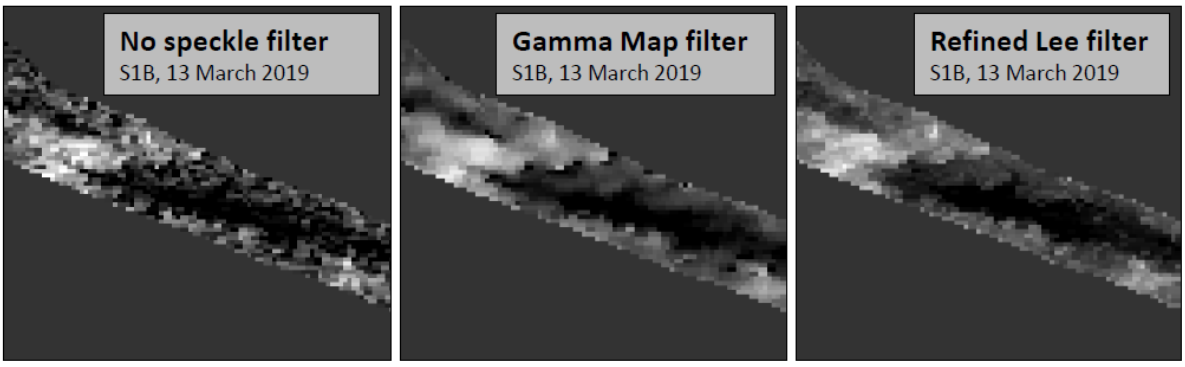

Figure B.1: Detailed comparison of two Sentinel 1 speckle filters (Gamma Map and Refined Lee). The left image [A] shows the S1 SAR image before speckle filtering, images [B] and [C] present to different Speckle filters, the Gamma Map and Refined Lee filter respectively. The Gamma Map filter shows more homogeneous patches than the Refined Lee filter and is therefore preferred.

Figure B.2 shows the used configurations for speckle filtering in SNAP. In the figure the speckle filter for quad-pol (RADARSAT-2) data is presented. SNAP also has a dual-pol and a compact-pol speckle filter, that were used for Sentinel-1 and RCM respectively.

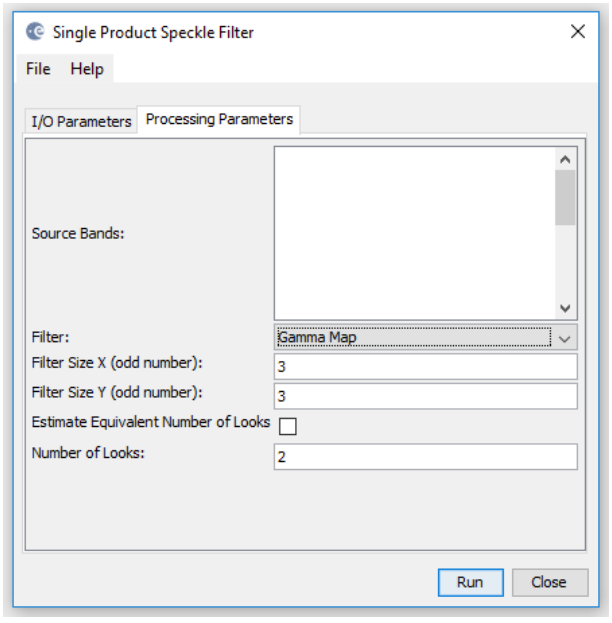

Figure B.2: Selected configurations in SNAP to speckle filter SAR images.

B.2. EIGENVALUE DECOMPOSITION FEATURES

In SNAP under the polarimetric menu multiple *polarimetric decomposition* methods can be selected. In this study the popular H-A-α decomposition was used, which provide information about the scattering mechanisms from a target. The H-A-α decomposition method can be computed for dual-, quad- and compact-pol. As input the coherency matrix T is required and a desired window size. After some test, a window size of 7x7 was found to be optimal. The used SNAP configurations can be found in Figure B.3.

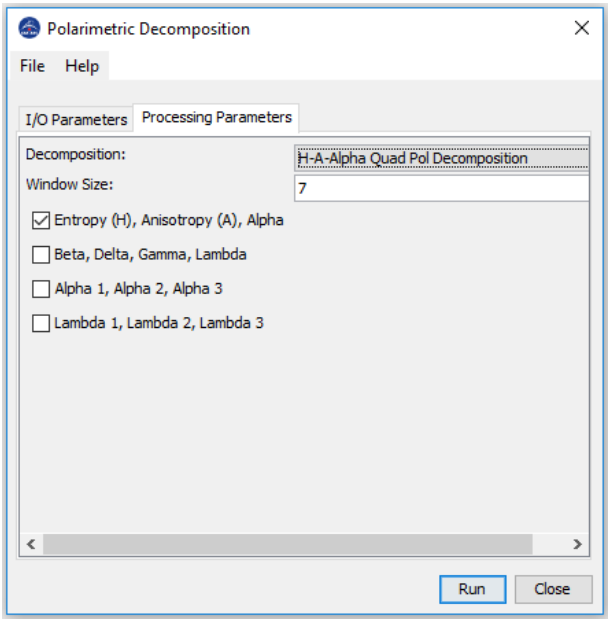

Figure B.3: Selected configurations in SNAP to compute decomposition parameters H, A and α.

B.3. TEXTURE FEATURES

Under the *image analysis* menu in SNAP, the option to analyse GLCM texture can be found. Several parameters can be adjusted when computing the GLCM texture features: (1) quantizer, (2) quantization levels, (3) displacement, (4) window size and (5) angle, see Figure B.4.

Two options are available for the *quantizer*, the probabilistic and the equal distance quantizer. The equal distance quantizer expresses the GLCM in total number of occurrences (see example in Figure 2.17 [D]). In this study, the probabilistic quantizer was preferred, which expresses the GLCM as probabilities (see example in Figure 2.17 [E]). *Quantization levels* are the number of possible values that the final image will have. In the example in Figure 2.17 2^2 values were used. In this study more values will used, namely 2^{16} different values. A larger number was used to prevent information from getting lost. Some experiments were conducted to find the optimal displacement value and window size. The best results were obtained with a *displacement value* of 2 and a *window size* of 11x11. The GLCM was computed in all directions, so instead of only computing the GLCM east matrix as was done in Figure 2.17, four *angles* (0°, 45°, 90° and 135°) were computed in this study.

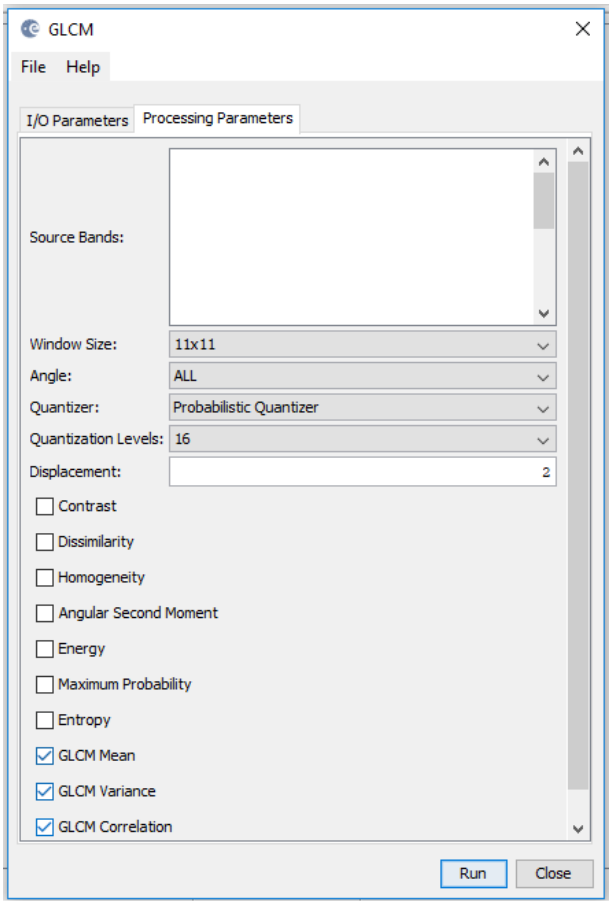

Figure B.4: Selected configurations in SNAP to compute GLCM features.

C

COMPARISON OF MACHINE LEARNING TECHNIQUES

For the S1-IntPolTex, R2-IntPolTex and RCM-IntPolTex validation data sets six supervised machine learning algorithms were tested. Among these classifiers are:

- Random Forest - **RF**
- K-Nearest Neighbours - **K-NN**
- Support Vector Machines - **SVM**
- Naive Bayes - **NB**
- Linear Discriminant Analysis - **LDA**
- Logistic Regression - **LR**

The results can be found in Tables C.1, C.2 and C.3. Highest accuracies were obtained with the Random Forest classier, which was also the used classifier in this study.

Table C.1: Statistical metrics of different supervised machine learning classifications based on Sentinel-1 data (S1-IntPolTex).

	RF	**K-NN**	**SCM**	**NB**	**LDA**	**LR**
Overall Accuracy	0.856	0.843	0.856	0.850	0.804	0.840
Cohen's Kappa	0.784	0.765	0.799	0.775	0.706	0.759

Table C.2: Statistical metrics of different supervised machine learning classifications based on RADARSAT-2 data (R2-IntPolTex).

	RF	**K-NN**	**SCM**	**NB**	**LDA**	**LR**
Overall Accuracy	0.912	0.903	0.909	0.902	0.887	0.867
Cohen's Kappa	0.867	0.855	0.863	0.853	0.831	0.801

Table C.3: Statistical metrics of different supervised machine learning classifications based on RCM data (RCM-IntPolTex).

	RF	**K-NN**	**SCM**	**NB**	**LDA**	**LR**
Overall Accuracy	0.910	0.891	0.894	0.899	0.871	0.896
Cohen's Kappa	0.865	0.836	0.841	0.848	0.806	0.844

D

RANDOM FOREST OPTIMIZATION

The Random Forest model that was built in Python can be optimized using several *skikit-learn's* packages. In order to optimize the RF models to obtain the most accurate predictions, hyperparameters should be adjusted. Section 4.5.3 provided more information on the used hyperparameters in this study.

For each satellite mission the performance of multiple hyperparameter values was evaluated in different validation curves.

Number of estimators
The validation curves for *n_estimators* were created with values ranging from 1 to 100. Graphs [A] in Figures D.1, D.2 and D.3 show that the best value for the number of estimators appeared to be 46 for Sentinel-1, 4 for RADARSAT-2 and 16 for RCM. It is important to note that the models showed very high accuracies, regardless of the number of estimators used.

Max depth
Graphs [B] in Figures D.1, D.2 and D.3 show that the maximum depth for the models varied between 5 and 15. When looking at the training score, it seems better to choose a higher value for *max_depth*. However, this is not recommended, since it might lead to overfitting of the training data.

Minimum sample split
Graphs [C] in Figures D.1, D.2 and D.3 show the selected values for the minimum samples split. It makes sense to select a low value for *min_samples_split*, since higher values constrain the model, because more samples have to be considered at each note. When higher values are selected, the RF model is suffering from underfitting, since the model cannot learn enough from the data.

Minimum sample leaf
Graphs [D] in Figures D.1, D.2 and D.3 show that the desired value for *min_samples_leaf* equaled 1 for all models. When this value increases, the decision trees may to be capable to make enough split to capture sufficient variation in the training data.

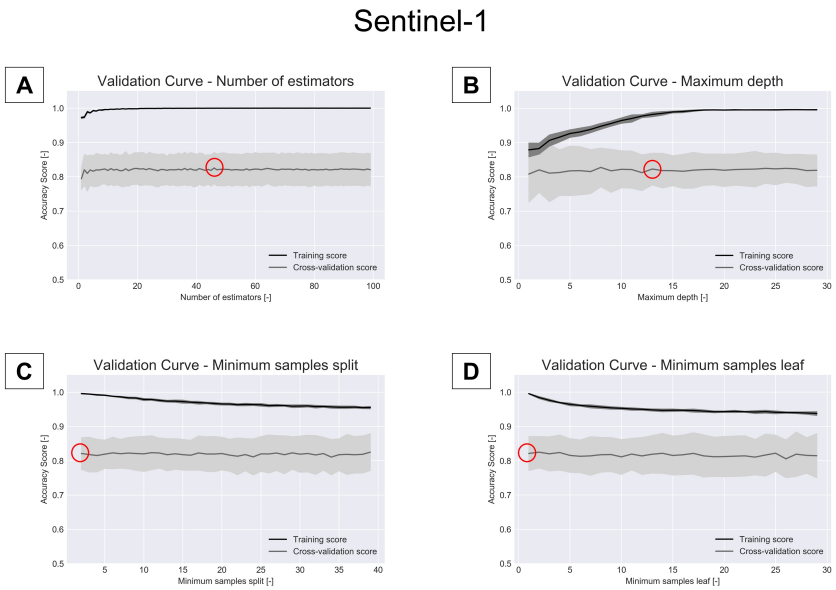

Figure D.1: Hyperparameter optimization of Random Forest classifier for Sentinel-1. The red circles in each of the validation curves show the optimal value for the number of estimators, the maximum depth, the minimum samples split and minimum samples leaf.

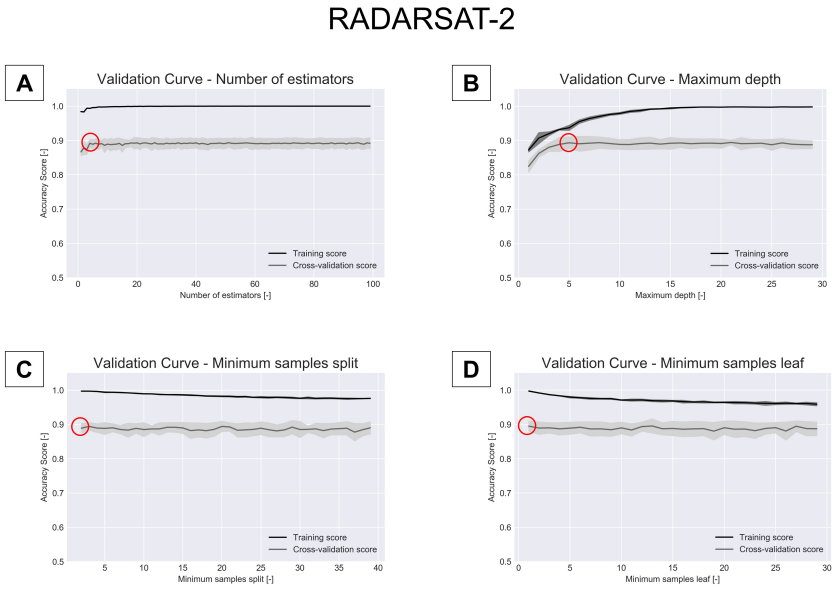

Figure D.2: Hyperparameter optimization of Random Forest classifier for RADARSAT-2. The red circles in each of the validation curves show the optimal value for the number of estimators, the maximum depth, the minimum samples split and minimum samples leaf.

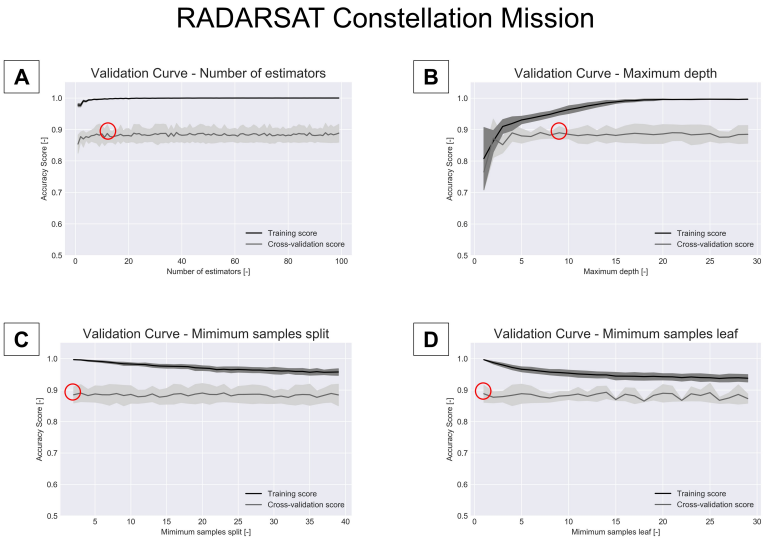

Figure D.3: Hyperparameter optimization of Random Forest classifier for RCM. The red circles in each of the validation curves show the optimal value for the number of estimators, the maximum depth, the minimum samples split and minimum samples leaf.

E

ADDITIONAL CLASSIFICATION MAPS

Besides studying the classification results of the individual sample areas that were presented in Chapter 5, the classification maps of the entire river section provide useful insights into the strengths and weaknesses of the developed classifiers. However, it should be noted that the data was not compared to ground truth data. In Figures E.1, E.2 and E.3 the median pixel value for each kilometer was selected to show the classification results of the 'Int' and 'IntPolTex' Random Forest classifiers.

These figures give a slightly different picture compared to the accuracy values that are presented in Table 5.2, because early in the season a large number of pixels are misclassified as ice jams instead of sheet ice. In the case of the sample areas classification, sample locations were mostly selected in areas in which the thermal deterioration had started. In Figures E.1, E.2 and E.3 the entire river section present on a SAR image is shown, so also parts of the river that were still in winter conditions.

Based on a Sentinel-1 image acquired at 10 June 2020 areas with rapids are extracted. The analyzed stretch of the Athabasca River knows many rapids, resulting in an increased backscatter when the stretch is free of ice. These areas are often misclassified as sheet ice or ice jams instead of water, due to the rough surface. The grey boxes in Figures E.1, E.2 and E.3 indicate the locations of the rapids.

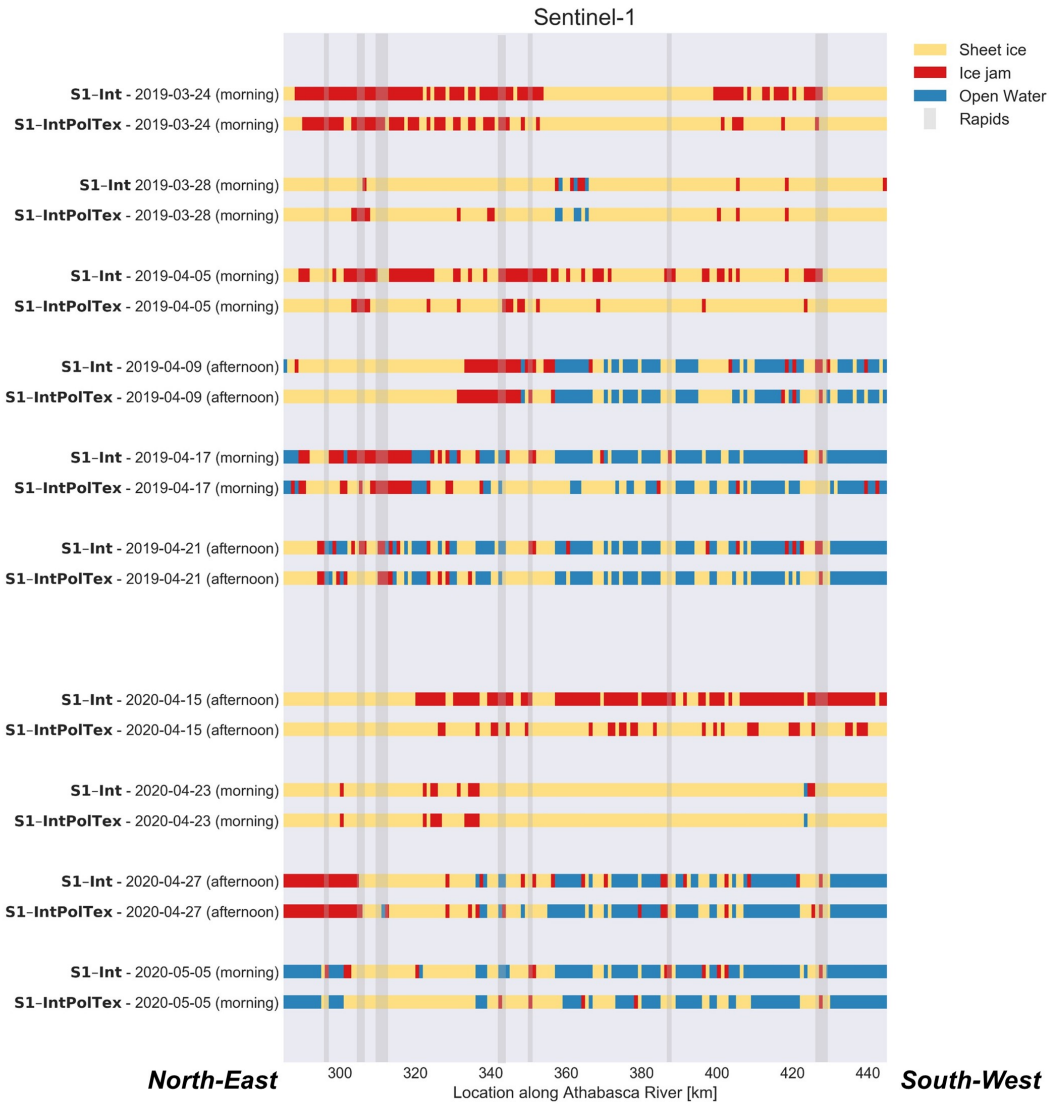

Figure E.1: Classification based on S1-Int and S1-IntPolTex data. The exact ice stages of the entire river are not completely known. However, based on general knowledge on the breakup process, it can be seen that large parts of the river are misclassified as ice jams early in the season.

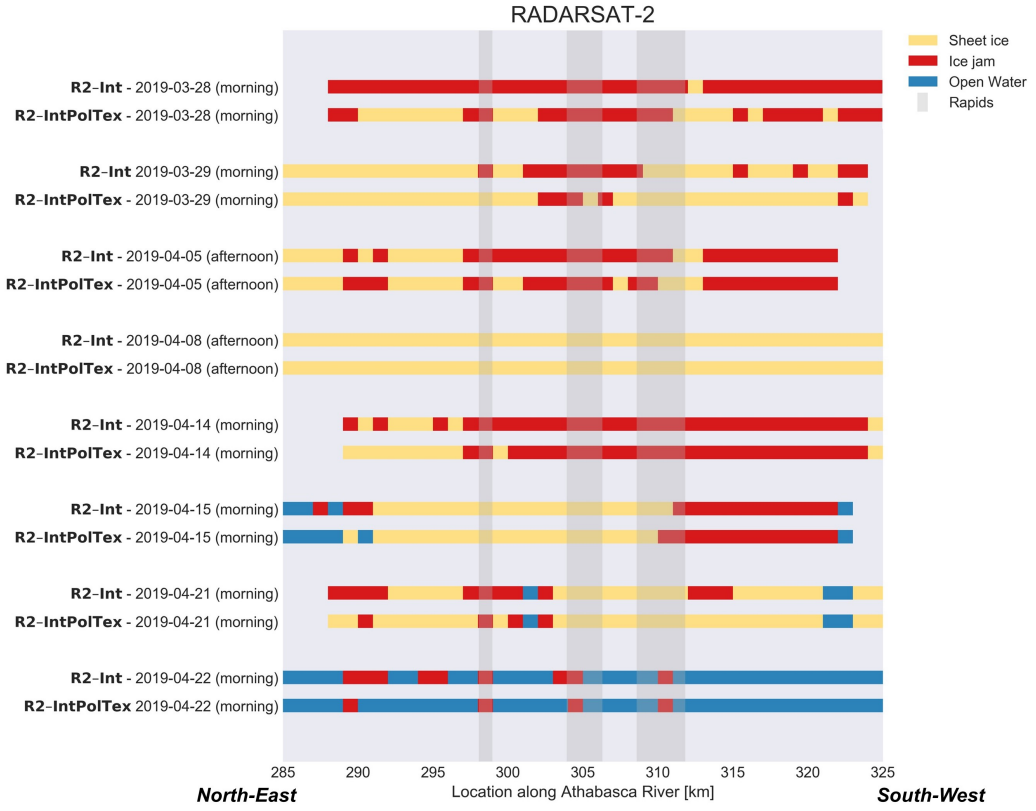

Figure E.2: Classification based on R2-Int and R2-IntPolTex data. Often R2-Int incorrectly classifies pixels as ice jams. To a lesser extent, this is also a problem for R2-IntPolTex.

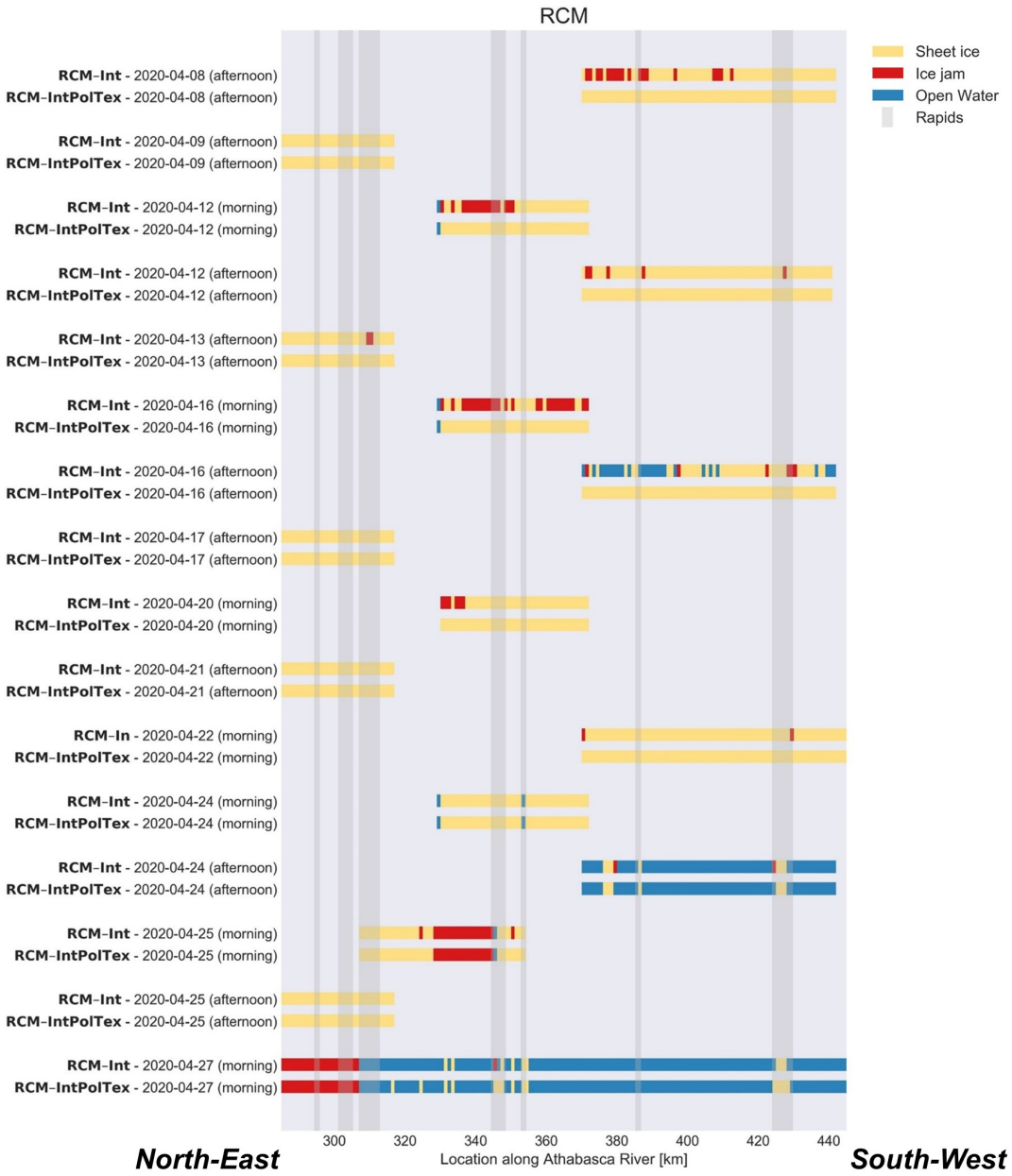

Figure E.3: Classification based on RCM-Int and RCM-IntPolTex data. RCM-IntPolTex is better able to detect sheet ice under melting conditions, as can be seen on 16 April 2020 (afternoon).

BIBLIOGRAPHY

Ainsworth, T., Schuler, D., and Lee, J.-S. (2008). Polarimetric SAR characterization of man-made structures in urban areas using normalized circular-pol correlation coefficients. *Remote Sensing of Environment*, 112(6):2876–2885.

Alberta Environment (2010). Facts about water in Alberta.

Andres, D. and Doyle, P. (1984). Analysis of breakup and ice jams on the Athabasca River at Fort McMurray, Alberta. *Canadian Journal of Civil Engineering*, 11(3):444–458.

Ashton, G. D. (1986). *River and lake ice engineering*. Water Resources Publication.

Barber, D. and LeDrew, E. (1991). SAR sea ice discrimination using texture statistics- A multivariate approach. *Photogrammetric Engineering and Remote Sensing*, 57(4):385–395.

Beltaos, S. and Prowse, T. (2009). River-ice hydrology in a shrinking cryosphere. *Hydrological Processes: An International Journal*, 23(1):122–144.

Beltaos, S. and Prowse, T. D. (2001). Climate impacts on extreme ice-jam events in Canadian rivers. *Hydrological Sciences Journal*, 46(1):157–181.

Benson, A. S. and DeGloria, S. D. (1985). Interpretation of Landsat-4 thematic mapper and multispectral scanner data for forest surveys. *Photogrammetric Engineering and Remote Sensing*, 51(9):1281–1289.

Bilello, M. A. (1980). *Maximum thickness and subsequent decay of lake, river, and fast sea ice in Canada and Alaska*, volume 80. US Army, Corps of Engineers, Cold Regions Research and Engineering Laboratory.

Bishop, C. M. (2006). *Pattern recognition and machine learning*. Springer.

Bishop, Y. M., Fienberg, S. E., and Holland, P. W. (2007). *Discrete multivariate analysis: Theory and practice*. Springer Science & Business Media.

Boularbah, S., Ouarzeddine, M., and Belhadj-Aissa, A. (2012). Investigation of the capability of the compact polarimetry mode to reconstruct full polarimetry mode using RADARSAT2 data. *Advanced Electromagnetics*, 1(1):19–28.

Boulze, H., Korosov, A., and Brajard, J. (2020). Classification of sea ice types in Sentinel-1 SAR data using convolutional neural networks. *Remote Sensing*, 12(13):2165.

Breiman, L. (2001). Random Forests. *Machine learning*, 45(1):5–32.

Brown, R. S., Hubert, W. A., and Daly, S. F. (2011). A primer on winter, ice, and fish: what fisheries biologists should know about winter ice processes and stream-dwelling fish. *Fisheries*, 36(1):8–26.

Buderi, R. (1996). *The invention that changed the world: How a small group of radar pioneers won the Second World War and launched a technological revolution*. Simon and Schuster.

Campbell, J. B. and Wynne, R. H. (2011). *Introduction to Remote Sensing*. Guilford Press.

Canada Centre for Remote Sensing (2019). Fundamentals of Remote Sensing. https://www.nrcan.gc.ca/maps-tools-publications/satellite-imagery-air-photos/tutorial-fundamentals-remote-sensing/9309. Accessed on 1 September 2020.

Cawley, G. C. and Talbot, N. L. (2010). On over-fitting in model selection and subsequent selection bias in performance evaluation. *The Journal of Machine Learning Research*, 11:2079–2107.

Chaouch, N., Temimi, M., Romanov, P., Cabrera, R., McKillop, G., and Khanbilvardi, R. (2014). An automated algorithm for river ice monitoring over the Susquehanna River using the MODIS data. *Hydrological Processes*, 28(1):62–73.

Charbonneau, F., Brisco, B., Raney, R., McNairn, H., Liu, C., Vachon, P., Shang, J., DeAbreu, R., Champagne, C., Merzouki, A., et al. (2010). Compact polarimetry overview and applications assessment. *Canadian Journal of Remote Sensing*, 36(sup2):S298–S315.

Chu, T., Das, A., and Lindenschmidt, K.-E. (2015). Monitoring the variation in ice-cover characteristics of the Slave River, Canada using RADARSAT-2 data—A case study. *Remote Sensing*, 7(10):13664–13691.

Chu, T. and Lindenschmidt, K.-E. (2016). Integration of space-borne and air-borne data in monitoring river ice processes in the Slave River, Canada. *Remote Sensing of Environment*, 181:65–81.

Cloude, S. R. and Pottier, E. (1996). A review of target decomposition theorems in radar polarimetry. *IEEE Transactions on Geoscience and Remote Sensing*, 34(2):498–518.

Cloude, S. R. and Pottier, E. (1997). An entropy based classification scheme for land applications of polarimetric SAR. *IEEE Transactions on Geoscience and Remote Sensing*, 35(1):68–78.

Congalton, R. G., Oderwald, R. G., and Mead, R. A. (1983). Assessing Landsat classification accuracy using discrete multivariate analysis statistical techniques. *Photogrammetric engineering and remote sensing*, 49(12):1671–1678.

Cooley, S. W. and Pavelsky, T. M. (2016). Spatial and temporal patterns in Arctic river ice breakup revealed by automated ice detection from MODIS imagery. *Remote Sensing of Environment*, 175:310–322.

Cooper, D. W., Mueller, R. A., and Schertler, R. J. (1976). Remote profiling of lake ice using an S-band short-pulse radar aboard an all-terrain vehicle. *Radio Science*, 11(4):375–381.

Cumming, W. (1952). The dielectric properties of ice and snow at 3.2 centimeters. *Journal of Applied Physics*, 23(7):768–773.

Dabboor, M. and Geldsetzer, T. (2014). Towards sea ice classification using simulated RADARSAT Constellation Mission compact polarimetric SAR imagery. *Remote Sensing of Environment*, 140:189–195.

Dabboor, M., Montpetit, B., and Howell, S. (2018). Assessment of the high resolution SAR mode of the RADARSAT Constellation Mission for first year ice and multiyear ice characterization. *Remote Sensing*, 10(4):594.

Das, A., Sagin, J., van der Sanden, J., Evans, E., McKay, H., and Lindenschmidt, K.-E. (2015). Monitoring the freeze-up and ice cover progression of the Slave River. *Canadian Journal of Civil Engineering*, 42(9):609–621.

Drinkwater, M. R., Kwok, R., Winebrenner, D., and Rignot, E. (1991). Multifrequency polarimetric Synthetic Aperture Radar observations of sea ice. *Journal of Geophysical Research: Oceans*, 96(C11):20679–20698.

Duguay, C. R., Bernier, M., Gauthier, Y., and Kouraev, A. (2015). Remote sensing of lake and river ice. *Remote sensing of the cryosphere*, pages 273–306.

Emery, W. and Camps, A. (2017). *Introduction to satellite remote sensing: atmosphere, ocean, land and cryosphere applications*. Elsevier.

Enderle, D. I. and Weih, R. C. (2005). Integrating supervised and unsupervised classification methods to develop a more accurate land cover classification. *Journal of the Arkansas Academy of Science*, 59(1):65–73.

Eriksson, L., Drinkwater, M., Holt, B., Valjavek, E., and Nortier, O. (1998). SIR-C polarimetric radar results from the Weddell Sea, Antarctica. In *IGARSS'98. Sensing and Managing the Environment. 1998 IEEE International Geoscience and Remote Sensing. Symposium Proceedings.(Cat. No. 98CH36174)*, volume 4, pages 2222–2224. IEEE.

Ettema, R., Muste, M., and Kruger, A. (1999). Ice jams in river confluences. Technical report, Cold Regions Research and Engineering Lab Hanover NH.

Evans, S. (1965). Dielectric properties of ice and snow–a review. *Journal of Glaciology*, 5(42):773–792.

Farr, T. G. (1993). Radar interactions with geologic surfaces. *Guide to Magellan Image Interpretation*, 93:45–56.

Filipponi, F. (2019). Sentinel-1 GRD Preprocessing Workflow. In *Multidisciplinary Digital Publishing Institute Proceedings*, volume 18, page 11.

Flores-Anderson, A. I., Herndon, K. E., Thapa, R. B., and Cherrington, E. (2019). The SAR Handbook: Comprehensive Methodologies for Forest Monitoring and Biomass Estimation.

Floyd, A. L., Prakash, A., Meyer, F. J., Gens, R., and Liljedahl, A. (2014). Using Synthetic Aperture Radar to define spring breakup on the Kuparuk River, northern Alaska. *Arctic*, pages 462–471.

Freeman, A. and Durden, S. L. (1998). A three-component scattering model for polarimetric SAR data. *IEEE Transactions on Geoscience and Remote Sensing*, 36(3):963–973.

Gauthier, Y., Lhissou, R., Plante Lévesque, V., Maadeni, F., Persent, M.-A., Chokmani, K., Thériault, D., Ratsimbazafy, T., Gill-Fortin, J., Tolszczuk-Leclerc, S., Légaré, S., and Dunford, D. (2020). Forecasting river ice jams risk: the DAVE approach. *25th IAHR International Symposium on Ice*.

Gauthier, Y., Tremblay, M., Bernier, M., and Furgal, C. (2010). Adaptation of a radar-based river ice mapping technology to the Nunavik context. *Canadian Journal of Remote Sensing*, 36(sup1):S168–S185.

Gauthier, Y., Weber, F., Savary, S., Jasek, M., Paquet, L.-M., and Bernier, M. (2006). A combined classification scheme to characterise river ice from SAR data. *EARSeL eProceedings*, 5(1):77–88.

Geldsetzer, T., Charbonneau, F., Arkett, M., and Zagon, T. (2015). Ocean wind study using simulated RCM compact-polarimetry SAR. *Canadian Journal of Remote Sensing*, 41(5):418–430.

Geldsetzer, T., Sanden, J. v. d., and Brisco, B. (2010). Monitoring lake ice during spring melt using RADARSAT-2 SAR. *Canadian Journal of Remote Sensing*, 36(sup2):S391–S400.

Gerard, R. (1989). Hydroelectric power development and the ice regime of inland waters: A northern community perspective. Technical report, National Hydrology Research Inst.

Girard, R., Lee, P. F., and James, K. (2002). The RADARSAT-2&3 topographic mission: an overview. In *IEEE International Geoscience and Remote Sensing Symposium*, volume 3, pages 1477–1479. IEEE.

Groenenboom, J. and Snieder, R. (1995). Attenuation, dispersion, and anisotropy by multiple scattering of transmitted waves through distributions of scatterers. *The Journal of the Acoustical Society of America*, 98(6):3482–3492.

Guyon, I., Weston, J., Barnhill, S., and Vapnik, V. (2002). Gene selection for cancer classification using support vector machines. *Machine learning*, 46(1-3):389–422.

Hall, D. and Martinec, J. (1985). Remote sensing of snow and ice. *Principles and Applications of Imaging Radar, edited by FM Henderson and AJ Lewis*, pages 677–703.

Hall-Beyer, M. (2000). GLCM texture: a tutorial. *National Council on Geographic Information and Analysis Remote Sensing Core Curriculum*, 3.

Hallikainen, M. and Ulaby, F. (1986). Dielectric and scattering behaviour of snow at microwave frequencies. In *International geoscience and remote sensing symposium*, pages 87–91.

Hallikainen, M. and Winebrenner, D. P. (1992). The Physical Basis for Sea Ice Remote Sensing. *Microwave remote sensing of sea ice*, 68:29–46.

Hanssen, R. F. (2001). *Radar interferometry: data interpretation and error analysis*, volume 2. Springer Science & Business Media.

Haralick, R. M. and Bryant, W. F. (1976). Documentation of procedures for textural/spatial pattern recognition techniques.

Henderson, F. M. and Lewis, A. J. (1998). *Manual of remote sensing: principles and applications of imaging radar*. Wiley.

Hicks, F. (2009). An overview of river ice problems: CRIPE07 guest editorial.

Hicks, F. (2016). *An introduction to river ice engineering for Civil Engineers and Geoscientists*. CreateSpace Independent Publishing Platform.

Hicks, F. E. (2013). *The weird and wonderful world of river ice*. CPSIA.

Hoekstra, M., Jiang, M., Clausi, D. A., and Duguay, C. (2020). Lake ice-water vlassification of RADARSAT-2 images by integrating IRGS segmentation with pixel-based Random Forest labeling. *Remote Sensing*, 12(9):1425.

Holmes, Q. A., Nuesch, D. R., and Shuchman, R. A. (1984). Textural analysis and real-time classification of sea-ice types using digital SAR data. *IEEE Transactions on Geoscience and Remote Sensing*, (2):113–120.

Howell, S. E., Small, D., Rohner, C., Mahmud, M. S., Yackel, J. J., and Brady, M. (2019). Estimating melt onset over Arctic sea ice from time series multi-sensor Sentinel-1 and RADARSAT-2 backscatter. *Remote Sensing of Environment*, 229:48–59.

Hu, J., Ghamisi, P., and Zhu, X. X. (2018). Feature extraction and selection of Sentinel-1 dual-pol data for global-scale local climate zone classification. *ISPRS International Journal of Geo-Information*, 7(9):379.

Hutchison, T. K. and Hicks, F. (2007). Observations of ice jam release waves on the Athabasca River near Fort McMurray, Alberta. *Canadian Journal of Civil Engineering*, 34(4):473–484.

Hwang, P. A., Perrie, W., and Zhang, B. (2014). Cross-polarization radar backscattering from the ocean surface and its dependence on wind velocity. *IEEE Geoscience and Remote Sensing Letters*, 11(12):2188–2192.

Imhoff, M. L. (1995). A theoretical analysis of the effect of forest structure on Synthetic Aperture Radar backscatter and the remote sensing of biomass. *IEEE Transactions on Geoscience and Remote Sensing*, 33(2):341–351.

Insurance Bureau Canada (2020). Insurance Information from IBC for Those Affected by the Northern Alberta Floods. http://www.ibc.ca/ab/resources/media-centre/media-releases/insurance-information-from-ibc-for-those-affected-by-the-northern-alberta-floods. Accessed on 7 September 2020.

James, R. J. (1989). A history of radar. *IEE Review*, 35(9):343–349.

Jasek, M. (2003). Ice jam release surges, ice runs, and breaking fronts: field measurements, physical descriptions, and research needs. *Canadian Journal of Civil Engineering*, 30(1):113–127.

Jasek, M., Gauthier, Y., Poulin, J., and Bernier, M. (2013). Monitoring of freeze-up on the Peace River at the Vermilion Rapids using RADARSAT-2 SAR data. In *Proceedings of the 17th Workshop on River Ice, Edmonton, Alberta*, pages 21–24.

Jeffries, M. O., Morris, K., and Duguay, C. R. (2012). Floating ice: Lake ice and river ice. *Satellite Image Atlas of Glaciers of the World-State of the Earth's Cryosphere at the Beginning of the 21st Century: Glaciers, Global Snow Cover, Floating Ice, and Permafrost and Periglacial Environments*.

Kääb, A., Altena, B., and Mascaro, J. (2019). River-ice and water velocities using the Planet optical cubesat constellation. *Hydrology and Earth System Sciences*, 23(10):4233–4247.

Kuhn, M. and Johnson, K. (2019). *Feature engineering and selection: A practical approach for predictive models*. CRC Press.

Lee, J.-S., Grunes, M. R., Ainsworth, T. L., Du, L.-J., Schuler, D. L., and Cloude, S. R. (1999). Unsupervised classification using polarimetric decomposition and the complex Wishart classifier. *IEEE Transactions on Geoscience and Remote Sensing*, 37(5):2249–2258.

Lee, J.-S., Jurkevich, L., Dewaele, P., Wambacq, P., and Oosterlinck, A. (1994). Speckle filtering of Synthetic Aperture Radar images: A review. *Remote Sensing Reviews*, 8(4):313–340.

Lee, J.-S. and Pottier, E. (2009). *Polarimetric radar imaging: from basics to applications*. CRC press.

Liaw, A., Wiener, M., et al. (2002). Classification and regression by Random Forest. *R News*, 2(3):18–22.

Lindenschmidt, K.-E., Carstensen, D., Fröhlich, W., Hentschel, B., Iwicki, S., Kögel, M., Kubicki, M., Kundzewicz, Z. W., Lauschke, C., Łazarów, A., et al. (2019). Development of an ice jam flood forecasting system for the Lower Oder River – Requirements for real-time predictions of water, ice and sediment transport. *Water*, 11(1):95.

Lindenschmidt, K.-E. and Li, Z. (2018). Monitoring river ice cover development using the Freeman–Durden decomposition of quad-pol Radarsat-2 images. *Journal of Applied Remote Sensing*, 12(2):026014.

Lindenschmidt, K.-E. and Li, Z. (2019). Radar scatter decomposition to differentiate between running ice accumulations and intact ice covers along rivers. *Remote Sensing*, 11(3):307.

Lindenschmidt, K.-E., van der Sanden, J., Demski, A., Drouin, H., and Geldsetzer, T. (2011). Characterising river ice along the Lower Red River using RADARSAT-2 imagery. In *Proceedings of the 16th Workshop on River Ice, Winnipeg, MB*, pages 18–22.

Łoś, H., Osińska-Skotak, K., Pluto-Kossakowska, J., Bernier, M., Gauthier, Y., and Pawłowski, B. (2019). Performance evaluation of quad-pol data compare to dual-pol SAR data for river ice classification. *European Journal of Remote Sensing*, 52(sup1):79–95.

Łoś, H. and Pawłowski, B. (2017). The use of Sentinel-1 imagery in the analysis of river ice phenomena on the Lower Vistula in the 2015–2016 winter season. In *2017 Signal Processing Symposium (SPSympo)*, pages 1–5. IEEE.

Lotsari, E., Lind, L., and Kämäri, M. (2019). Impacts of hydro-climatically varying years on ice growth and decay in a Subarctic river. *Water*, 11(10):2058.

Mermoz, S., Allain, S., Bernier, M., Pottier, E., and Gherboudj, I. (2009). Classification of river ice using polarimetric SAR data. *Canadian Journal of Remote Sensing*, 35(5):460–473.

Mermoz, S., Allain-Bailhache, S., Bernier, M., Pottier, E., van Der Sanden, J. J., and Chokmani, K. (2013). Retrieval of river ice thickness from C-band PolSAR data. *IEEE Transactions on Geoscience and Remote Sensing*, 52(6):3052–3062.

Moreira, A., Prats-Iraola, P., Younis, M., Krieger, G., Hajnsek, I., and Papathanassiou, K. P. (2013). A tutorial on Synthetic Aperture Radar. *IEEE Geoscience and remote sensing magazine*, 1(1):6–43.

Morse, B. and Hicks, F. (2005). Advances in river ice hydrology 1999–2003. *Hydrological Processes: An International Journal*, 19(1):247–263.

Nave, C. (2011). Classification of Polarization. http://230nsc1.phyastr.gsu.edu/hbase/phyopt/polclas.html. Accessed on 13 January 2020.

Pavelsky, T. M. and Smith, L. C. (2004). Spatial and temporal patterns in Arctic river ice breakup observed with MODIS and AVHRR time series. *Remote Sensing of Environment*, 93(3):328–338.

Plank, S., Jüssi, M., Martinis, S., and Twele, A. (2017). Mapping of flooded vegetation by means of polarimetric Sentinel-1 and ALOS-2/PALSAR-2 imagery. *International Journal of Remote Sensing*, 38(13):3831–3850.

Potin, P. (2013). Sentinel-1 User Handbook.

Prowse, T., Alfredsen, K., Beltaos, S., Bonsal, B., Duguay, C., Korhola, A., McNamara, J., Vincent, W. F., Vuglinsky, V., and Weyhenmeyer, G. A. (2011). Arctic freshwater ice and its climatic role. *Ambio*, 40(1):46–52.

Puestow, T. M., Randell, C., Rollings, K. W., Khan, A. A., and Picco, R. (2004). Near real-time monitoring of river ice in support of flood forecasting in eastern Canada: towards the integration of Earth observation technology in flood hazard mitigation. *IGARSS 2004. 2004 IEEE International Geoscience and Remote Sensing Symposium*, 4:2268–2271.

Qi, Z., Yeh, A. G.-O., Li, X., and Lin, Z. (2012). A novel algorithm for land use and land cover classification using RADARSAT-2 polarimetric SAR data. *Remote Sensing of Environment*, 118:21–39.

Quegan, S. (1994). A unified algorithm for phase and cross-talk calibration of polarimetric data-theory and observations. *IEEE Transactions on Geoscience and Remote Sensing*, 32(1):89–99.

Raney, R. K. (1998). Radar fundamentals: Technical perspective. *Principals and Applications of Imaging Radar, Manual of Remote Sensing*, 2:9–130.

Raney, R. K. (2007). Hybrid-polarity SAR architecture. *IEEE Transactions on Geoscience and Remote Sensing*, 45(11):3397–3404.

Raschka, S. and Mirjalili, V. (2017). *Python machine learning*. Packt Publishing Ltd.

Rosenqvist, A. and Killough, B. (2018). A Layman's interpretation guide to L-band and C-band Synthetic Aperture Radar data, v2.0.

Shen, H. T. (2010). Mathematical modeling of river ice processes. *Cold Regions Science and Technology*, 62(1):3–13.

Shen, X., Zhang, J., Zhang, X., Meng, J., and Ke, C. (2017). Sea ice classification using Cryosat-2 altimeter data by optimal classifier–feature assembly. *IEEE Geoscience and Remote Sensing Letters*, 14(11):1948–1952.

Singh, G., Mohanty, S., Yamazaki, Y., and Yamaguchi, Y. (2019). Physical scattering interpretation of POLSAR coherency matrix by using compound scattering phenomenon. *IEEE Transactions on Geoscience and Remote Sensing*.

Skolnik, M. I. et al. (1980). *Introduction to radar systems*, volume 3. McGraw-hill New York.

Small, D. (2011). Flattening gamma: Radiometric terrain correction for SAR imagery. *IEEE Transactions on Geoscience and Remote Sensing*, 49(8):3081–3093.

Sobiech, J. and Dierking, W. (2013). Observing lake-and river-ice decay with SAR: advantages and limitations of the unsupervised k-means classification approach. *Annals of Glaciology*, 54(62):65–72.

Soh, L.-K. and Tsatsoulis, C. (1999). Texture analysis of SAR sea ice imagery using gray level co-occurrence matrices. *IEEE Transactions on Geoscience and Remote Sensing*, 37(2):780–795.

Sun, W., Trevor, B., and Kovachis, N. (2015). Athabasca River Ice Observations 2014-2015 (Annual Report). *Alberta Environment and Parks, Alberta*.

Thompson, A. A. (2015). Overview of the RADARSAT Constellation Mission. *Canadian Journal of Remote Sensing*, 41(5):401–407.

Torres, R., Snoeij, P., Geudtner, D., Bibby, D., Davidson, M., Attema, E., Potin, P., Rommen, B., Floury, N., Brown, M., et al. (2012). GMES Sentinel-1 mission. *Remote Sensing of Environment*, 120:9–24.

Tracy, B. T. and Daly, S. F. (2003). River ice delineation with RADARSAT SAR. In *Proceedings of the 12th Workshop on River Ice, Edmonton, Alberta*.

Ulaby, F. T., Moore, R. K., and Fung, A. K. (1986). Microwave remote sensing: Active and passive. Volume 3 – From theory to applications.

Unterschultz, K., van der Sanden, J., and Hicks, F. (2009). Potential of RADARSAT-1 for the monitoring of river ice: Results of a case study on the Athabasca River at Fort McMurray, Canada. *Cold Regions Science and Technology*, 55(2):238–248.

van der Sanden, J. (1997). *Radar remote sensing to support tropical forest management*.

van der Sanden, J. (2015). River ice mapping and monitoring using SAR satellites. https://www.nrcan.gc.ca/earth-sciences/permafrost-ice-snow/lake-river-ice/9166. Accessed on 26 January 2020.

van der Sanden, J., Drouin, H., and Geldsetzer, T. (2020). An automated procedure to map breaking river ice with C-band HH SAR data. *Remote Sensing of Environment*.

van der Sanden, J., Drouin, H., Hicks, F., and Beltaos, S. (2009). Potential of RADARSAT-2 for the monitoring of river freeze-up processes. In *Proceedings of the 15th Workshop on River Ice, St. John's, NL, Canada*, pages 14–17.

van der Sanden, J. and Geldsetzer, T. (2015). Compact polarimetry in support of lake ice breakup monitoring: Anticipating the RADARSAT Constellation Mission. *Canadian Journal of Remote Sensing*, 41(5):440–457.

van der Sanden, J., Geldsetzer, T., Drouin, H., and Deschamps, A. (2014). On the anticipated utility of RCM CP data for freshwater ice mapping and monitoring. In *2014 IEEE Geoscience and Remote Sensing Symposium*, pages 1564–1567. IEEE.

van Zyl, J. (2011). *Synthetic Aperture Radar Polarimetry*, volume 2. John Wiley & Sons.

Vincent, F., Raucoules, D., Degroeve, T., Edwards, G., and Abolfazl Mostafavi, M. (2004). Detection of river/sea ice deformation using satellite interferometry: Limits and potential. *International Journal of Remote Sensing*, 25(18):3555–3571.

Weber, F., Nixon, D., and Hurley, J. (2003). Semi-automated classification of river ice types on the Peace River using RADARSAT-1 Synthetic Aperture Radar (SAR) imagery. *Canadian Journal of Civil Engineering*, 30(1):11–27.

Woodhouse, I. H. (2017). *Introduction to Microwave Remote Sensing*. CRC press.

Xie, Q., Meng, Q., Zhang, L., Wang, C., Wang, Q., and Zhao, S. (2018). Combining of the H/A/Alpha and Freeman–Durden Polarization Decomposition Methods for Soil Moisture Retrieval from Full-Polarization Radarsat-2 Data. *Advances in Meteorology*, 2018.

Yang, H. L., Yuan, J., Lunga, D., Laverdiere, M., Rose, A., and Bhaduri, B. (2018). Building extraction at scale using convolutional neural network: Mapping of the United States. *IEEE Journal of Selected Topics in Applied Earth Observations and Remote Sensing*, 11(8):2600–2614.

Yang, X., Pavelsky, T. M., and Allen, G. H. (2020). The past and future of global river ice. *Nature*, 577(7788):69–73.

Younis, M., Huber, S., Patyuchenko, A., Bordoni, F., and Krieger, G. (2009). Performance comparison of reflector-and planar-antenna based digital beam-forming SAR. *International Journal of Antennas and Propagation*, 2009.

Zhang, G., Perrie, W., Zhang, B., Khurshid, S., and Warner, K. (2018). Semi-empirical ocean surface model for compact-polarimetry mode SAR of RADARSAT Constellation Mission. *Remote Sensing of Environment*, 217:52–60.